Development of CaS:Eu^{2+}/Dy^{3+} Persistent and NIR Photo-Stimulated Nanophosphors

Diana Consuelo Rodríguez Burbano

A Thesis
in
The Department
of
Chemistry and Biochemistry

Presented in Partial Fulfillment of the Requirements
for the Degree of Doctorate of Philosophy at
Concordia University
Montreal, Quebec, Canada

February 2017

CONCORDIA UNIVERSITY

SCHOOL OF GRADUATE STUDIES

This is to certify that thesis prepared

By: Diana Consuelo Rodríguez Burbano

Entitled: Development of CaS:Eu^{2+}/Dy^{3+} Persistent and NIR Photo-Stimulated Nanophosphors

and submitted in partial fulfillment of the requirements for the degree of

Doctorate of Philosophy (Chemistry)

complies with the regulations of the University and meets the accepted standards with respect to originality and quality.

Signed by the final examining committee:

Dr. Jean-Roch Laurence Chair

Dr. Jose García Solé External Examiner

Dr. Shimon Amir External to Program

Dr. Christine DeWolf Examiner

Dr. Yves Gélinas Examiner

Dr. John A. Capobianco Thesis Supervisor

Approved by

Chair of Department or Graduate Program Director

Dean of Faculty

ABSTRACT

Development of $CaS:Eu^{2+}/Dy^{3+}$ Persistent and NIR Photo-Stimulated Nanophosphors

Diana Consuelo Rodríguez Burbano, Ph.D.
Concordia University, 2017

Persistent luminescent nanophosphors are nano-sized materials that have recently come into the limelight and have attracted attention as potential fluorescent imaging probes due to their attractive optical properties. The synthesis and characterization of red persistent luminescent $CaS:Eu^{2+}/Dy^{3+}$ nanophosphors were investigated. These nanophosphors are capable of energy storage due to presence of electron trap sites. This provides a new approach of avoiding exposure of biological tissue to high-energy irradiation and eliminating the generation autofluorescence since these nanophosphors are charged *ex vivo* with UV irradiation. Once injected in the body, *in vivo* images can be acquired by detection of the red persistent luminescence originating from the shallow traps present in the nanophosphor. After the persistent luminescence has subsided, energy stored in deeper traps can be released upon near infrared light (NIR) irradiation, resulting in a red photo-stimulated emission.

With the goal to develop $CaS:Eu^{2+}/Dy^{3+}$ persistent and NIR photo-stimulated nanophosphors, synthesis and characterization of the optical properties of CaS nanoparticles and $CaS:Eu^{2+}$ and $CaS:Eu^{2+}/Dy^{3+}$ nanophosphors were carried out. The nature of the electron trap sites and the trapping and de-trapping mechanisms were studied by wavelength resolved thermally stimulated luminescence. In addition, the generation of strong red light emission following NIR excitation of the $CaS:Eu^{2+}/Dy^{3+}$ nanophosphors is demonstrated. This basic understanding is primordial in the development of a new nano-sized photonic materials in the field of biomedical luminescent probes for applications in bioimaging.

The integration of the CaS:Eu^{2+}/Dy^{3+} nanophosphors as an optical bioimaging probe is limited by the hygroscopic character of the CaS nano host. Consequently, different surface modification strategies were studied to render the CaS:Eu^{2+}/Dy^{3+} nanophosphors water dispersible and at the same time prevent hydrolization. Among the surface modification strategies studied, the grafting of a silica shell, tetraethyl orthosilicate (TEOS), was chosen to carry out preliminary *in vivo* fluorescence optical imaging experiments using TEOS-CaS:Eu^{2+}/Dy^{3+} nanophosphors as the luminescent probes.

AGRADECIMIENTOS ~ ACKNOWLEDGEMENTS

Behind this work, there are many people that with their schooling, support, advices, guidance, encouragement, friendship and love made possible for me to never give up and to whom I wish to acknowledge. The words I want to express are coming from my heart and it only knows one language…

Empiezo con un enorme GRACIAS para mi supervisor, el Profesor John A. Capobianco. Á él, le agradezco que me haya dado la oportunidad de unirme a su grupo de investigación. Gracias por creer en mis capacidades y en que podría llevar a cabo la realización de este proyecto. Gracias por creer que no soy un "vegetal común y corriente del jardín". Agradezco todas sus enseñanzas y sus consejos, no sólo a nivel profesional, sino también en lo personal. Gracias por retarme a ser mejor, por darme la libertad para establecer mis propios objetivos, planear, experimentar, aprender, fallar, pero aún más importante, por siempre alentarme a no rendirme y buscar la excelencia en mi trabajo. Llevaré siempre conmigo todas nuestras charlas de tipo científico que incentivaron mi curiosidad por aprender más. Así también me llevo grabados en el alma muchos buenos momentos y todas nuestras conversaciones sobre historia, política, futbol, tenis, viñedos, café y demás. Muchas Gracias Boss.

Quiero agradecer a los miembros de mi comité de estudios doctorales: Dra. Christine DeWolf, agradezco todo el apoyo y guía que me dió para poder llevar a cabo la realización de este proyecto. Gracias por estar siempre disponible para orientarme en la búsqueda de soluciones. Por siempre estaré agradecida por todos los comentarios y sugerencias recibidos de su parte que le puedo asegurar han aportado inmensamente en mi formación. Dr. Yves Gélinas, gracias por acompañarme durante todo mi proceso como estudiante de posgrado. Agradezco de corazón todas las palabras de aliento, las sugerencias, los comentarios positivos, los puntos a reforzar y por siempre transmitirme confianza. Así mismo, quiero agradecer el apoyo recibido por parte del Dr. Peter Bird, quien perteneció a

mi comité cuando estaba realizando mis estudios de maestría, y quien apoyó mi transferencia al programa de doctorado.

Quiero extender mi agradecimiento a todos los colaboradores que contribuyeron en la realización de este proyecto y de quienes he tenido la oportunidad de aprender. Gracias al Dr. Peter Dorenbos (Delf University, Países Bajos) por sus valiosas contribuciones en todas las publicaciones generadas a través de la realización de este proyecto. Así también quiero agradecer al Dr. Marco Betinelli (University of Verona, Italia) por sus excelentes contribuciones a la realización de este proyecto. Infinitas gracias al Dr. Suchinder K. Sharma, al Dr. Bruno Viana y al Dr. Cyrille Richard (Chimie-ParisTech, France) por su colaboración con los experimentos de termoluminiscencia, así como los experimentos *en vivo*. La existencia de esta colaboración ha sido fundamental en el éxito de este proyecto.

Quiero expresar mi inmensa gratitud al Dr. Louis Cuccia por ser una mano que siempre está extendida para mí. Gracias por todas las veces en que fue voz de aliento y de lograr subir mi ánimo para ver las situaciones con optimismo. Gracias por enseñarme muchas cosas curiosas y especiales que relacionan la ciencia y la vida diaria. También quiero agradecer al Dr. Rafik Naccache, quien es ejemplo de dedicación, responsabilidad y excelencia. Muchas gracias por todo el conocimiento compartido, los buenos consejos y orientarme en cómo hacer de manera adecuada una presentación oral.

Agradezco a todos los miembros de la familia que conforma el Departamento de Química y Bioquímica de la Universidad de Concordia. Gracias por recibirme con una sonrisa y su disponibilidad al ayudarme a resolver las “situations”. Muchas gracias de todo corazón a Miriam Posner, Maria Dochia, Vincent Lau, Mihai Ciortea, Zornitsa Stoyanova, Kai Lee, Lisa Montesano, Maria Ciaramella, Donna Craven y Hilary Scuffell. Me llevo guardados en el corazón maravillosos recuerdos con cada uno de ustedes. Quiero agradecer al Dr. Rolf Schimidt por toda su colaboración en el desarrollo de software y su invaluable ayuda en los conflictos de tipo técnico. Muchas gracias, infinitas gracias a Dan, Bob, Richard y Aldo, son unos ¡magos de la ingeniería!

Durante mi tiempo como miembro del grupo de investigación del Dr. Capobianco, tuve la oportunidad de conocer muchas personas que no sólo aportaron en mi crecimiento profesional sino también con su apoyo y aliento. Agradezco infinitamente que en este grupo de investigación logré consolidar muy bonitas y valiosas amistades. Muchas gracias a todos los miembros del grupo de investigación de lantánidos (pasados y presentes). Ha sido un placer y les deseo lo mejor en su vida personal y profesional.

Quiero agradecer a mi familia (Rodríguez-Melo, Burbano-Montenegro, Chávez-Montenegro, Echeverría-Burbano), no ha sido nada fácil tenerlos lejos, pero nunca deje de sentir su apoyo, amor y buena energía. Estoy muy agradecida de hacer parte de esta hermosa y muy única familia.

Un maestro Jedi es a un aprendiz Padawan como mi amiga Emma es a mí. Emma, punteas en mi lista de estrellitas. Admiro tu especial capacidad de incentivar a la gente a hacer todo lo más bonito que se pueda. Nuestra amistad nació de una perfecta sincronía y sólo mejora con en el tiempo a pesar del tiempo-distancia. Estaré por siempre en deuda contigo por todo lo que me compartiste y me enseñaste. ¡Muchas Gracias Emma!

Mi Zrororof, he llegado el final y pronto los gallitos estarán juntos de nuevo en la perfecta combinación de rojo y blanco. Muchas Gracias mi Zrororof por ser mi roca en los momentos en que cruzaba por cuerdas flojas, gracias por ser voz de aliento, ser ruta de escape, por tener siempre las palabras precisas, por ser modelo de vida, por estar en mi vida, por ser cómplice, y por dejarme ver el mundo a través de tus ojos. “-Creo que sí, estás demente. Pero te diré un secreto: las mejores personas lo están”.

Muchas Gracias Sr. Afacevedo. Agradezco todos los días a la vida por darnos la oportunidad de encontrarnos en Montreal y convertirnos en el equipo que somos hoy en día. Tu apoyo, tu positivismo, tu ayuda y tu comprensión han sido sumamente importantes para mí. Y sólo deseo poder tener el mismo papel en tu vida. Muchas gracias por estar siempre junto a mí respaldándome, tanto en los buenos como en los malos momentos. ¡Muchas Gracias mi Pato!.

Gracias a Lula y Gaudí, por ser mis fieles y pacientes compañeritos, su existencia hace que mi mundo sea mejor.

A los amores de mi vida, mis padres, Consuelo y Miguel. Mis osos, son ustedes mi preciado más grande, importante y valioso. Soy la persona más afortunada del mundo de ser su hija y sólo quiero que se sientan orgullosos de mí. No hay palabras que describan a la perfección lo agradecida que me siento por su amor incondicional, su confianza, su fuerza, su tiempo, sus esfuerzos, sus enseñanzas, sus sacrificios y sus consejos. Gracias porque con todo esto forjaron quien soy yo. Este logro que hoy consigo es para ustedes. Mi Oso Bonito, mi héroe, gracias enseñarme el valor del trabajo duro, por enseñarme a ser fuerte e independiente, por consentirme, por tener respuestas a todas mis preguntas, y por hacerme saber que puedo llegar tan lejos como quiera. Mi Oso Loco, eres pilar fundamental de mi vida, gracias por enseñarme a vivir y a afrontar la vida. Soy la más afortunada por tenerte conmigo desde el principio y con orgullo llevo muchas cosas tuyas. Gracias mamita por consentirme, aconsejarme, guiarme, apoyarme, enseñarme y corregirme las veces que es necesario.

Los amo con toda mi alma mis ositos.

A Consuelo y Miguel

"Nothing in life is to be feared,
it is only to be understood.
Now is the time to understand more,
so that we may fear less."

Marie Curie

Table of Contents

List of Figures

List of Tables

List of Abbreviations

BOTW	Biological optical transparency window
CB (CBM)	Conduction band
CT	Computed tomography
EDS	Energy-dispersive X-ray spectroscopy
ICG	Indocyanine Green
ICP-MS	Inductively Coupled Plasma – Mass Spectroscopy
MRI	Magnetic resonance imaging
NIR	Near infrared light
PAA	Polyacrilic acid
PEG	Polyethylene glycol
PET	Positron emission tomography
PL	Persistent luminescence
PVP	Polyvinylpyrrolidone
QDs	Quantum dots
TEM	Transmission electron microscopy
TEOS	Tetraethyl orthosilicate
VB (VBM)	Valence band
XRPD	X-ray powder diffraction
ZGO	Zinc gallate

Chapter 1 – Introduction

1.1 Bioimaging

Before the 19th century, doctors relied on handmade drawings, written and oral descriptions of symptoms and pathologies to establish a diagnosis. In this period, there were no imaging tools available that allowed for the non-invasive viewing of the internal structure and organs. Hence, dissection was the preponderant technique used to gather physiological and pathological information.[1] In 1895, Wilhelm Röntgen, a German physicist and engineer, discovered how to generate and detect X-ray radiation. He realised that X-rays can penetrate through solid objects and detected on a photographic film. With this finding, he was the first to make medical use of X-rays when he took a picture of the now famous hand of his wife on a photographic plate. The discovery of Rontgen has led to the development of computed tomography, mammography, angiography and fluoroscopy making it the most used medical bioimaging technique.[2]

From this moment in history, bioimaging has become a research area that bridges the gap between the physical sciences, engineering and the life sciences. It has become the cornerstone in the modernization of medicine by providing the ability to acquire, process and visualize structural or functional images of living species or systems of biological interest.[3] Different bioimaging techniques have been developed as consequence of the need to provide factual diagnoses, to establish treatment and to have more precise evaluation of its efficiency.

1.1.1 Fluorescence Optical Imaging

Fluorescence optical imaging is non-invasive bioimaging technique based on the excitation of fluorescent molecules (fluorophores) using light of an appropriate wavelength, followed by the emission of lower-energy light for imaging.[4] In recent years, this definition has been extended to include photoluminescent nanoparticles that have been used as optical imaging probes.[5] Fluorescence imaging has been used to visualize and

study processes of biochemical and biological interest on various levels ranging from subcellular to small animal (whole body) imaging.[5a, 6]

Whereas some of the clinical imaging techniques require ionizing radiation to generate images, fluorescent optical imaging relies on irradiation that range from ultraviolet to infrared light. Therefore, potentially negative side effects associated to ionizing radiation are eliminated. In addition, the lower risk of the irradiation used translates in the possibility to carry out direct observation and faster analysis process throughout surgical procedures and long-term and repetitive monitoring of diseases progression and evaluation of treatment efficiency.[7] Additionally, the substantial effort in the design and engineering of fluorescent optical imaging systems with high sensitivity has resulted in the relative ease of operation and significantly less expensive fluorescent imaging setups in comparison to other bioimaging techniques.

Fluorescence optical imaging can be performed by exploiting the optical properties of endogenous fluorophores present in some living subjects such as reduced nicotinamide adenine dinucleotide, flavins, porphyrins, collagen, elastin and lipo-pigments to name a few.[8] The presence of these endogenous fluorophores has facilitated considerably the imaging at the cellular and subcellular level. However, as the system increases in complexity to the acquisition of *in vivo* whole-body images, the technique becomes very limited due to the presence of endogenous fluorophores that absorb light and the scattering of the excitation light, for example by tissue .[9] The absorption coefficients as a function of the excitation wavelength of some of the most important endogenous fluorophores are shown in Figure 1.1. High absorption coefficients are exhibited by species in the blood (*e.g.* oxyhemoglobin and deoxyhemoglobin Hb) and the skin (melanin) in the UV-Vis region. Consequently, the transmission of the excitation light is reduced thus limiting the penetration depth. In addition, UV-Vis light is highly scattered which further reduces penetration depth. Furthermore, the endogenous fluorophores will absorb the UV-Vis light that results in autofluorescence. This fluorescence occurs in the UV-vis region, and overlaps with the signal from the fluorophore thus, limiting further the sensitivity of the technique.[7a]

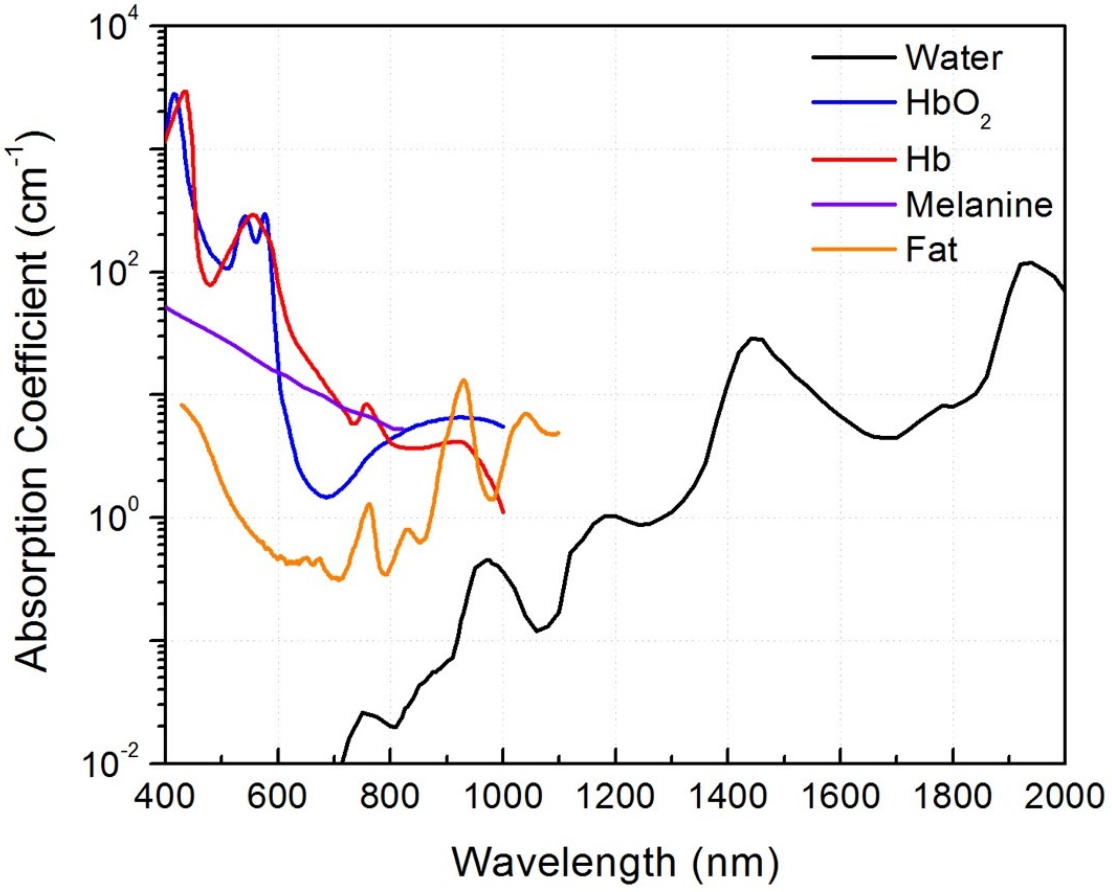

Figure 1.1 Absorption properties of water and important chromophores found in blood (oxyhemoglobin HbO_2, and deoxyhemoglobin Hb), epidermis and tissues.[10]

The currently used whole-body fluorescence optical imaging systems, have allowed the acquisition of images from small animal models, mostly mice, which minimize the light path that the irradiation light needs to penetrate. Moreover, nude and albino mice (*e.g.* BALB/c mouse) are preferred to decrease the attenuation of the excitation light occurring due to absorption, scattering and autofluorescence. To reduce these impediments several exogenous fluorescent probes have been proposed that absorb light in the region 650 and 1350 nm where water and tissue endogenous fluorophores exhibit low absorption coefficients (Figure 1.1). This spectral region is known as the biological optical transparency window (BOTW).[11] BOTW has been divided in two regions: *i)* the first biological window (NIR-I) between 650 nm and 950 nm and *ii)* the second biological window (NIR-II) between 1000 nm and 1350 nm. In the first region, water is nearly transparent and absorption is minimized. In the second region, water absorption

coefficients are higher in comparison to the NIR-I, but still deeper light penetration can be achieved since the light scattering coefficient of different tissues such as skin, brain, breast and bone, decreases as a function of increasing wavelength.[9, 11-12] In the recent years, a third biological window (NIR-III) has been proposed in the range between 1550 to 1870 nm. In this range, higher optical contrast is obtained due to the nearly zero tissue autofluorescence and the significant higher tissue penetration as the scattering of light for all intents and purposes is eliminated.[13]

Accordingly, great efforts have been focussed on the design and synthesis of exogenous fluorescent probes that provide higher contrast and resolution based on the following criteria:[14]

- *Biocompatibility*. The chemical nature and physicochemical properties of the exogenous fluorescent probe need to provide dispersibility and colloidal stability in buffers, cell culture media and bodily fluids. The introduction of the exogenous probe should not cause any damage in the structure, composition and physiological functions of the entity to be imaged.

- *Targeting.* The exogenous fluorescent probe should exhibit highly preferential interaction with the specific region of interest to be imaged in comparison with the surrounding environment.

- *Facile excitation and detection.* The exogenous fluorescent probe should possess a significantly higher absorption coefficient at a given excitation wavelength than the one exhibited by the surrounding environment. Thus, the luminescence of the probe should use a wavelength of excitation that does not induce autofluorescence. Furthermore, the excitation, detection and generation of optical images should be achieved from commercially available optical systems.

Organic dyes have been widely used as exogenous fluorescent probes. These probes are molecular systems with a defined chemical structure. The origin of the luminescence exhibited by these organic fluorophores may arise from an optical transition delocalized over the whole fluorophore (e.g. fluorescein and cyanine families) or from intramolecular charge transfer transitions (e.g. coumarin family). Typically, these dyes possess high molar absorption coefficients and exhibit moderate to high quantum yields. [15] Recently efforts have been oriented towards the synthesis of organic dyes that can be excited in the NIR-I or NIR-II range and that their emission are also in these optical windows. Antaris *et al.*, synthesized a PEGylated organic dye (CH1055-PEG) and demonstrated its use as a luminescent probe for *in vivo* NIR-II imaging (Figure 1.2A and B). The CH1055-PEG allows the acquisition of higher quality images than those obtained using indocyanine green, however it exhibits a lower quantum yield. The authors demonstrated the imaging of inguinal lymph node and lymphatic vasculature (Figure 1.2C).[16]

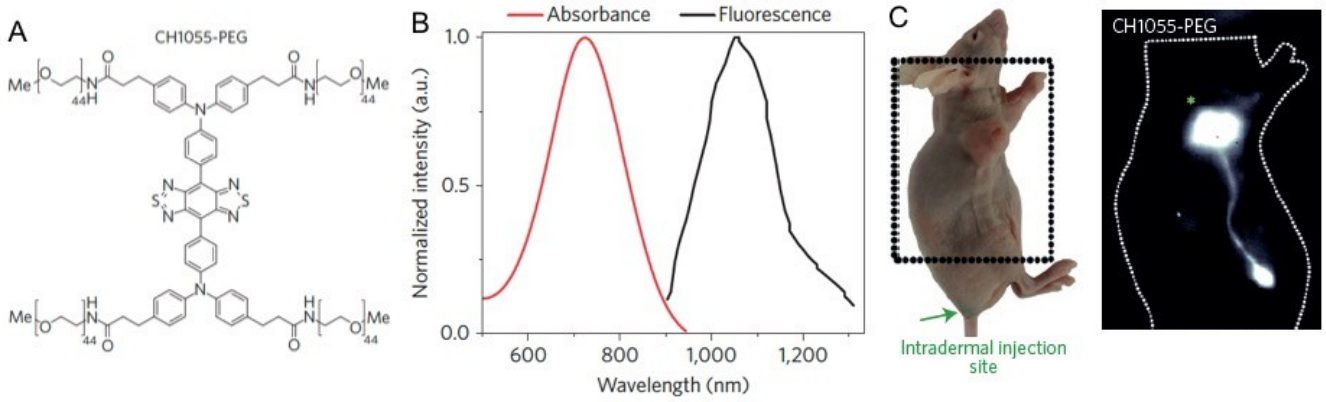

Figure 1.2 (A)Chemical structure of the NIR-II organic dye CH1055-PEG; (B) Absorption and emission spectra of CH1055-PEG and (C) (Left) A digital photograph of a nude mouse with a U87MG tumour located on the shoulder. The dotted rectangle shows the region imaged and the green arrow denotes the fluorophore injection site. (Right) NIR-II fluorescence image showing the inguinal lymph node and lymphatic vasculature. The green asterisk denotes the location of the tumor. Figure adapted from "A small-molecule dye for NIR-II Imaging" by Antaris *et al*. Nature Materials, 2016, ref [16].

Notwithstanding the widespread use of organic dyes, many shortcomings exist in their use for fluorescent optical imaging. A considerable limitation is related to their low photostability resulting in a reduced optical response.[5c, 17] Thus, a significant decrease of the signal-to-noise ratio, which translates in a reduced detection sensitivity. Furthermore,

organic fluorophores lack the necessary structural properties to build a scaffold system to impart multimodal functionalities that would allow targeting, diagnostics, and therapeutics to be carried out without affecting their optical properties. Additionally, it has been reported that some of the small organic dyes such as fluorescein isothiocyanate are phototoxic. Upon irradiation of these probes, reactive oxygen species may form, triggering undesired oxidation of the biological components in the system under study.[18]

1.2 Nano-sized Luminescent Probes

On December 29, 1959 Richard Feynman gave the now famous often quoted lecture entitled "There's Plenty of Room at the Bottom". Feynman's 7,000 words were a defining moment in nanoscience/nanotechnology long before anything "nano" appeared on the horizon. "What I want to talk about" he said "is the problem of manipulating and controlling things on a nanoscale..." In his lecture, he showed the potential of making machines extremely small, and drew a parallel to biology. "Many of the cells are very tiny, but they are active; they manufacture various substances, they walk around; they wiggle; and do all kind of marvelous things- all on a very small scale."[19] Feynman's lecture inspired many scientists to study physics at the nanoscale and laid the groundwork for nanoscience/nanotechnology to overcome some of the challenges in biomedicine for example, identifying the molecular origin of many disease through novel diagnostic tools and imaging technologies.

Nanoscience, studies the properties of materials that has at least one dimension in the nanometer scale, 1 to 100 nm (1 nm = 10^{-9} m). Properties of materials with nano-scale dimension show properties (e.g. optical, electrical, mechanical etc.) that are significantly different from those of bulk materials. Therefore, they can no longer be described by the principles of classical physics and only quantum mechanics principles apply.[20]

Nanoparticles have been exploited for a wide variety of applications in fields such as electronics, food industry, catalysis, fuels, aerospace and automobile engineering, and environmental sciences. Moreover, materials in the nanometer regime allow for unique interactions with biological system, as they are approximately the same size as enzymes,

DNA and other bio-macromolecules (Figure 1.3). Therefore, photoactive/photoresponsive nanoparticles such as luminescent quantum dots, carbon dots, lanthanide-doped inorganic materials have attracted attention because they have demonstrated exciting potential to furthering biomedical science (*e.g.* bioimaging, cell targeting and therapeutics).

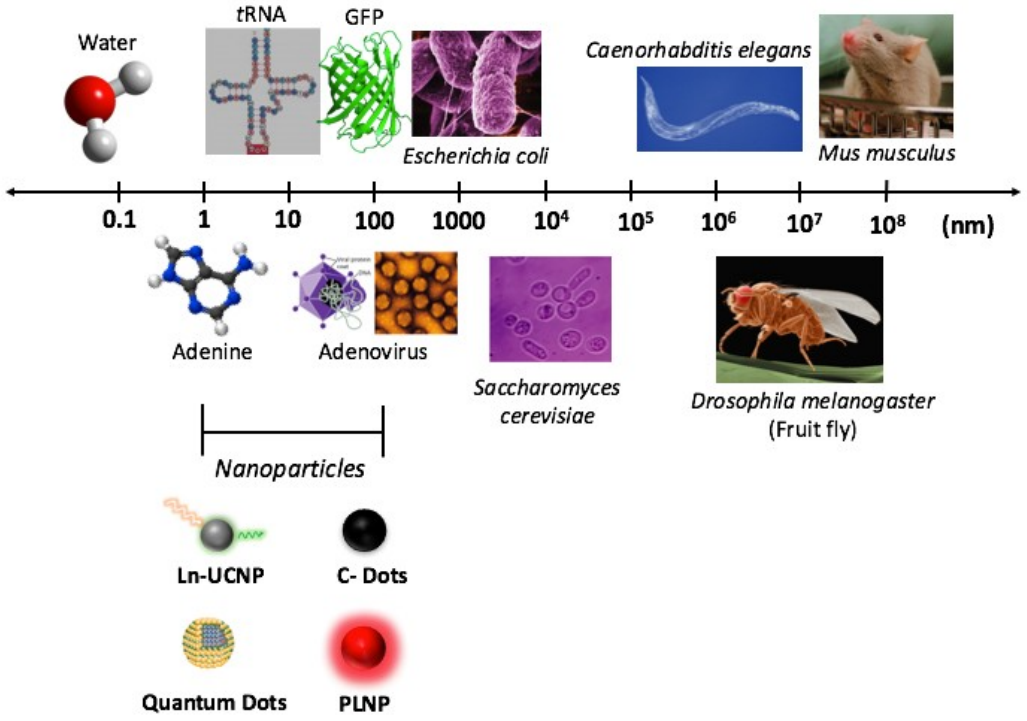

Figure 1.3 Size comparison scale of the animal models and other species of biological interest with respect to nanoparticles. (Ln-UCNP is the abbreviation used for lanthanide base nanoparticles, C-dots for carbon dots and PLNP for persistent luminescent nanoparticles). Images of *Escherichia coli, Caenorhabditis elegans, Mus musculus, Drosophila melanogaster, Saccharomyces cerevisiae* and Adenovirus were taken from Genetics (2014), Genetics (2005) W.H. Freeman, ref [21].

All nano-scale materials possess properties that distinguishes them from bulk materials.[5c, 22] Nanoparticles are an assembly of atoms. As the size is decreased, there is a major decrease in the volume that the constituent atoms of the nanoparticles can occupy thus, most of the atoms are found at the surface. Nanoparticles exhibit large surface areas with high surficial energy due to the presence of dangling bonds. The need to reduce this surface energy favors the addition of moieties that provide or improve dispersibility of the nanoparticles in aqueous environments. Recently, Wilhelm *et al.*, introduced an appropriate terminology 'Type ex' and 'Type add' to describe the procedures used to convert the surface

of nanoparticles from hydrophobic to hydrophilic a necessary requirement for biological applications of nanomaterials.[23] 'Type ex' involves the exchange of the hydrophobic ligand by a hydrophilic ligand containing groups such as –COOH, -NH_2 or –SH. Whereas, 'Type add' is the addition of an amphiphilic layer, a mesoporous or silica coating or an appropriate polymer while maintaining the original hydrophobic ligand.

Furthermore, depending on the nature of the modified surface, introduction of several functionalities such as targeting agents (*e.g.* folic acid, antibodies and peptides) and therapeutic agents (*e.g.* doxorubicin and porphyrin derivatives) may be achieved. *In vivo* experiments have revealed that nanoparticles without efficient coating or targeting ligands can suffer from nonspecific adsorption of proteins at the surface that leads to particle agglomeration and clearance *via* the reticular-endothelial system.[24] With a well-designed and optimized surface functionalization, selective and specific recognition of receptors located at the cell membrane can be achieved, as well as enhanced cellular internalization, non-cytotoxicity, and prevention of immune system capture.[25]

With the aim to develop superior, biocompatible and colloidally stable nano sized luminescent probes, research has explored different strategies for the synthesis and surface modification of different kind of photoluminescent nanoparticles (*e.g.* metallic nanoparticles, quantum dots, lanthanide based nanoparticles, silicon and carbon dots, nanodiamonds). In addition, several studies have been carried out to gain a fundamental understanding of their physicochemical properties and the nature of their interaction with biological studies, resulting in an exponential growth in the number of publications that demonstrate the potential use of photoluminescent nanoparticles as fluorescent optical imaging probes.[5c, 26]

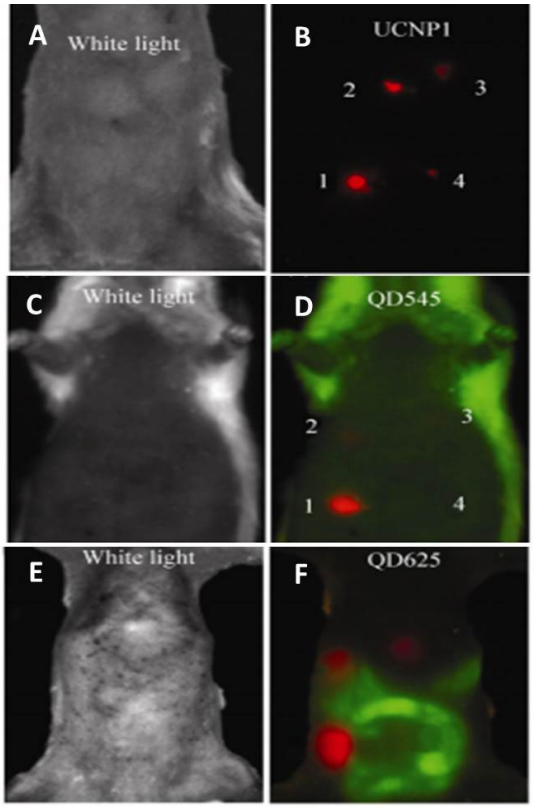

Figure 1.4 Comparison of imaging sensitivities between water dispersible upconverting nanoparticles and commercial quantum dots: (A) white light image of a mouse subcutaneously injected with various concentrations of upconverting nanoparticles; (B) *in vivo* image of the injected mouse; (C) and (E) white light images of mice subcutaneously injected with commercial quantum dots; (D) and (F) spectrally-resolved fluorescence images of QD545 injected mouse and QD625 injected mouse (red and green colors represent QD fluorescence and autofluorescence, respectively). Figure taken from "Highly-sensitive multiplexed *in vivo* imaging using pegylated upconversion nanoparticles" by Chen *et al*. Nano Research, 2010, ref [27].

The capacity to carry out tumor imaging and of early cancer diagnosis have been the driving forces to explore the use photoluminescent nanoparticles as fluorescence optical imaging probes. The enhanced permeability and retention effect exhibited by nanoparticles, the optical properties and the potential to introduce active targeting agents and their large surface area make them attractive for the detection of cancer at the early stages of the disease. An example of the research carried out on tumor imaging using fluorescence optical imaging was reported by Chen *et al*. The authors compared the *in vivo* imaging sensitivity of water dispersible upconverting nanoparticles (Oleate-Polyacrylic acid (PAA)-Polyethylene glycol (PEG) coated $NaYF_4:Er^{3+}/Yb^{3+}$) with commercially available water dispersible quantum dots for the identification of human carcinoma cell in mice.[27] The

authors reported *in vivo* detection sensitivity of the upconverting nanoparticles to be one order of magnitude higher than that exhibited by the commercial quantum dots. Despite the higher quantum yield of the semiconductor nanoparticles, the detection sensitivity is strongly reduced by the autofluorescence background (Figure 1.4).

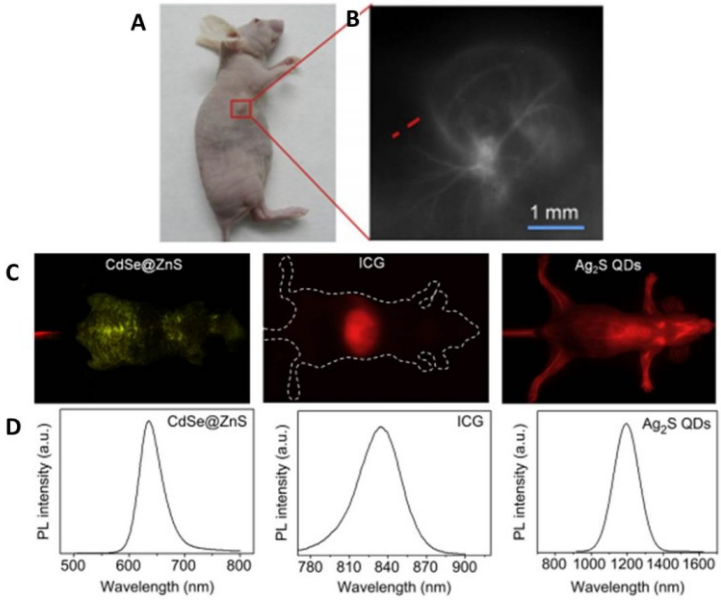

Figure 1.5 (A) Color photo of U87MG tumor-bearing mouse; (B) Amplified fluorescent image of the selected region in (A); (C) *In vivo* fluorescence images of CdSe@ZnS QDs, ICG, and Ag2S QDs in nude mice. CdSe@ZnS QDs, ICG and Ag_2S QDs were injected intravenously into mice and fluorescence images were taken after intravenous injection for 5 min under excitation at 455, 704, and 808 nm, respectively. The green-yellow signal of the mouse injected with CdSe@ZnS QDs indicates the strong autofluorescence of tissues in the visible emission window. The red signal concentrated in the liver of the mouse injected with ICG indicates the short blood circulation half-time. The red signal widely distributed in the whole body of mouse injected with Ag2S QDs indicates the long blood circulation half-time; and (D) The emission spectra of CdSe@ZnS QDs, ICG and Ag2S QDs using excitation at 455, 704, and 808 nm, respectively. Figure taken from "In vivo real-time visualization of tissue blood flow and angiogenesis using Ag_2S quantum dots in the NIR-II window" by Li *et al*. Biomaterials, 2014, ref [28].

New generation of quantum dots with optical properties in the BOTW have arisen as fluorescent luminescent probes. Promising results were reported by Li *et al* on the use of PEGylated Ag_2S as a fluorescent optical imaging probe for lymphatic drainage monitoring and tumor imaging.[28] The PEGylated Ag_2S quantum dots showed an emission peak at 1200 nm upon 808 nm irradiation reducing significantly the scattering caused by the tissues, showed negligible tissue autofluorescence, and increased tissue penetration. This allowed

for a more effective non-invasive identification of the circulatory systems that play a major role in diagnosis and therapy of the cancer in comparison to CdSe@ZnS QDs and indocyanine green (ICG) (Figure 1.5). However, concerns related to the toxicity of this nanoconstruct remain.

These selected examples are proof of the progress made to develop promising nano sized luminescent probes. However, challenges endure that expand further the research horizon in this field. In the case of metallic nanoparticles, morphologies have been developed with surface plasmon bands that can be excited in the NIR region. However, upon uptake by cells, agglomeration of the nanoparticles is observed. This causes changes in the their optical spectra, as it may shift and broaden due to plasmonic coupling.[29] Quantum dots excel due to the high quantum yield, high brightness and photostability, however their intrinsic toxicity due to their composition is still an important issue that must be resolved. On the other hand, lanthanide upconverting nanoparticles with their unique ability to convert NIR light into higher energy light (UV, Vis or NIR) have found widespread applications in bioassays, light-triggered based drug delivery, photodynamic therapy and bioimaging. However, a challenge which needs to be addressed is their low quantum yield.[5d] New promising emerging photoluminescent nanoparticles such as silicon and carbon dots and nanodiamonds, still require a full understanding of the origin of their fluorescence. Moreover, it is important to carry out systematic studies on biodistribution, toxicity, excretion pathways, time of clearance and interaction with biological entities for all photoluminescent nanoparticles.

1.3 Persistent Luminescent Nanoparticles

Persistent luminescence (PL) is an optical phenomenon defined as the emission of light that continues for a period of time after the external excitation is switched off. This optical property has been observed in semiconductors and insulators after irradiation with visible or UV light, electron beam, plasma beam, X-rays or γ-rays. The length of time of the persistent luminescence can be in the range of minutes up to hours. The physics behind this phenomenon exhibited by some materials arise from the recombination of electrons and holes. Upon high energy excitation electron-holes pairs are generated and trapped in

metastable states present in the host. These states, or trapping sites originate by the introduction of dopants ions (*e.g.* lanthanide and/or transition metal ions), impurities or intrinsic lattice defects. Trapping sites located near the conduction band are known as 'shallow traps' and at room temperature, electrons contained within may be liberated back to the conduction band. If the location of the traps is deeper in the band gap (> 0.5 eV), higher energy is required to attain the liberation of the trapped electrons. Hence, the release of these electrons may be achieved *via* thermal, electric or optical stimulation. After the release of electrons, the recombination of electrons and holes produces an emission in the visible or NIR region of the electromagnetic spectrum (Figure 1.6).[30] However, the nature of the trapping sites and the electron trapping-detrapping mechanism are still not well understood.[5c]

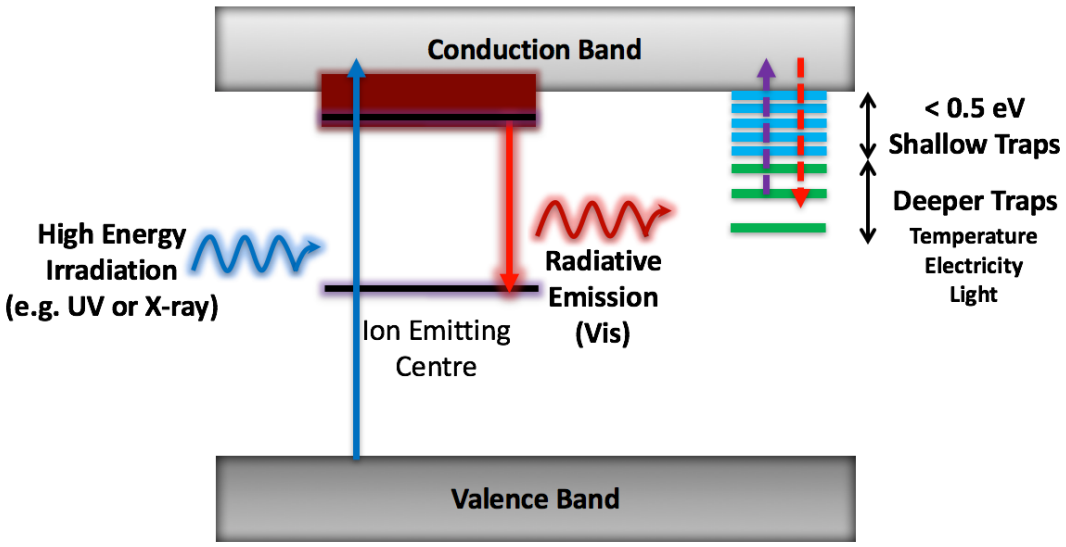

Figure 1.6 General mechanism of persistent luminescent materials.

Materials that exhibit persistent luminescence are currently used in different industries in the field of emergency and warning signs, luminous paints, textile printing and fibers and imaging plates for optical storage.[31] Recently, persistent luminescence nanomaterials have started to attract the attention of the scientific community for applications as fluorescent optical imaging luminescent probes.[5c, 32] Three important advantages emerge from the use of persistent luminescent nanomaterials as luminescent probes for *in vivo* optical imaging:

I. *Acquisition of images without the need of external excitation.* The 'charging' of persistent luminescent nanomaterials is carried out *via* high energy irradiation prior to introduction into the body. The electrons trapped in the shallow traps are released at room temperature conditions, producing a persistent luminescent emission. Thus, *in vivo* excitation is not required. This allows the prevention of tissue and DNA damage caused by irradiation with high-energy photon excitation or possible generation of heat due to the absorption of water in the NIR region.

II. *Eliminates autofluorescence.* In the absence of external irradiation and the low absorption properties exhibited by tissues in the BOTW, a significant improvement of the signal to noise ratio is expected in comparison to other luminescent probes that require excitations that may also activate the intrinsic fluorescence of tissue chromophores.

III. *Photo-stimulation.* As mentioned previously, electrons trapped in deeper traps may be released using higher energies provided by temperature, electricity or light. For optical imaging purposes, special interest is oriented to the release of the electrons using light, also referred as photo-stimulation. Thus, the energy stored in the deeper traps may be liberated upon NIR light, activating the luminescence process, hence extending if necessary the period of acquisition of images. This process can be carried out using available commercial NIR diodes.

Maldiney *et al*., reported the synthesis of $ZnGa_{1.995}Cr_{0.005}O_4$ (ZGO) persistent luminescent nanoparticles *via* low temperature sintering.[33] The nanoparticles exhibit a persistent luminescence centered at 695 nm that corresponds to the $^2E(^2G) \rightarrow {}^4A_2(^4F)$ transition of Cr^{3+} with a duration of 2 hours after 2 min of irradiation with 254 nm light. As well, the authors reported that the nanoparticles can be recharged using orange/red LED excitation obtaining a persistent luminescent time of 150 seconds. The surface of ZGO nanoparticles is modified to have hydroxyl moieties that further facilitates the grafting of a PEG silane shell to provide water dispersibility properties to the persistent luminescent nanoparticles. A hydrodynamic diameter of 80 nm was reported. Moreover, CT26 tumour bearing mice were injected intravenously with 200 μL solution of 2 mg/mL of the PEG-silane shell- ZGO nanoparticles and i*n vivo* fluorescence optical images were acquired 2

hours after the injection without the need of external excitation. Furthermore, *in vivo* images were obtained after exposing the animal to orange/red illumination 4 hours after injection. (Figure 1.7).

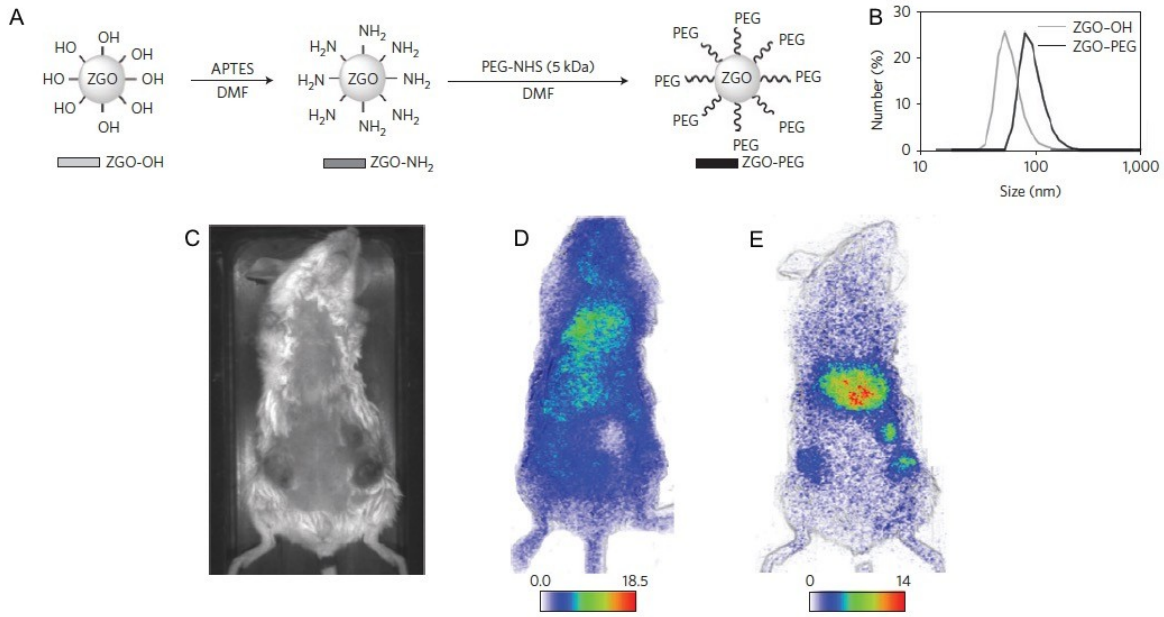

Figure 1.7 (A) Schematic representation of the surface modification carried out on the ZGO-OH persistent luminescence nanoparticles; (B) hydrodynamic diameter measured by dynamic light scattering in 5% glucose before and after PEG-silane surface modification; (C) CT26 tumour bearing mouse used for the in vivo experiments; (D) persistent luminescence image of a the CT26 tumour bearing mouse, 2 hours after the injection of PEG-silane shell- ZGO nanoparticles and (E) persistent luminescence image taken immediately after irradiation with orange/red light of a the CT26 tumour bearing mouse, 4 hours after the injection of PEG-silane shell- ZGO nanoparticles. Figure adapted from "The *in vivo* activation of persistent nanophosphors for optical imaging of vascularization, tumours and grafted cells" by Maldiney *et al*. Nature Materials, 2014, ref [33].

1.4 Statement of the Problem

The capacity to acquire *in vivo* images has played a key role towards gaining knowledge in the study of diseases, more efficient detection and diagnostic methods as well in the evaluation of the efficiency of therapeutic procedures. Great effort has been oriented to the improvement and development of different imaging techniques (MRI, CT, PET, X-Ray). However, the high cost of several of these techniques and some technological barriers prevents their widespread use. Fluorescence optical imaging makes use of photons and represents a rapidly expanding field, with direct applications in biology and medicine. Not

only has substantial effort been directed in the development of optical systems that allow the acquisition of *in vitro* and *in vivo* images with high resolution, but also in the elaboration of nano-sized luminescent probes that show optical properties in the BOTW.

Most luminescent probes that have been synthesized are metallic nanoparticles, quantum dots, and lanthanide based upconverting nanoparticles. Despite the large number of applications that have been based on these luminescent probes, several drawbacks remain. Consequently, new imaging probes are needed which eliminate the use of *in vivo* UV-Vis irradiation, provide higher signal to noise ratio, do not generate autofluorescence and their optical properties (excitation/emission) are in the BOTW. These probes should be capable to provide information on the physiological processes occurring in human organs, and with the proper functionalization facilitate diagnosis, drug delivery and therapeutic applications.

Among the novel luminescent nanoparticles, persistent luminescent nanoparticles show great potential as candidate since they possess the required characteristics. However, a significantly larger number of persistent luminescent materials show emission in the blue-green region of the electromagnetic spectrum in comparison to materials that exhibit persistent luminescent emissions in the BOTW. The challenge is to obtain an efficient red emitting persistent luminescent nanomaterials that exhibit a longer persistent luminescence time (> 2h). The best candidate to generate red persistent luminescence is the Eu^{2+} ion. In this oxidation state, the 5d levels are exposed and strongly affected by both the strength of the nephelauxetic and the crystal field effects provided by the host. When Eu^{2+} is introduced in sulfide based host, the electrostatic effect of the S^{2-} neighboring ions on Eu^{2+} causes a crystal field split of the 5d levels that lowers the lowest emitting level to energies that may produce red emissions.[34] The major challenge is to obtain red persistent luminescence from nano-sized, highly crystalline and colloidally stable nanoparticles that exhibit a persistent luminescence with a duration longer than two hours. In addition, the presence of electrons trapped in deeper traps can be used to acquire *in vivo* fluorescence optical images using NIR irradiation that provides deeper tissue penetration and less autofluorescence in comparison to visible irradiation.

In the work reported herein, the development of CaS:Eu^{2+}/Dy^{3+} nanophosphors is presented. These nanophosphors exhibit the required optical properties to establish them as promising candidates to be used not only in optical storage applications but as well as luminescent probes for fluorescent optical imaging. Most of the available persistent luminescent phosphors show emissions in the blue and green regions, and only a few show emissions in the yellow and orange regions. To date, obtaining a stable photo-stimulated phosphor in the red region has proven to be a difficult task. The combination of Eu^{2+} with Dy^{3+} in alkaline earth sulfide host appears as an attractive candidate to achieve this goal. Eu^{2+} is introduced in CaS to take advantage of the allowed transition $4f^6 5d^1 \rightarrow 4f^7$ at 650 nm, an intense red emission whereas Dy^{3+} is used as a co-dopant to induce the formation of electron trapping sites.

Furthermore, the persistent and photo-stimulated luminescence and the photo-stimulated mechanisms are complicated and not totally understood; however, this understanding is primordial in the development of a new nano-sized photonic materials in the field of biomedical applications. Consequently, we carried out a complete characterization of the optical properties, thermoluminescence and photo-stimulated studies that allowed the elucidation of the persistent luminescent mechanism exhibited by the CaS:Eu^{2+}/Dy^{3+} nanophosphors.

Moreover, due to the hygroscopic properties of the nano-host, different surface modification strategies were evaluated to provide water dispersibility characteristics and protection from hydrolysis. Three strategies of surface modification were evaluated: the adsorption of thiol ligands, adsorption of polyvinylpyrrolidone (PVP) and grafting of a silica shell. The latter one provided promising results that led to a preliminary evaluation of these nanophosphors as luminescent probes for *in vivo* optical imaging.

Chapter 2 – Theory

2.1 Bulk Persistent Luminescent Materials

Persistent luminescent (PL) materials have been known over several centuries. The first report of this type of materials is found in an ancient Chinese story concerning a painting of Tsi Tsung, the second Emperor of the Sung dynasty (976-988 A.C).[35] The story was found in the notes written by a Sung monk and it describes a painting that in daylight showed a cow eating grass outside a pen, but during the night the cow appeared resting inside the pen. The monk wrote that to achieve this, the paint used was fabricated by mixing pearl shell with a ground rock found in the seashore next to a volcano.

It was not until 1602 that the first scientific description of a technique to prepare persistent luminescent materials was reported. Vincenzo Casciarolo found that after the calcination of barite ($BaSO_4$), a mineral rich in sulphur collected from Monte Paterno near Bologna, a product that glowed yellow-orange light in the dark was obtained.[36] He described that the product had the capacity to attract the "golden light of the sun" and decided to call it *"lapis solaris".* The interest on this mineral promptly grew and spread throughout Europe. Several references related to the preparation of this after-glowing material, under the names of "Bologna stone" or "*lapis phosphorus*", were found in publications dating back to the 17th century.[37]

In the 18th century, the exploration of different procedures to obtain the Bologna stone led to the discovery of other materials that possessed persistent luminescent properties. That was the case of calcium sulphide (Hoffmann's phosphor), calcium nitrate (Baldewinian phosphor) and strontium sulphide.[36] In the 19th century, Theodor Sidot developed a synthetic procedure for the production of zinc sulphide, also called the "Sidot blend", that would become the most widely used persistent phosphor during the 20th century.[38] In almost all the published work during this period of time, descriptions of different persistent luminescence emission colors are found, notwithstanding the fact that the reports were all for the same material. Thus, authors started to gain insights on the

relationship between the nature of the impurities and the persistent luminescent emission and the duration of the luminescence. However, this was not based on the physical fundamentals responsible for the persistent luminescence phenomena.

Up to the end of the 20th century, the green persistent emission of ZnS:Cu^{+} and ZnS:Cu^{+}/Co^{2+} were the most studied and used in the fields of photoluminescence, cathodoluminescence and electroluminescence. Zinc sulfide was also, the first persistent luminescent phosphor available commercially and used in traffic signs, emergency signage, watch dials, clocks, paintings, textile printing and toys.[39] Despite its popularity, the quest to improve the brightness and persistent luminescence duration of the "Sidot blend" phosphor still remained. As a consequence, radioactive elements (*e.g.* promethium and tritium) were included as dopants in the ZnS host, but it was found that large quantities of material were needed in order to obtain a significant improvement on the duration of the persistent luminescence.[40]

The search for different persistent luminescent materials with improved optical properties continued. In 1996, Matsuzawa *et al*., pioneered the search for new materials and discovered a superior green-emitting persistent luminescent material.[41] The authors reported $SrAl_2O_4$:Eu^{2+}/Dy^{3+} as a novel green-emitting long "phosphorescent phosphor" with higher brightness and significantly longer persistent luminescent duration (~ 10 h) in comparison with ZnS:Cu^{+}, Co^{2+} (~ 0.5 h). This discovery not only pushed the boundaries leading to the discovery of other hosts, such as alkaline earth aluminates, but also to the introduction of lanthanide ions as activators of the persistent luminescent optical phenomenon. Shortly after this discovery, other persistent luminescent materials with blue and green emissions based on alkaline earth aluminates were reported.

Later, it was found that alkaline earth akermanites ($M_2MgSi_2O_7$, M=Ca, Sr, Ba), doped with lanthanide ions exhibited persistent luminescence duration and brightness equal to the alkaline earth aluminates. Other hosts, such as phosphates ($M_2P_2O_7$, M= Ca, Sr) and alkaline earth nitride-silicates ($M_2Si_5N_8$: M=Ca, Sr, Ba) were widely studied for the development of white LEDs due to their high stability towards moisture and heat.[40]

Sulphide based phosphors maintained their privileged place in the development of persistent luminescent materials, as they were the only ones that showed an increased red shift compared to the other hosts offering yellow, orange and red persistent luminescent emissions. However, since they are hygroscopic, they are considered less stable hosts; in addition, they are the ones that show the shortest persistent luminescent duration.[30e] In order to circumvent the drawbacks of the sulphide hosts, yttrium oxysulphide was proposed as a more stable red-shifted host. It was first reported as a red-orange persistent luminescent material using Sm^{3+} as the dopant, with persistent luminescent duration of 0.5 h.[42] Soon after, the persistent luminescent duration was lengthened to 1 h by doping with Eu^{3+}, Mg^{2+} and Ti^{4+} ions.[43] On the other hand, Bessiere *et al*., suggested the use of a biocompatible material $Ca_3(PO_4)_2$ as an alternative to the sulfide hosts. The authors reported that by doping the host with Mn^{2+} and Dy^{3+} (or Tb^{3+}), it was possible to obtain red persistent luminescence (660 nm wavelength) with a persistent luminescence duration of 1 h after irradiation of the material with X-ray.[44]

In the literature more than 200 different host materials can be found, in which persistent luminescence may be induced by intrinsic defects or by co-doping with two types of active centres: emitting ions such as Eu2+ or transition metals such as Mn2+ and Cr3+; and trivalent lanthanide ions to furnish trapping centres.[32a] In Table 2.1 some examples of hosts and dopants used to obtain persistent luminescent bulk materials are listed.

Table 2.1 Some examples of persistent luminescent bulk materials

HOST MATERIAL	DOPANTS [a]	PL MAXIMUM[b] (nm)	PL DURATION[b] (h)	REFERENCES
$SrAl_2O_4$	Eu^{2+}/Dy^{3+}	520	~ 10	[41, 45]
$SrAl_2O_4$	Ce^{3+}	385	~ 10	[46]
$CaAl_2O_4$	Eu^{2+}/Nd^{3+}	430	~ 5	[47]
$CaAl_2O_4$	Ce^{3+}	413	~ 10	[48]
$BaAl_2O_4$	Eu^{2+}/Dy^{3+}	500	~ 2	[49]
$BaAl_2O_4$	Ce^{3+}	450	~ 10	[50]
$Sr_2MgSi_2O_7$	Eu^{2+}/Dy^{3+}	470	~ 10	[51]
$Ca_2MgSi_2O_7$	Eu^{2+} or Tb^{3+}	515/535	~ 5	[52]
$Ca_2MgSi_2O_7$	Dy^{3+}	White (480 + 575+667)	~ 3	[53]
$Ba_2MgSi_2O_7$	Eu^{2+}/Tm^{3+}	505	~ 5	[54]
$Ba_2MgSi_2O_7$	Mn^{2+}/Ce^{3+}	408	~ 2	[55]
$Sr_2P_2O_7$	Eu^{2+}/Y^{3+}	420	~ 8	[56]
$Ca_2P_2O_7$	Eu^{2+}/Y^{3+}	415	~ 6	[57]
$CdSiO_3$	Mn^{2+}	580	~ 2.5	[58]
$SrSiO_3$	Dy^{3+}	White (480 + 572 + 664)	~ 1	[59]
$Ca_2Si_5N_8$	Eu^{2+}/Tm^{3+}	620	~ 1	[60]
CaO	Eu^{3+}	594	~ 2	[61]
SrO	Pb^{2+}	390	~ 1	[62]
ZnS	Cu^{+}	530	~ 3	[39]
CaS	Eu^{2+}/Tm^{3+}	650	~ 1	[63]
BaS	Cu^{+}	610	~ 0.5	[64]
$CaGa_2S_4$	Eu^{2+}/Ho^{3+} (or Ce^{3+})	555	~ 0.5	[65]
$CaSi_2S_4$	Eu^{2+}/Nd^{3+}	660	~ 0.5	[66]
Y_2O_2S	$Eu^{3+}/Mg^{2+}/Ti^{4+}$	611	~ 1	[43]
Y_2O_2S	Sm^{3+}	610	~ 0.5	[42]
Gd_2O_2S	Sm^{3+}/Ti^{4+}	607	~ 1	[67]
$Ca_3(PO_4)_7$	$Mn^{2+}/Tb^{3+}/Dy^{3+}$	660	~ 1	[44]

[a] Dopant ions used to furnish trapping sites are *italicized*.

Different procedures have been reported to synthesize bulk persistent luminescent materials. The flux method, a solid-state reaction, is the most commonly used.[40, 68] It is carried out *via* annealing at high temperatures (>1000 °C) a mixture of salt precursors in the presence of another salt with a lower melting point that acts a high temperature solvent. At high temperatures, all reactants melt and diffuse easily leading to the formation of the desired host with high crystallinity.

Another widely used synthetic procedure is the combustion method, since it leads to the instantaneous formation of products.[69] At low igniting temperatures (~500 °C), persistent luminescent materials are formed by the heat liberated by the redox exothermic reaction between precursor metal salts and a fuel such as urea. Another fast-synthetic route to obtain this type of materials is the microwave route. In this process, precursor metal salts or oxides are ground and placed in a microwave reactor.[70]

An alternative "low temperature" procedure is the Pechini method, a sol-gel synthesis, in which precursor metal salts dissolved in water are mixed with citric acid and a polymer such as polyethylene glycol. The presence of the citric acid leads to the formation of citrate complexes, thus uniform distribution of the precursor ions in the solution is achieved. The mixture is heated to obtain a polymer citrate gel. The gel is then dried and annealed to obtain persistent luminescent fine powders.[71]

2.2 Nano-sized Red Persistent Luminescent Materials

The optical properties of persistent luminescent materials with emission in the biological optical transparency window attracted the attention of researchers that were developing luminescent probes for bioimaging. With this type of materials, fluorescent optical imaging could be carried out without the use of external excitation hence, eliminating auto-fluorescence thereby providing an improvement in the signal to noise ratio. Moreover, in this region light attenuation is predominantly due to scattering rather than absorption. Light scattering occurs due to the different refractive indices exhibited by the different components of the tissues. The scattering coefficient is defined as the probability of a photon scattering in tissue per unit per length, and in general as the

wavelength of light is increased the scattering coefficient decreases. Thus, in the biological optical transparency window light scattering is significantly lower than in the UV-Vis region.[12c] Hence, it provides an increase in the penetration depth. Despite the promising applications for these type of materials, there are a significant low number of hosts that could offer a persistent luminescent emission in the biological optical transparency window. Additionally, the persistent luminescence decay time of these hosts is significantly shorter than that of persistent luminescent materials with emission in the blue or green spectral regions.[30e]

Materials that are included in the nano-regime (particle size < 100 nm) are highly preferred for biomedical applications such as bioimaging since their size is in the range where different important biological processes can be studied. Furthermore, they offer a large surface area that is amenable to functionalization with possible targeting ligands and therapeutic agents. However, the currently used synthetic approaches produce particles well outside the boundary of the nano-regime and/or the persistent luminescence emissions are not within the biological optical transparency window. Table 2.2 summarizes the most relevant references found on the synthesis, characterization of red persistent luminescence nanomaterials (620 nm to 750 nm) that have been proposed as optical imaging probes.

Table 2.2 List of reported red persistent luminescence nanomaterials

HOST MATERIAL	DOPANTS[a]	PL MAXIMUM (nm)	PL DURATION	AV. SIZE (nm)	REFERENCES
Gd_2O_2S	$Eu^{3+}/Mg^{2+}/Ti^{4+}$	710	> 15 min	65	[72]
$CaMgSi_2O_6$	$Eu^{2+}/Mn^{2+}/Pr^{3+}$	685	~ 1 h	140	[73]
$CaMgSi_2O_6$	Mn^{2+}/Dy^{3+}	680	~ 1 h	125	[74]
$Ca_3(PO_4)_2$/Hap[b]	$Eu^{2+}/Mn^{2+}/Dy^{3+}$	670	> 10 min	Mixture[c]	[32c]
$Ca_{0.2}Zn_{0.9}Mg_{0.9}Si_2O_6$	$Eu^{2+}/Mn^{2+}/Dy^{3+}$	690	~ 1 h	75	[75]
$MAlO_3$(M=La, Gd)	Mn^{4+}/Ge^{4+}	730	~ 20 h	500	[76]
$ZnGa_2O_4$	Cr^{3+}	695	~ 1.5 h	150	[33]
$LiGa_5O_8$	Cr^{3+}	719	~ 1 h	120	[77]

[a] Dopant ions used to furnish trapping sites are *italized*.
[b] HAp:Hydroxyapatite
[c] Mixture of nanorods (Long axis: 30 nm-120 nm and wide axis: 20 nm and nanospheres: 10 nm -20 nm)

The most widely used synthetic procedures to obtain persistent luminescent nanoparticles are the hydro(solvo)thermal method, the co-precipitation and the sol-gel processes. In the first approach, precursors of the hosts and dopants are solubilized in a solvent at pressure and temperature conditions above the critical point of the solvent thus, favouring the rate at which the nanoparticles grow. In the reaction mixture, stabilizing ligands such as small molecules (e.g. sodium citrate and cytrimethylammonium bromide), or organic polymers such as polyethylene glycol and polyethylamine are present to control the particle growth as well to yield water dispersible nanoparticles.[78]

Co-precipitation method is a wet-chemical technique in which saturation of the precursors species lead to seed formation and particle growth *via* Ostwald ripening. Typically, for this synthetic route low temperatures (< 100 °C) are used, yielding nanoparticles with low crystallinity. The as-synthesized nanoparticles then require an annealing treatment at higher temperatures (500°C - 900°C) in order to improve their crystallinity, which also results in increasing their luminescence efficiency.[40, 79] The sol-gel method is a wet chemical technique in which nanoparticles dispersed in a solvent (sol) are integrated in a polymeric network (gel) *via* hydrolysis and polycondensation reactions. Next, a drying process is carried out to remove the liquid phase from the gel, followed by an annealing treatment to improve the crystallinity of the nanomaterial produced. [40, 75, 80]

2.3 Proposed Mechanisms of Persistent Luminescence

Notwithstanding, the fact that persistent luminescence materials have been known for several centuries, very little was reported on the physical principles that explain the persistent luminescence phenomenon. This particular optical property was confused with the phosphorescence due to the long emission times.[81] The mechanism of phosphorescence decay involves an organic molecule decaying *via* a metastable state, which is a triplet. The decay scheme is shown in Figure 2.1. The decay from the higher singlet to the triplet is by a non-radiative transition, which involves the crossing of potential energy curves known as intersystem crossing. The decay from the triplet to the ground state singlet is forbidden by spin symmetry and therefore is slow.

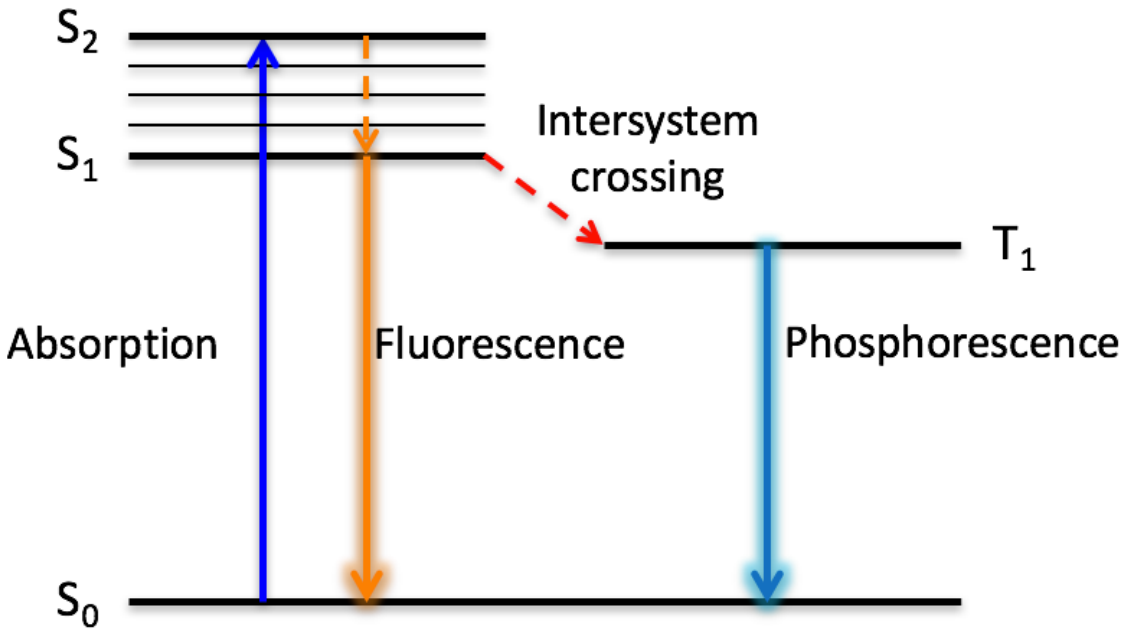

Figure 2.1 Scheme of the mechanism of fluorescence and phosphorescence.

Contrary to the well-understood process of phosphorescence, different mechanisms have been postulated to explain the persistent luminescence phenomenon. The first persistent luminescent mechanism proposed the co-existence of emitting centres and long lifetime meta-stable energy levels, also referred as 'traps' located within the band gap of the host. Upon high energy excitation, charge carriers (electrons or holes) from the emitting centres are retained in the traps. Once the excitation has subsided, the electrons are gradually released returning to the emitting centres resulting in a delayed luminescence (Figure 2.2).[40]

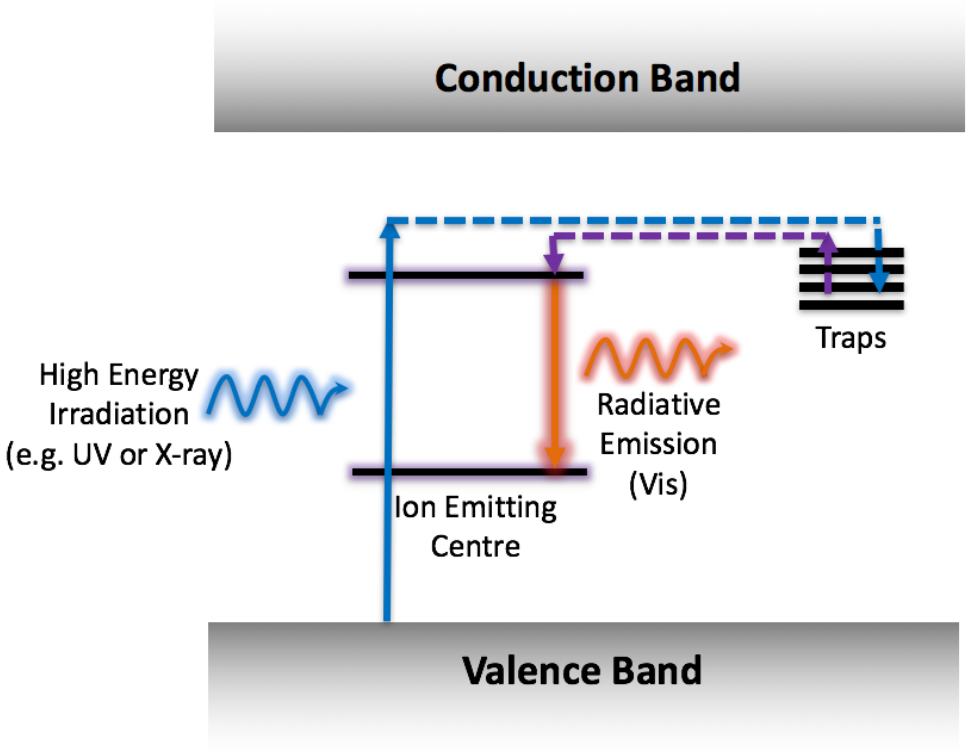

Figure 2.2 Scheme of the PL mechanism generally agreed before the discovery of Matsuzawa *et al*.

In 1996, Matsuzawa *et al*., reported the synthesis of $SrAl_2O_4:Eu^{2+}/Dy^{3+}$. The authors also proposed a more detailed model of the mechanism responsible for the persistent luminescence of this material and assigned the nature of the charge carriers and traps. The proposed model was based on experimental results obtained from photoconductivity measurements. Figure 2.3 shows the scheme of the proposed PL mechanism, which is known as the Matsuzawa model.[41]

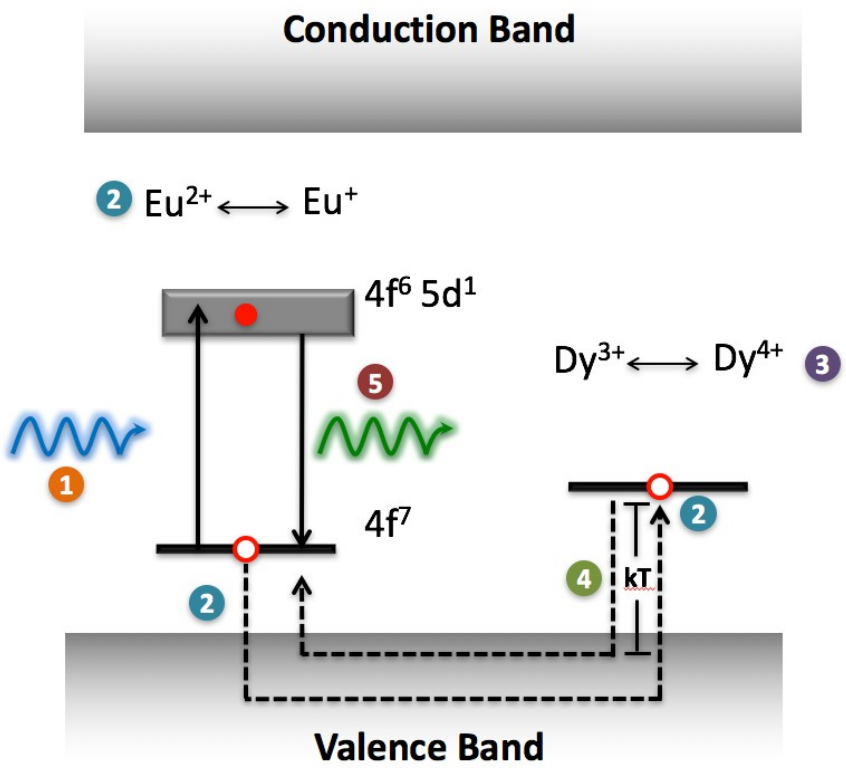

Figure 2.3 Scheme of the persistent luminescence mechanism proposed by Matsuzawa *et al.* for $SrAl_2O_4:Eu^{2+}/Dy^{3+}$. Figure adapted from reference [41].

The Matsuzawa model postulated that upon high energy irradiation of the host, an electron in the ground state of the Eu^{2+} ion is excited to the $4f^65d^1$ energy levels; leaving a 'hole' in the ground state (Step 1). This hole can escape to the valence band, causing a change in the oxidation state of europium ($Eu^{2+} \rightarrow Eu^{+}$) (Step 2). This 'hole' is then captured by the trivalent lanthanide ion (Dy^{3+}) reducing it to Dy^{4+} (Step 3). The trapped hole is released back into the valence band, a process activated by thermal energy (Step 4). From the valence band the trapped hole can combine with an Eu^{+} ion to form Eu^{2+} and return to the ground state with the emission of a photon (Step 5).

After the publication of Matsuzawa *et al.*, several publications on novel persistent luminescent materials were reported using this model to explain the optical phenomenon observed.[49b, 51, 52b, 82] However, this model did not provide an adequate explanation of the persistent luminescence observed in undoped and singly doped hosts. As well, due to the increasing interest in these materials, careful attention was being paid to the experimental

results obtained from thermoluminescence and electron paramagnetic resonance studies with the aim to confirm the proposed mechanism and the formation of Eu^{+} and Dy^{4+} species.[40]

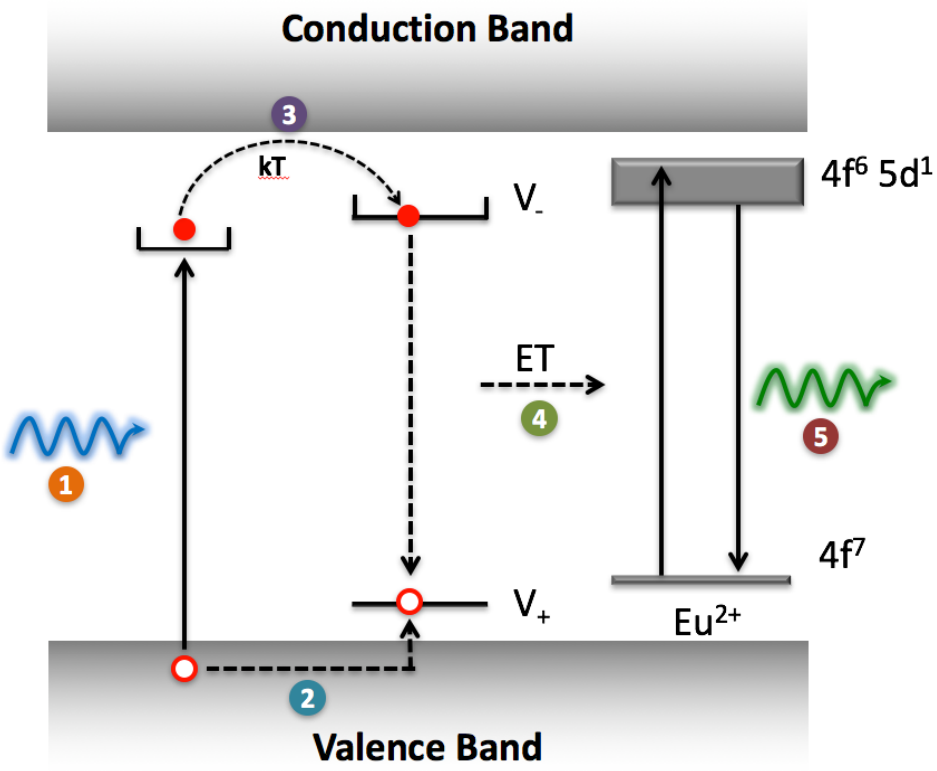

Figure 2.4 Scheme of the persistent luminescence mechanism proposed by Aitasalo *et al.* for $CaAl_2O_4:Eu^{2+}/Dy^{3+}$. Figure adapted from reference [68b].

In 2001 Aitasalo *et al.,* proposed a mechanism based on results from luminescence and thermoluminescence studies carried out on $CaAl_2O_4:Eu^{2+}/Dy^{3+}$. The scheme of the Aitasalo's model to explain the persistent luminescence mechanism is shown in Figure 2.4. Upon UV irradiation, electrons from the valence band are excited and trapped by anionic vacancies before reaching the conduction band (Step 1). The excitation of the electron, causes the formation of a hole in the valence band. This hole can be easily trapped by cationic vacancies located above the valence band (Step 2). Thermal energy can liberate the electron trapped from one anionic vacancy that can be re-trapped by a nearby vacancy (Step 3). The electron trapped can recombine with the hole trapped in the cationic vacancy

releasing energy that is transferred directly to the Eu^{2+} ion (Step 4) resulting in the emission of a photon (Step 5).

The model proposed by Aitasalo *et al.*, explained the persistent luminescence observed in single doped and co-doped materials. The authors suggested that the presence of co-dopants increased the number of lattice defects, leading to the lengthening of the duration of the persistent luminescence duration.[68b] Additionally, the mechanism does not suggest the formation of chemically unstable ions such as Eu^{+} and Dy^{4+}.

In 2003, Aitasalo *et al.*, reported that blue persistent luminescence (430 nm) of $CaAl_2O_4:Eu^{2+}/Nd^{3+}$ could be induced with UV and Vis light (530 nm).[83] The authors showed the presence of long-lived intermediate and shallow traps located close to the conduction band. They proposed that upon 530 nm irradiation, electrons from the valence band are excited to an intermediate trap level. As the irradiation process continues, the electron can be liberated from the intermediate trap and excited to a higher shallow trap. The trapped electron can be further liberated from the shallow trap and recombine in the energy levels of an Eu^{2+} ion, generating the blue persistent luminescence. This observed blue PL after irradiation with green light could not be explained through the model proposed by Matsuzawa et al. In his model, the trapped holes are originated from the Eu^{2+} ion. This generates low-energy photons that cannot fill the energy gap needed to generate higher in energy persistent luminescence emission.

Albeit the answers provided by this mechanism, the process requires that the anionic and cationic vacancies as well as the emitting Eu^{2+} ions be "relatively close" to each other for the persistent luminescence to occur. Thus, this mechanism is limited since it will only occur if electron migration is favoured.

In 2004, Dorenbos expressed some apprehension with respect to the formation of Eu^{+} and Dy^{4+}, to explain the mechanism for persistent luminescence. Thus, Dorenbos began to develop a model to predict the absolute location of the energy levels of Ln^{2+} and Ln^{3+} (Ln: Lanthanide) relative to the valence and conduction band.[84] Initially, he used two hosts, CaF_2 and YVO_4, to demonstrate the validity of his model, and later he improved his model,

which has been used to predict the location of Ln^{2+} and Ln^{3+} energy levels in more than 100 hosts.[85]

Calculations using the Dorenbos model to predict the location of Eu^{2+} in aluminate and silicate hosts revealed that the lowest 5d levels of this ions are located close and below the conduction band in both hosts (approximately ≈0.017 eV below the conduction band). In general, Ln^{2+} excited d-levels are located near the edge of the conduction band. Thus, by thermal activation the electrons excited to the 5d levels can be promoted to the conduction band, favouring electron migration towards trapping sites.[84a] With this knowledge Dorenbos proposed the persistent luminescence mechanism shown in Figure 2.5, in which electrons are considered to be the main charge carriers.

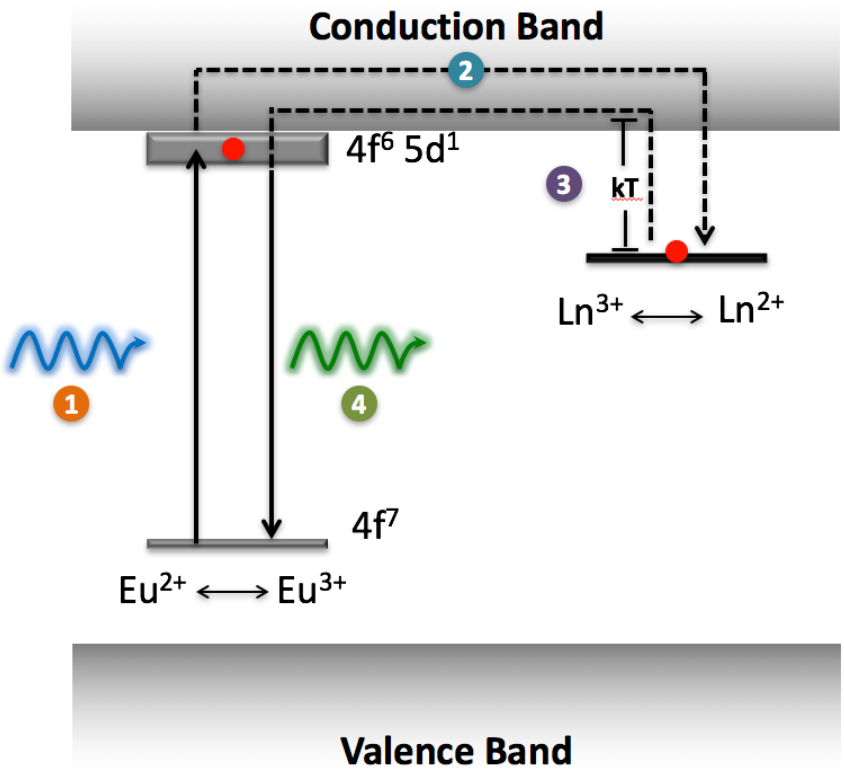

Figure 2.5 Scheme of the persistent luminescence mechanism proposed by Dorenbos *et al.* for aluminates and silicates codoped with Eu^{2+} and Ln^{3+}. Figure adapted from reference [84a].

Upon irradiation, an electron is excited from the $4f^7$ level to the $4f^6\ 5d^1$ excited energy level (Step 1). Since the excited energy level lies close to the conduction band, the excited electron is thermally stimulated to the conduction band and subsequently "caught" by a Ln^{3+} co-dopant (Step 2). Thus, an oxidation ($Eu^{2+} \rightarrow Eu^{3+}$) / reduction ($Ln^{3+} \rightarrow Ln^{2+}$) process occurs leading to the formation of more stable species. If the Ln^{2+} trapping site is near the conduction band, at room temperature, the trapped electron can be released back to the conduction band (Step 3). Subsequently, the electron migrates back to the Eu^{2+} luminescent centre producing a persistent luminescence emission (Step 4).

The model developed by Dorenbos has facilitated the design of persistent luminescent materials, since it allowed to recognize which Ln^{3+} co-dopants could reduce or lengthen the PL emission at room temperature depending on their location below the conduction band. Ln^{3+} located no further than 0.5 eV below the conduction band could be easily emptied at room temperature conditions, favouring long PL emissions. On the contrary, deeper bands will require higher energy sources thus, drastically reducing the PL observed at room temperature.[84a] The PL mechanism suggested by Dorenbos and supported by experimental and computational results, justified the persistent luminescence in codoped materials, however, it did not explain its existence in undoped and single doped materials.

For the same reasons as Dorenbos, Claubau *et al*., did not accept Matsuzawa's model. They carried out electron paramagnetic resonance experiments to study the PL observed in $SrAl_2O_4:Eu^{2+}/Dy^{3+}$.[86] The authors reported that upon UV excitation, the Eu^{2+} concentration decreases followed by an increase as soon as the irradiation is terminated. They also reported on the presence of trace amounts of Eu^{3+} but did not find any evidence for the presence of Dy^{2+} ions or any variation in the concentration of Dy^{3+}. Thus, the authors acknowledged that Eu^{2+} participates in the trapping process and that electrons are the charge carriers as proposed by Dorenbos. However, they attribute the nature of the traps to anionic vacancies located near the photo-generated Eu^{3+} ions. These defects are created by charge compensation due to the substitution of the divalent cation by Ln^{3+}. Based on the

experimental results, Claubau *et al*., proposed a persistent luminescence mechanism shown in Figure 2.6.

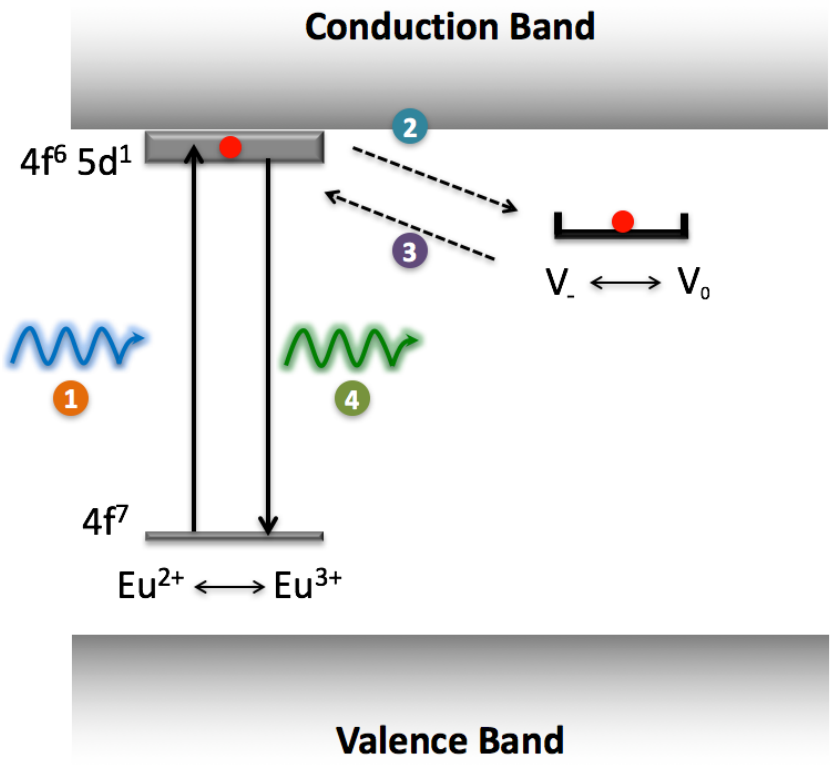

Figure 2.6 Scheme of the persistent luminescence mechanism proposed by Clabau *et al*. for $SrAl_2O_4:Eu^{2+}/Dy^{3+}$. Figure adapted from reference [86].

The authors proposed that upon UV irradiation, an electron of Eu^{2+} is excited from the $4f^7$ to $4f^65d^1$ excited energy level (Step 1). The electron does not migrate through the conduction band, rather *via* direct transfer moves into an anionic vacancy. Therefore, Eu^{2+} is oxidized to Eu^{3+} and the negative vacancy (V_-) is neutralized (V_0) (Step 2). At room temperature, the thermal energy is sufficient to induce the de-trapping of the electron directly to the 5d levels of Eu^{2+} (Step 3), followed by emission (Step 4).

Notwithstanding, that this model could be extended to explain the intrinsic persistent luminescence observed in undoped materials, and provide a better understanding of the nature of the traps, electron migration is still required with the necessity that the Eu^{2+} ions and the anionic vacancies be in close proximity.

In 2006, Aitasalo et al., reported the results obtained from the thermoluminescence studies carried out on $CaAl_2O_4:Eu^{2+}/Ln^{3+}$ (Ln^{3+}= La to Lu) to characterize its blue persistent luminescence.[87]. Based on their results the authors proposed a new mechanism that incorporated the ideas from the mechanisms proposed by Dorenbos and Claubau *et al*. Aitasalo et al., included the migration of electrons through the conduction band, and the nature of the traps, both lattice defects and/or Ln^{3+} energy levels. This model has become the generally accepted and the mechanism is shown in Figure 2.7.

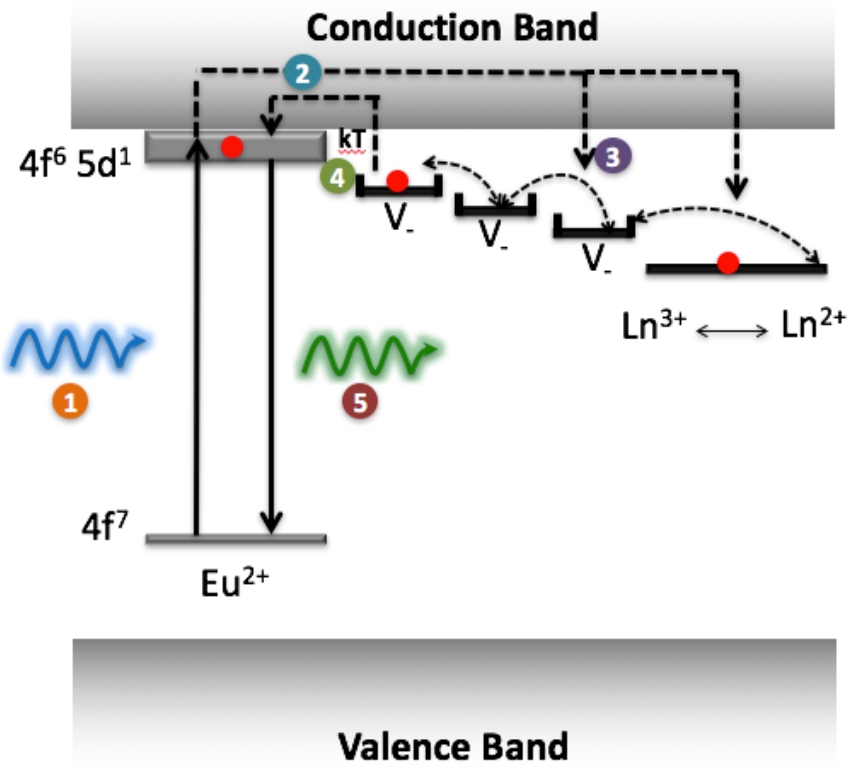

Figure 2.7 Scheme of the second persistent luminescence mechanism proposed by Aitasalo *et al*. for $CaAl_2O_4:Eu^{2+}/Ln^{3+}$. Figure adapted from reference [87].

The mechanism proposes that upon high energy irradiation, an electron from the ground state of Eu^{2+} is excited to the 5d level (Step 1). By thermal-stimulation, the electron is promoted to the conduction band and migrates to the trapping sites (Step 2). The electron may be trapped by either anionic vacancies or Ln^{3+} energy levels. The electron can be liberated or re-trapped by another trapping site until it reaches a trap located close to

the conduction band (Step 3). The electron is liberated back to the conduction band at room temperature and it migrates and recombines in the 5d level of Eu^{2+} (Step 4). This is followed by the radiative transition $4f^6 5d^1 \rightarrow 4f^7$ (Step 5).

2.4 Defects: The Nature of the Trapping Sites

Crystalline nanoparticles are defined as an assembly of atoms in an ordered and periodic array. However, the formation of defects is an entropically favored process that occurs during the growth and processing (*e.g.* annealing) of the nanocrystal.[88] These defects cause a disturbance in the ordering of the atoms, reducing the crystallinity of the nanoparticles. The degree of crystallinity of the nanoparticles have a significant impact on the electrical, magnetic and optical properties. In the case of the luminescent nanoparticles, it is generally accepted that the intensity of the emission increases with the amelioration in the crystallinity. A characteristic of nanoparticles is the high surface to volume ratio. This results in surface defects which affect the optical properties of the crystal. Depending on the nature of the defect that are located in close proximity to an emission centre, defects may cause a shift in the emission wavelength, a quenching of the emission, or the defect itself may act as an emission centre (*e.g.* impurities or dopants).[89] In the particular case of persistent luminescent, defects have been associated to the duration of the emission of light under no irradiation and to the intrinsic afterglow observed in undoped and single doped materials.[30e, 31, 73]

Defects are classified by their dimensions with respect to the crystal. Extended defects are imperfections that disrupt the crystal periodicity in more than one dimensions (*e.g.* dislocations, grain boundaries, precipitates, voids and inclusions) whereas point defects are defined as 0-dimensional that disrupt the crystal periodicity at one lattice site.[90] The latter have being attributed to play a major role in the persistent luminescent phenomenon.

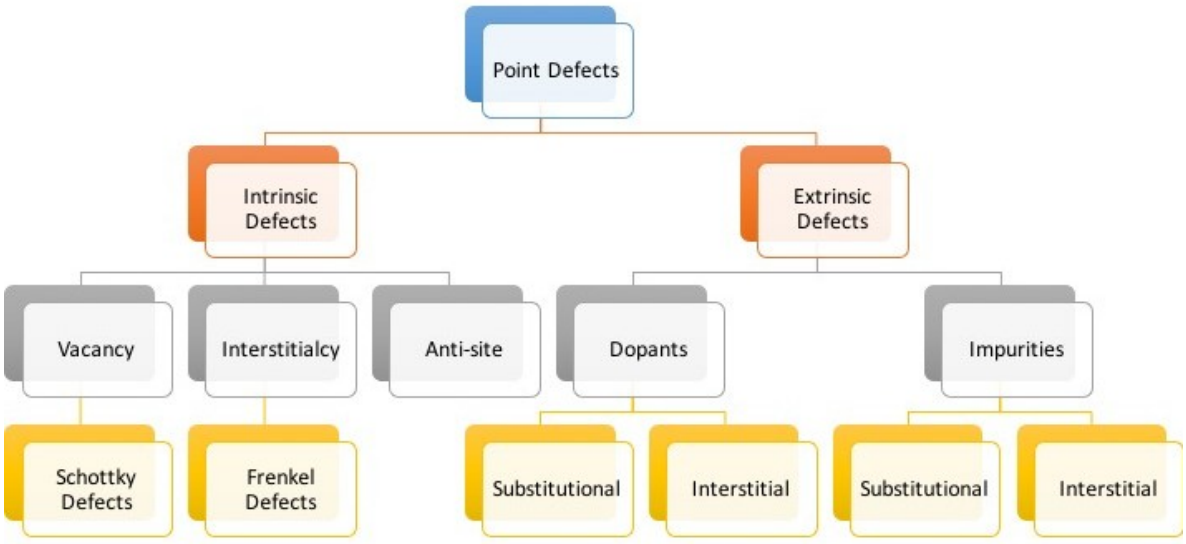

Figure 2.8 Classification of point defects in crystals

The classification of point defects is shown in Figure 2.8. Point defects generated by an entropically favored process in crystals are known as intrinsic defects whereas defects that are created as consequence of introducing dopants or incorporation of impurities during the crystal growth are identified as extrinsic defects.[90b, 91]

There are three types of intrinsic defects:[91b]

a) *Vacancy.* it is defined as a vacant lattice site, due to an atom missing from its corresponding crystal site (Figure 2.9A). In the Kröger-Vink notation a vacancy is denoted by the symbol V. It is accompanied by a superscript that identifies its net charge and a subscript that indicates the nature of the site in the crystal. Vacancies are considered to govern the charge neutrality of the crystal. The presence of a vacancy disrupts the local charge balance of the crystal. To re-establish the neutrality, a vacancy of the opposite charge may form to compensate the charge build up. Paired vacancies of opposite charge are known as a Schottky defect (Figure 2.9B). In addition, the charge build up can also be minimized by the formation of a color centre, referred to as an F-centre (F stands for *'farbe'*, the german word for color). An F-centre is defined as an electron trapped by the electric field of an anionic vacancy (Figure 2.9C). The presence of

color centres give rise to energy levels located in the bandgap of the crystal and the manifestation of optical bands.[92]

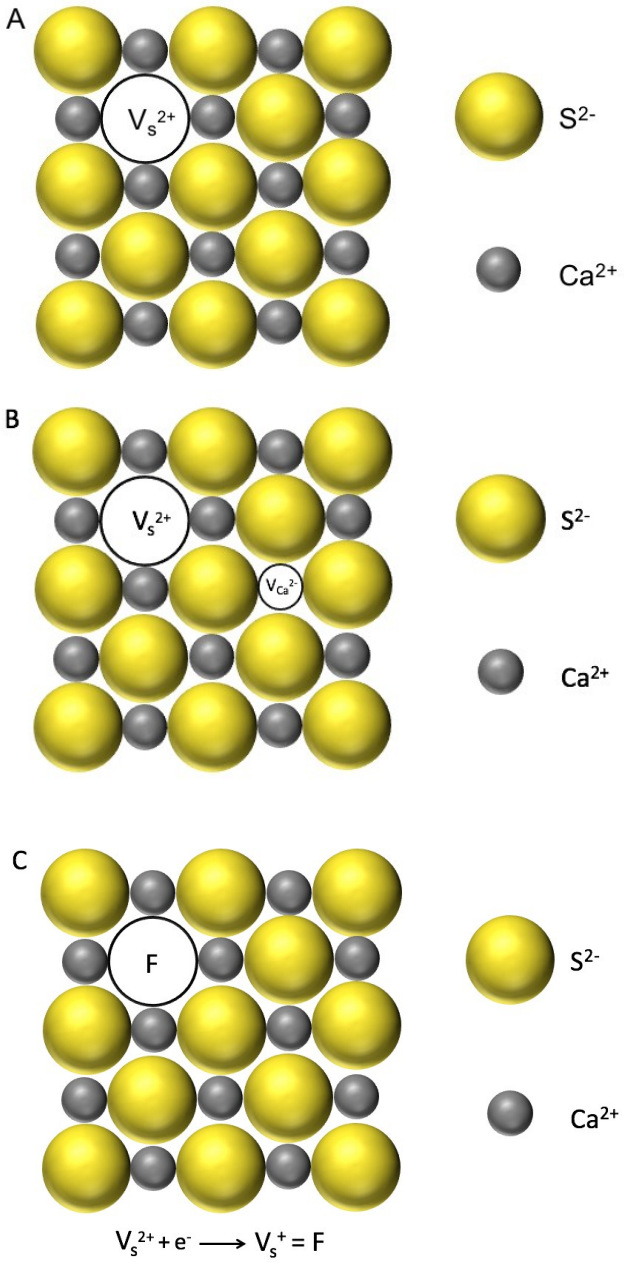

Figure 2.9 Two-dimensional representation of (A) an anionic vacancy, (B) a Schottky defect and (C) a F-Center in CaS.

b) *Interstitialcy.* This type of defect occurs when an atom occupies a normally unoccupied site in the crystal structure (Figure 2.10A). Due to the unfavorable bonding conditions and limited space, this type of defect is significantly less common than the vacancies. They are generated to compensate the charge build up created by a vacancy of the same charge as the interstitial atom. This paired vacancy-interstitialcy is known as a Frenkel defect (Figure 2.10b). In the Kröger-Vink notation an interstitial is denoted with the symbol I accompanied of a subscript that indicates the nature of the atom at the interstitial site.

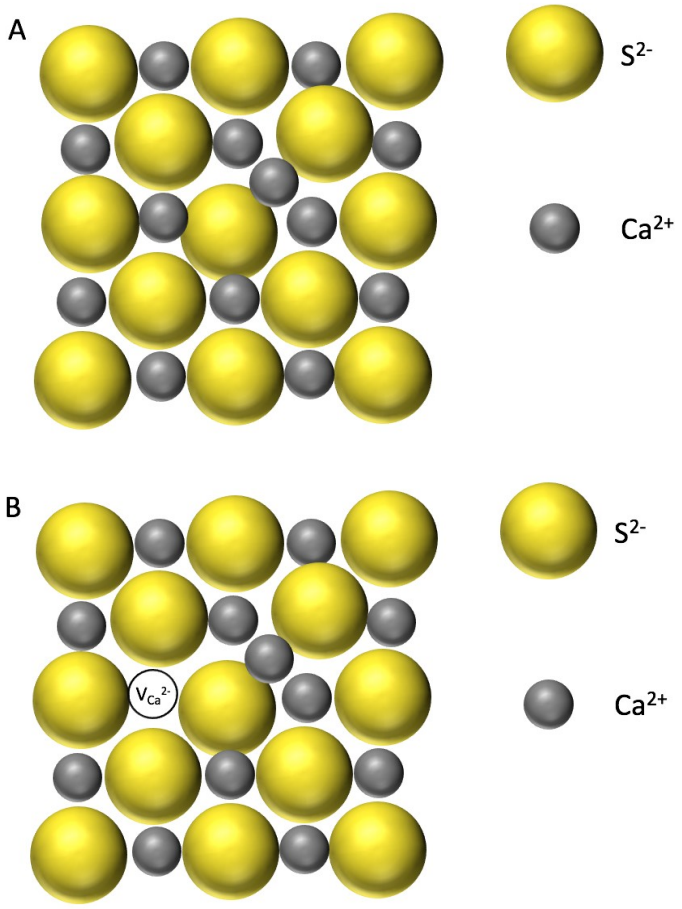

Figure 2.10 Two-dimensional representation of (A) an interstitialcy and (B) a Frenkel defect in CaS.

c) *Anti-site Defects.* It occurs when two ions of opposite charge exchange position (Figure 2.11). This type of defect is found in less strongly ionized compounds such as GaAs.[93]

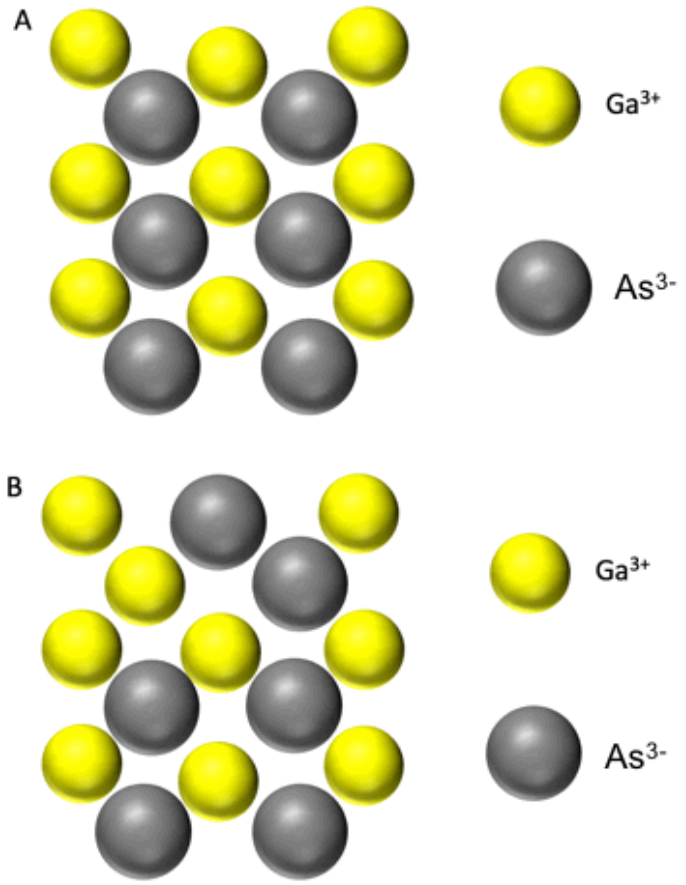

Figure 2.11 Two-dimensional representation of (A) GaAs and (B) an anti-site defect in GaAs.

Extrinsic defects are formed as consequence of the non-intentional introduction of impurity ions. Whereas when ions are purposefully introduced they are known as dopants or solutes. The foreign ions can occupy a lattice site by replacing another of similar ionic radius. In addition, ions with small ionic radii or small diatomic molecules can be incorporated at interstitial sites. In both cases, formation of defects may occur as the crystal undergoes organization. However, the probability of the generation of defects increases if the oxidation state of the dopant (or impurity) differs from that of the ion present at the

substitution site. The difference in the local charge resulting from the substitution needs to be compensated by the formation of electron-hole trapping sites in the crystal.

Figure 2.12 shows how the introduction of a monovalent impurity ion (X^+) or a trivalent dopant ion (Z^{3+}) lead to the formation of trapping sites in CaS. The replacement of any of the impurity ions into a Ca^{2+} lattice site may occur by exchange of an equivalent number of ions or by charge conservation.[94] In the scenario when X^+ is introduced as impurity, if the substitution occurs by an equivalent number of atoms, a X^+ ion replaces a Ca^{2+} ion the local charge of the crystal is +1. To neutralize the charge imbalance in the crystal a hole is required. A hole is simply defined as the absence of an electron thus a hole is positively charged.[95] However, if the substitution occurs whereby, $2X^+$ ions substitute into the Ca^{2+} sites, two Ca^{2+} ions are removed resulting in a charge imbalance of +2. As consequence, a sulfur vacancy is created. This vacancy can trap electrons due to the positive electrical field surrounding it.

In the scenario when a Z^{3+} dopant ion is introduced to occupy a Ca^{2+} lattice site and the replacement occurs by charge conservation ($2Z^{3+} \rightarrow 3Ca^{2+}$), a cationic vacancy will be formed. As this vacancy is surrounded by a negative electrical field, holes (positive charge carriers) can be trapped within. On the other hand, if the replacement occurs by number conservation ($2Z^{3+} \rightarrow 2Ca^{2+}$), an excess of local charge (+1) will be formed, that can only be neutralized by the trapping of an electron. Thus, an electron trapping site is formed.

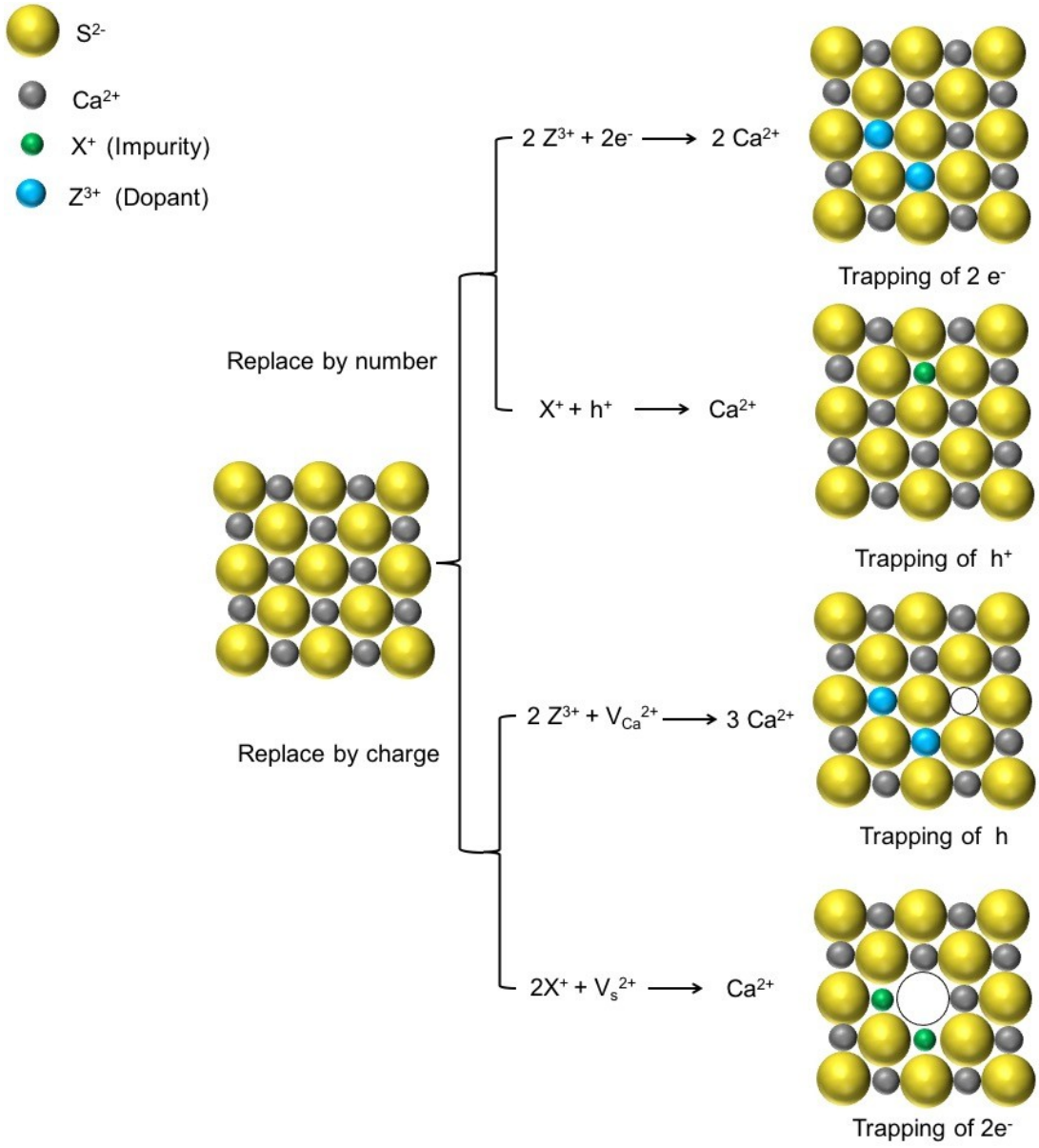

Figure 2.12 Scheme of the formation of trapping sites in CaS by the introduction of a X^{+} impurity and a Z^{3+} dopant.

2.5 Calcium Sulfide as a Host and Lanthanide Ions as Dopants

Inorganic materials exhibit an energy-band structure composed of a valence and a conduction band. The valence band is the band made up of the occupied molecular orbitals whereas the conduction band is the band of orbitals that are high in energy and are generally empty. The energy difference between the top of the valence band and the bottom of the conduction of band is known as the bandgap.[95] The bandgap determines the electrical conductivity of the material (Figure 2.13). When there is an overlap of the conduction and valence band or they are in close proximity (< 1 eV), electrons can easily transfer from the valence to the conduction band, conducting electrical current. Materials showing this band structure are known as conductors. When the bandgap value is in between 1 to 3 eV, electrons can be promoted from the valence to the conduction band by thermal or photo stimulation. These materials are known as semiconductors. When the bandgap is larger than 3 eV, electrons cannot be promoted from the valence to the conduction band thus, no electrical conductivity is generated, and the material is considered an insulator.

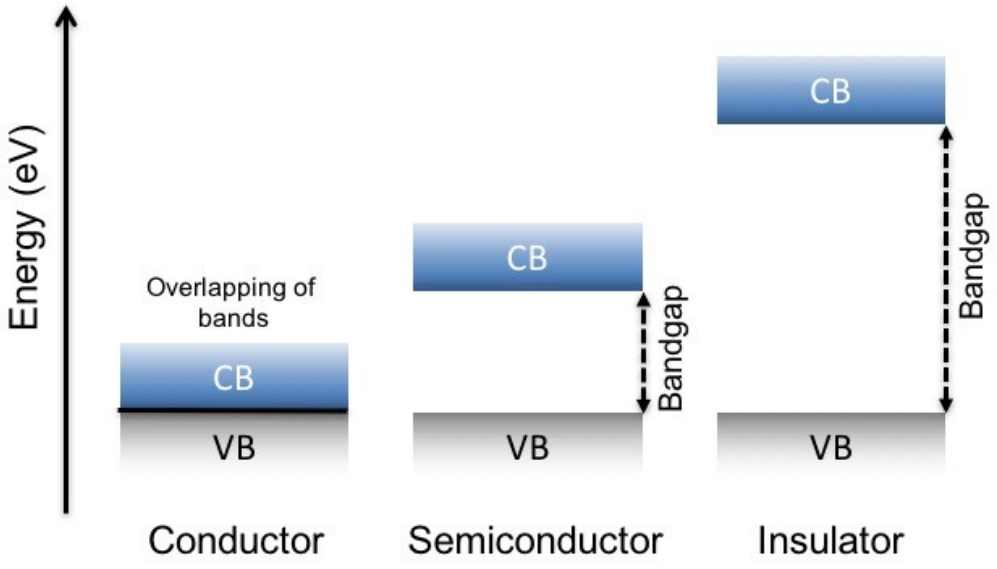

Figure 2.13 A comparison of the bandgaps of conductors, semiconductor and insulator materials. VB and CB denote valence and conduction band respectively. Figure adapted from reference [67].

Persistent luminescent materials are based on insulator inorganic materials that exhibit bandgap values greater than 4 eV.[40] When an optically active dopant ion (ion emitting centre) is incorporated in an inorganic host , the energy levels of the dopant ion are found in the bandgap. Eu^{2+} is one of the most used ion incorporated in insulator inorganic host to produce materials that exhibit persistent luminescent. Eu^{2+} belongs to the group of stable divalent lanthanide ions ($Yb^{2+,}$ Sm^{2+} and Tm^{2+}) that show relatively low electron affinity and exhibit the intraconfigurational $[Xe]4f^n \rightarrow [Xe]4f^{n-1}5d$ transitions. These transitions are characterized by high oscillator strengths, short lifetimes and broad absorption and emission bands. The positions of the 5d energy levels of Eu^{2+} dopant ion are strongly affected by the environment provided by the host in which it has been incorporated. Two important factors influence their location in an insulator host:[96]

I. *The nephelauxetic effect*. Jorgensen studied the nephelauxetic effect, the so-called cloud expansion effect.[97] The effect describes the decrease in the interelectronic repulsion in going from the free ion to the crystalline state. It has been shown that the expansion of the d electron cloud overlap with the ligand atom orbitals thus providing paths by which the d electrons can escape to some extent from the metal ion. In the case of the divalent lanthanides the 5d electron cloud becomes more delocalized over the surrounding ligands causing a decrease in the energy difference between the ground state ($4f^n$) and the $4f^n5d^n$ excited state is decreased (Figure 2.14). Common ligands have been arranged in the order of ability to induce cloud expansion. The order is generally independent of the metal ion similarly to the spectrochemical series. The order reflects the ligands capacity to decrease the energy difference between the 5d and the 4f ground state.[85]

$$F^- < O^{2-} < Cl^- < Br^- < I^- < S^{2-}$$

II. *The crystal field effect.* The 5d orbitals in the free ion are degenerate, however when the ion is introduced in a host, the surrounding ligands can cause the splitting of the 5d energy levels (xy, xz, yx, x^2-y^2 and z^2). The splitting is determined by the coordination number, the ion-ligand distance and the charge of the ligand. In highly

symmetric environments (*e.g.* octahedral and tetrahedral) the 5d orbitals split into two groups (e_g and t_{2g}) (Figure 2.14), whereas in lower symmetric environments (*e.g.* linear and square planar) split into more than two groups. Furthermore, at low coordination number, small distances have been observed between the ion and the surrounding ligands favoring a large crystal field splitting. The spectrochemical series, shown below, arranges the ligands by their capacity to split the d-orbitals, a large splitting is associated to strong field ligands. The strength of the field increases from left to right.

$$O_2^{2-} < I^- < Br^- < S^{2-} < SCN^- < Cl^- < N_3^- < F^- < NCO^- < OH^- < C_2O_4^{2-} \approx H_2O < NCS^- < CH_3CN < NH_3 < NO_2^- < CN^- \approx CO$$

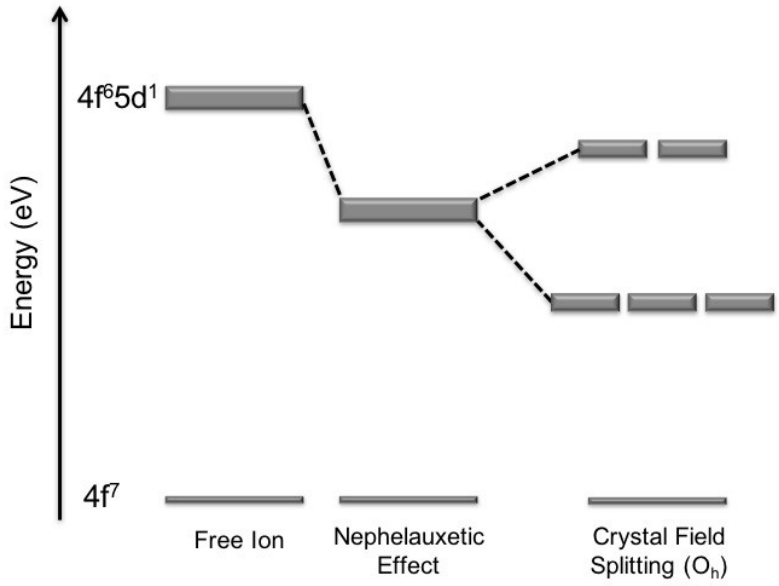

Figure 2.14 The influence of the nephelauxetic effect and the crystal field splitting on the 5d energy levels of a divalent lanthanide ion.

Most persistent luminescent materials contain Eu^{2+} as the emitting dopant ion in oxide base hosts. Consequently, most of the persistent luminescent materials exhibit green and blue emissions due to the nephelauxetic effect and the low crystal field splitting of the 5d energy levels offered by oxygen as the surrounding ligand. A larger crystal field splitting is offered by the S^{2-} ligand, leading to a significant red-shift of the Eu^{2+} emission compared

to the free ion transition. Thus, sulfide based host doped with Eu^{2+} ions exhibit persistent luminescent spanning from the yellow to the red region.

Alkaline earth sulfide hosts such as CaS doped with Eu^{2+} ions exhibit red persistent luminescence with a maximum at 650 nm. CaS is ionic with a rock-salt structure with a space group $Fm\bar{3}m$ and a reported lattice parameter of 5.694 Å. Electronic band structure calculations carried out by Huang using DFT + Hubbard method revealed that bulk CaS has an indirect bandgap of 5.13 eV.[98] A value that is in agreement with the experimental bandgap value of 5.0 eV reported by Ghosh and Pandey.[88, 99] Moreover, Huang calculated a valence bandwidth of 3.25 eV that is mainly composed of the 3p orbitals of sulfur (from -3.3 eV to 0 eV) while the filled 3p levels of calcium are located at approximate -8 eV relative to the highest occupied level (0 eV) (Figure 2.15). The conduction band possesses a bandwidth of 3.69 eV and consists mainly of 3d and 4s orbitals of calcium, and the lowest unoccupied level is made up of principally the 3d levels of calcium (Figure 2.15).

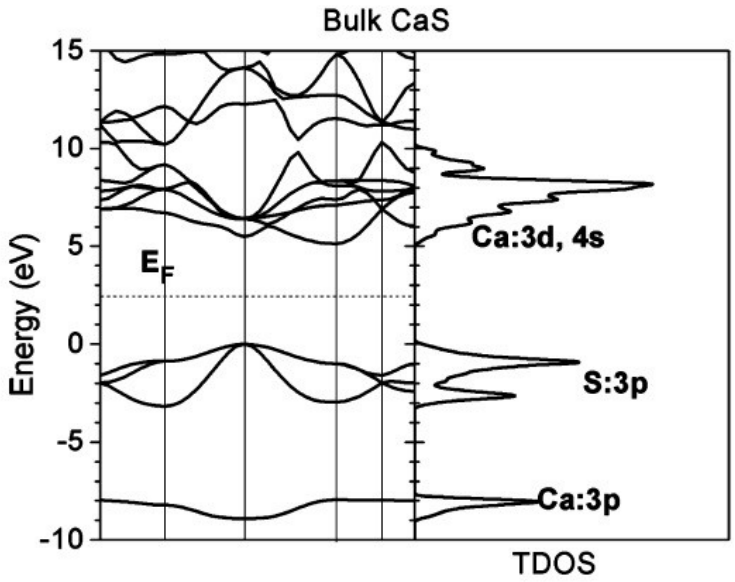

Figure 2.15 Band structure and total density of states (TDOS) of bulk CaS. Figure taken from "Native point defects in CaS: Focus on intrinsic defects and rare earth ion dopant levels for up-converted persistent luminescence" by Haung. Inorganic Chemistry, 2015, Ref [98].

The location of the ground and excited states energy of the divalent and trivalent ions relative to the valence and conduction bands in CaS is fundamental information to determine the energy required to activate the persistent luminescence as well for the elucidation of the mechanism behind this phenomenon. A method that accomplishes this objective was developed by Dorenbos.[84b] This method is based on the pattern exhibited by the ionization energies of an electron in the 4f orbitals in the lanthanide series with increasing *n*(number of electrons). Figure 2.16 shows the ionization energy pattern for the free gaseous divalent (red) and trivalent (blue) lanthanide ions. The ionization energies provide information on the binding energy of an electron to the atom. The pattern observed for the trivalent lanthanide ions is similar to the one of divalent ions, however, trivalent lanthanide ions exhibit larger ionization energies due to their higher ionic charge.

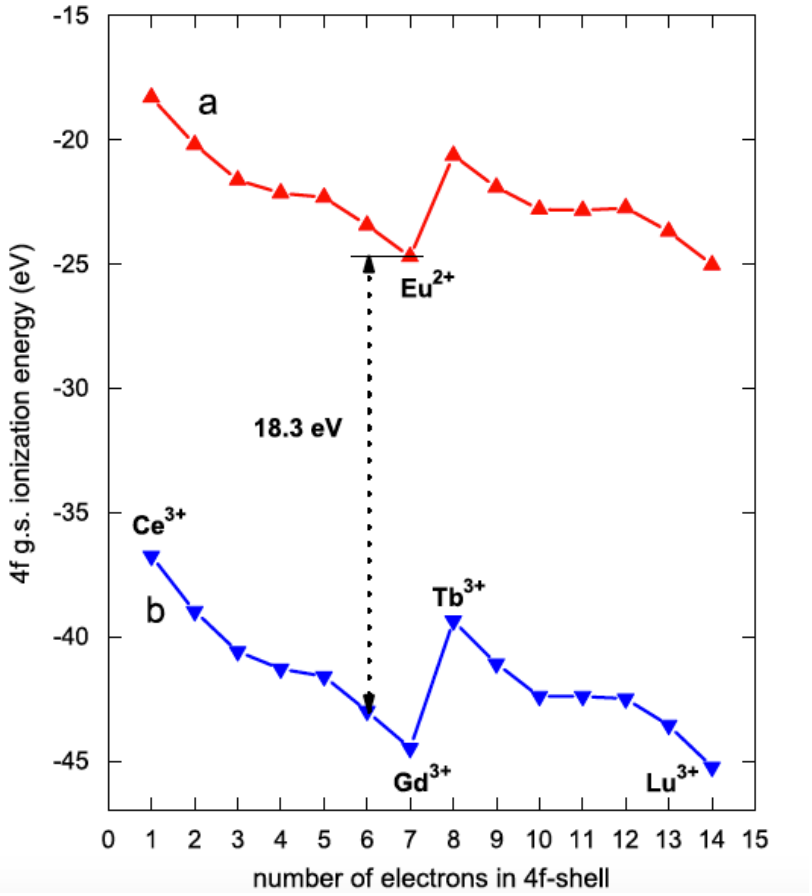

Figure 2.16 The ionization energies for (a) free gaseous divalent and (b) trivalent lanthanide ions as a function of the number of 4f electrons. Figure taken from "Lanthanide level location and related thermoluminescence" by Dorenbos *et al*. Radiation Measurements, 2008, Ref [100].

The behavior of the ionization energy of the ion as dopant in a host follows a similar pattern as the one for the free lanthanide ions. Ionization energies can be calculated from the charge transfer bands (valence band to trivalent lanthanide ion transitions) observed in the excitation spectra of lanthanide luminescence. Thus, the measurement of these values provides information on the location of the ground state energy relative to the top of the valence band of the corresponding divalent lanthanide ions.[101] This information is the starting point in the construction of a vacuum referred binding energy level scheme (VRBE), a scheme that summarizes the location of the lanthanide 4f and 5d levels within the bandgap of inorganic hosts. In Figure 2.17 the ground states of the divalent ions in CaS (red zigzag) are shown.

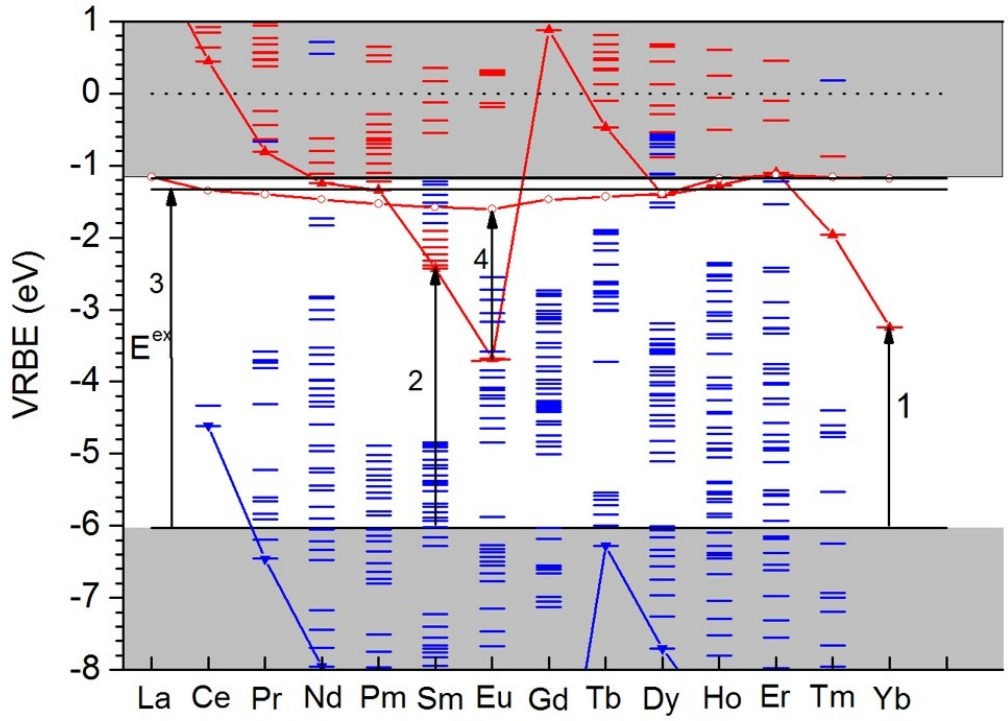

Figure 2.17 Vacuum referred binding energy level (VRBE) scheme showing the location of divalent (red) and trivalent lanthanide ions (blue) 4f and 5d energy levels in CaS.

The next important parameter to locate the energy levels of the lanthanides in the CaS host is the Coulomb repulsion energy U(6,A) for Eu. This parameter is defined as the energy difference between the ground state of Eu^{2+} and Eu^{3+}. In the case of using CaS as the host, the U(6,A) corresponds to 6.17 eV. This value was obtained from the compilation reported by Dorenbos.[85] It is important to highlight that the energy difference between the

ground state of Eu^{2+} and that of Eu^{3+} has reduced from a value of 18.3 eV for the free ions to a value of 6.17 eV. The ground state of the Eu^{2+} is brought closer to the ground state of Eu^{3+}. This decrease in the energy difference, known as redshift is attributed to the crystal field splitting and the charge distribution of the ion with its chemical environment. From the identification of the location of the ground state of Eu^{3+}, it is possible to predict the ground state of the other trivalent lanthanide ions. Figure 2.17 shows the ground states of the trivalent ions in CaS (blue). Moreover, knowing the ground state energies of divalent and trivalent ions, it is possible to obtain the $4f^n$ excited states. Furthermore, following the model developed by Dorenbos, it is predicted that the valence band is located at approximate -3.68 eV from the $4f^7$ ground state of Eu^{2+}.[85]

Experimental data collected for CaS doped with different Ln^{3+} was used to place the top of the valence band at -6.0 eV. An excitation band at 2.84 eV in the emission spectrum of Yb^{3+} reported by Parmentier *et al*., has been interpreted as the charge transfer band (see arrow 1 in Figure 2.17).[102] Yamashita *et al*., reported a broad excitation in CaS:Sm^{3+} at 3.55 eV assigned to the $4f^65d^1$ transition in Sm^{3+}. [103] However, that transition must be at much higher excitation and it is more likely to be due to the charge transfer to Sm^{3+}. The energy (see arrow 2 in Figure 2.17) is consistent with that predicted by the VRBE scheme. Furthermore, experimental data reported by Huang, Yokono *et al* and *Jia et al.,* was used to establish the bottom of the conduction band. In spectra reported by both groups the energy for host exciton creation E^{ex} (see arrow 3 in Figure 2.17) is estimated at 5 eV.[63a, 98, 104] By adding an estimated energy of 0.15 eV for the electron-hole binding energy, the bottom of the conduction band is placed near -0.9 eV. Moreover, arrow 4 in Figure 2.17 shows the energy for the $4f^7 \rightarrow 4f^65d^1$ transition of Eu^{2+}. It defines the location of the lowest $4f^{n-1}5d^1$ levels for all Ln^{2+} ions in CaS (connected red dots). The ground state of Eu^{2+} is in the bandgap, therefore the use of a high-energy irradiation such as 254 nm will cause the excitation of ground state electrons directly to the conduction band. This will be followed by trapping of electrons in the different available electron trapping sites.

2.6 Thermoluminescence

Thermoluminescence is defined as the emission of light exhibited by some semiconductor and insulator materials when they are heated and after being previously irradiated with a high energy excitation for a period of time.[105] This optical phenomenon is also known as thermal stimulated luminescence.

This phenomenon was first reported by Robert Boyle in 1663.[106] In his publication, he describes the luminescence exhibited by diamond while it was heated using a thick piece of hot iron and when he warmed it up using heat from his body. In 1676, Elsholtz and Oldeburg discovered that other minerals such as fluorspar (CaF_2) exhibited luminescence upon heating and postulated that heat was being directly converted into light.[107] It was not until 1735, while Du Fay was studying the luminescent properties of natural quartz, that he found that the light exhibited by the natural quartz when heated could be reactivated if the sample was exposed over a period of time to sunlight.[108] Thus, it was stablished that heat stimulated the emission of light from the material but it was not its cause.

The term 'thermoluminescence' was first used in the literature in 1895 by Wiedemann and Schimidt.[109] The authors reported the thermoluminescent properties of synthetically produced phosphors after irradiation with an electron beam. Following this work, the number of publications on thermoluminescence properties of natural and synthesized phosphors increased significantly and continues to do so, using different high energy irradiation such as α-rays, β-rays, γ-rays, X-rays, UV light and even visible light.

The persistent luminescent observed by some semiconductor and insulator materials is a form of thermal stimulated emission that occurs at room temperature. In this case, after the irradiation of the material, electrons retained in trapping sites located at $\leq$0.58 eV below the conduction band can be released using the thermal energy produced at room temperature. In general, the closer the position of the trapping sites to the edge of the conduction band, lower temperatures are required to favour the release of electrons from the traps to the conduction band. As the trapping sites move further away from the edge of

the conduction band, higher temperatures are required to release electrons contained within (Figure 2.18).

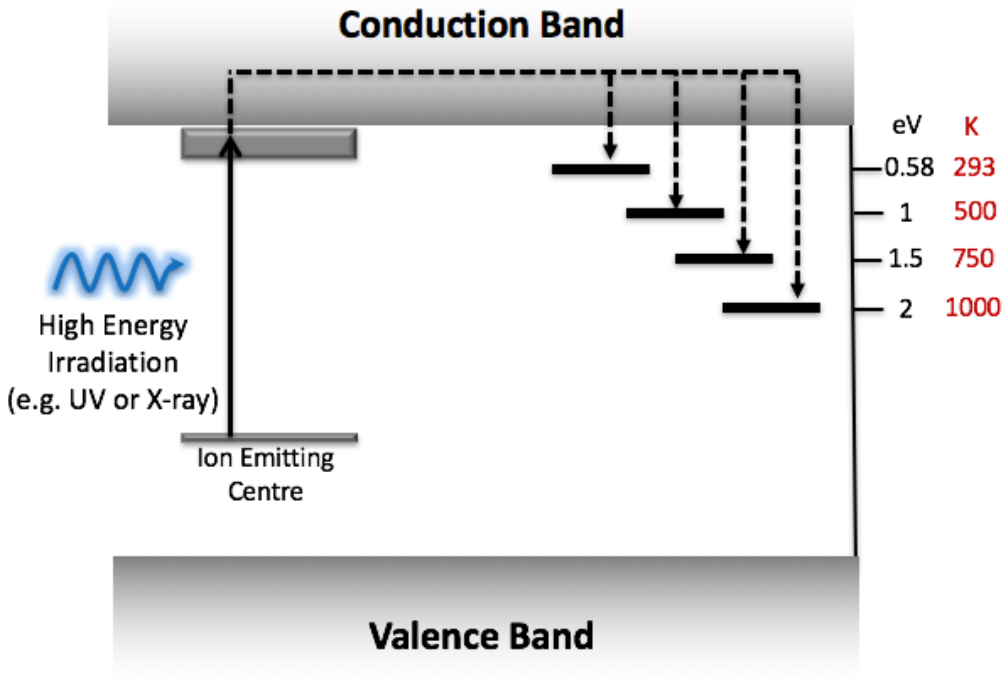

Figure 2.18 Scheme of a distribution of electron trapping sites in an insulator material and the temperature required to liberate electrons trapped in the different traps after irradiation.

Thermodynamically, the mean time (τ) an electron spends in a trap at a temperature T is given by equation 2.1,

$$\tau = s^{-1}e^{\left(\frac{E}{kT}\right)} \qquad (2.1)$$

where E is the trap depth or energy difference between the electron trapping site and the edge of the conduction band; k is Boltzmann's constant and s is the frequency factor, also referred as the 'attempt to escape' frequency and represents the times per second that a bound electron interacts with the lattice phonons (10^9-10^{14} s^{-1}). This exponential dependency of the temperature and τ was first reported by Jablonski in 1935.[110] Using equation 2.1 the mean time that an electron is trapped in a trap located at 0.58 eV below the

conduction band at T=298 K and s = 10^9 s^{-1}, is calculated to be 64 ms. The persistent luminescence observed at room temperature with an intensity (I) is dependent on the rate of release of electrons from the trap. This dependency is given by equation 2.2,

$$I(t) = -C\frac{dn}{dt} = C\ \frac{n}{\tau} \qquad (2.2)$$

where c is a proportionality constant and n is the number of electrons trapped in each trap located at E eV below the conduction band. If it is assumed that once the electron has been released from this specific trap, the probability of returning to the trap is negligible in comparison to the probability to recombine with a luminescent centre, then the intensity of the persistent luminescence decay at constant temperature following the end of the irradiation is given by equation 2.3,

$$I(t) = I_o e^{\left(-\frac{t}{\tau}\right)} \qquad (2.3)$$

where t is the time and I_o is the intensity at t=0. This equation describes a first order decay and it was first reported by Randall and Wilkins in 1945.[111] However, in reality most of the intensity as a function of time at a given temperature (T_o) cannot be fitted to a single exponential decay but to two or even more combined exponential decays. This can be explained by the overlap of electrons released from several traps at different E values that can be thermally stimulated at temperatures lower than T_o. However, it can also be attributed to the possibility that once an electron is being released from the trapping site, a retrapping process occurs due to the presence a nearby trapping site. Thus, a non-negligible probability of having a retrapping process over a recombination process. Randall and Wilkins also solved equation 2.3 for this latter case and the intensity of the persistent luminescence second order decay at constant temperature is given by equation 2.4,[111]

$$I(t) = \frac{I_o}{(n_o \alpha t + 1)^2} \qquad (2.4)$$

where n_o is the number of electrons trapped at t_o and α is a constant related to the mean lifetime and the relative probabilities of retrapping and recombination.

When equation 2.1 is used to determine the mean time lifetime of an electron trapped in a trap located at 1.5 eV below the conduction band at room temperature, a value of 7.4 x 10^9 years is obtained. Thus, luminescence from recombination process at room temperature after the release of an electron from this trap will never be observed in this lifetime. However, if T is increased, then τ decreases. Hence, by heating the material at a linear rate $\beta=dT/dt$, the release of electrons from deeper traps is favoured. Accordingly, the luminescence intensity exhibited upon heating will increase as the electrons are liberated from the trapping sites and decrease as the trap becomes depleted. Thus, the luminescence intensity $I(t)$ as a function of the temperature shows broad bands known as thermoluminescence glow peaks.[105, 112]

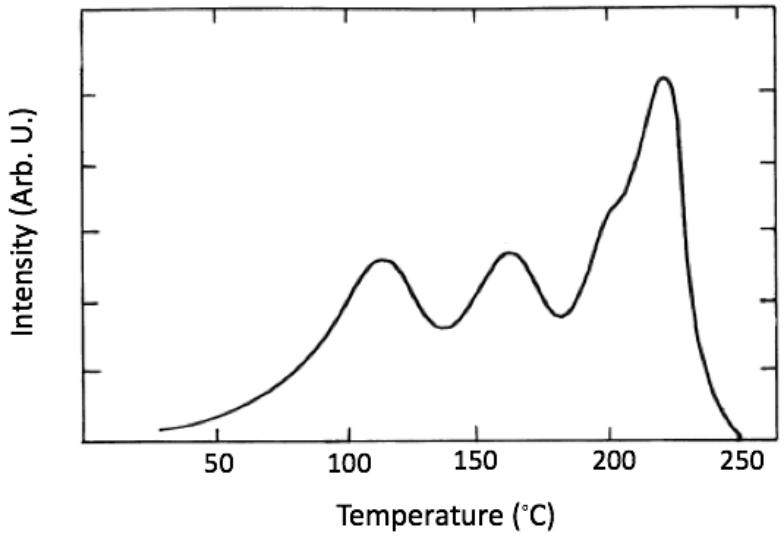

Figure 2.19 Example of a thermoluminescent glow curve. Figure adapted from reference [83].

An example of a thermoluminescence glow curves is shown in Figure 2.19. Each peak exhibited in the glow curve corresponds to an electron trapping site present in the host with a trap depth E and a frequency factor s. Thus, the nature of the thermoluminescent glow peaks gives information about the distribution of traps in the material. To estimate E and s for each glow curve peak, it is necessary to analyze each peak.

Following their work on the mathematical description of thermoluminescence, Randall-Wilkins found the mathematical expression that describes the shape of a thermoluminescent glow peak (Equation 2.5),

$$(T) = n_o s e^{\left[-\frac{E}{kT} - \int_0^T \frac{S}{\beta} e^{\left(-\frac{E}{kT}\right)} dT\right]} \qquad (2.5)$$

Based on equation 2.5, several computerized curve-fitting and deconvolution methods, of the multi-peak structure of the glow curves have been developed. Using *the initial rise method* and *the peak shape method* an estimate of E and s the characteristic parameters to describe the trapping sites may be obtained.

Garlick and Gibson proposed that for thermoluminescent emissions that follow first order decay that is thermal glow curves that exhibit a single peak or well defined separate peaks with a decay profile that can be fitted using a single exponential equation 2.6 may be applied.[113] This equation only considers the intensities and temperatures of the initial rise region of the glow peak where the temperature and intensity are significant lower than the temperature and intensity maxima ($T << T_m$ and $I << I_m$),

$$I(T) = e^{\left(-\frac{E}{kT}\right)} \qquad (2.6)$$

Thus, by plotting *ln(I)* versus$1/T$, a linear relationship is observed with a slope equal to $-E/k$. Once the value of E is determined, the frequency factor s can be estimated using Equation 2.7,

$$\frac{\beta E}{kT_m^2} = s e^{\left(-\frac{E}{kT_m}\right)} \qquad (2.7)$$

The peak shape method was developed by the contributions of Lushchik, Halperin, Braner and Chen.[105] As the name of this method implies, it is based on the shape of the peak, the half width parameters and the symmetry of the peak. It can be used for first and second decay orders, however it is not recommended when there is a significant overlap of the thermal glow peaks. In Figure 2.20 and Equations 2.8 to 2.11 the parameters defined from the shape of the thermal glow peak are given

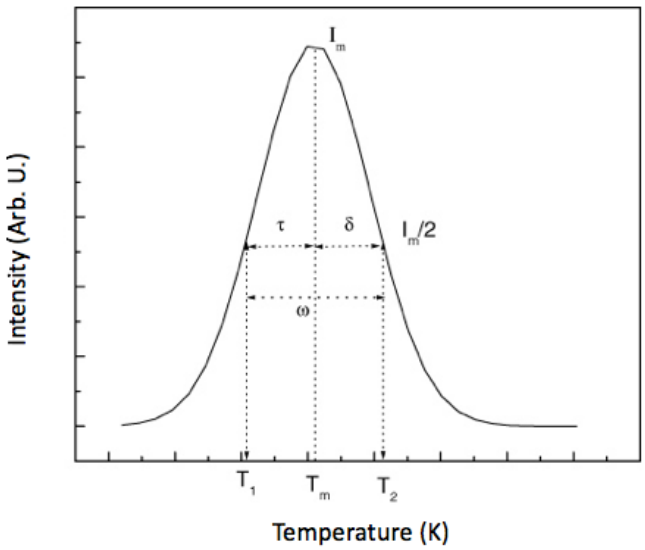

Figure 2.20 Diagram of the peak parameters used to determine the *E* and *s* parameters. Figure adapted from reference [114].

$$\delta = T_2 - T_m \qquad (2.8)$$

$$\tau = T_m - T_1 \qquad (2.9)$$

$$\omega = T_2 - T_1 \qquad (2.10)$$

$$\mu_g = \frac{\delta}{\omega} \qquad (2.11)$$

where μ_g is known as the geometry factor.

The trap depth is calculated using the Chen's equation (Equation 2.12) where η represents δ, τ and ω. The values C_η and b_η are defined by equations 2.14 to 2.19.

$$E_\eta = C_\eta \frac{kT_m^2}{\eta} - b_\eta(2kT_m) \qquad (2.12)$$

$$E = \frac{E_\delta + E_\tau + E_\omega}{3} \qquad (2.13)$$

$$C_\tau = 1.51 + 3(\mu_g - 0.42) \qquad (2.14)$$

$$C_\delta = 0.976 + 7.3(\mu_g - 0.42) \qquad (2.15)$$

$$C_\omega = 2.52 + 10.2(\mu_g - 0.42) \qquad (2.16)$$

$$b_\tau = 1.58 + 4.2\left(\mu_g - 0.42\right) \qquad (2.17)$$

$$b_\delta = 0 \qquad (2.18)$$

$$b_\omega = 1 \qquad (2.19)$$

Equation 2.7 and 2.20 are used to estimate the frequency factor *s* for a first and second order decay respectively,

$$\frac{\beta E}{kT_m^2} = se^{\left(-\frac{E}{kT_m}\right)}\left(1 + 2\frac{kT_m}{E}\right) \qquad (2.20)$$

These methods can be easily applied if the thermal glow peaks can be fitted to a Gaussian distribution and there is no significant overlap among the peaks, or if only one peak corresponding to one distribution of traps is found. However, most of the thermoluminescent glow curves do not exhibit these characteristics thus, the *peak position method* is the approach most used to estimate the trap depth *E* as a first approximation. It is based in the direct relationship between *E* and T_m found by Urbach and later on supported by Randall and Wilkins (Equation 2.22),[111]

$$E = kT_m \ln(s) \qquad (2.21)$$

if the product of $k\ln(s)$ is considered to be constant and the value to be $s=10^9\ s^{-1}$, then the trap depth is given by Urbach's equation (Equation 2.22) postulated in 1930 and widely used since then.

$$E = \frac{T_m}{500} \qquad (2.22)$$

Chapter 3 – Experimental Procedures and Methods

3.1 Synthetic Route for the Preparation of CaS:Eu^{2+}/Dy^{3+}

In order to synthesise CaS:Eu^{2+}/Dy^{3+} nanophosphors, three steps were necessary: *i)* synthesis of CaS nanoparticles *via* co-precipitation, *ii)* incorporation of Eu^{3+} as a dopant and its reduction to Eu^{2+} and *iii)* the incorporation of Dy^{3+} as the co-dopant to furnish the 'trapping' states.

3.1.1 Synthesis of CaS Nanoparticles *via* Co-precipitation Method

The co-precipitation method was chosen as the synthetic method to obtain CaS nanoparticles. $CaCl_2$ was selected as the calcium source while two sulfide salts, Na_2S and K_2S, were evaluated as sulfide precursors.

3.1.1.1 Using Na_2S as the Sulfide Precursor

Ethanolic solutions of the calcium and sulfide precursors were prepared by dissolving 0.62 mmol (0.0918 g) of $CaCl_2 \cdot 2H_2O$ in 50 mL of ethanol (99%) and 0.62 mmol (0.1500 g) of $Na_2S \cdot 9H_2O$ in 50 mL of ethanol (99%). The sulfide solution is sonicated for 30 min, while the calcium solution is placed in a three-neck flask at room temperature under vigorous stirring and a flow of argon to avoid the formation of calcium carbonate. The $Na_2S \cdot 9H_2O$ solution is injected to the $CaCl_2 \cdot 2H_2O$ solution at a rate of 20 mL min^{-1} at room temperature under a flow of argon and vigorous stirring for 3 h.

CaS nanoparticles were precipitated under reduced pressure followed by a dropwise addition of 20 mL of tetrahydrofuran and stirred vigorously for 2 h under a flow of argon. The nanoparticles were recovered by centrifugation, washed three times with ethanol (99%) and dried under vacuum overnight. Finally, CaS nanoparticles were annealed for 4h at 700°C under a N_2 atmosphere.

3.1.1.2 Using K_2S as the Sulfide Precursor

K_2S was used as a second alternative as the sulfide source in the synthesis of CaS nanoparticles. In this case, an ethanolic solution of K_2S was prepared by dissolving 0.62 mmol (0.0690 g) in 50 mL of ethanol (99%). This solution was injected to the $CaCl_2 \cdot 2H_2O$ ethanolic solution (0.62 mmol, 50 mL) using the same conditions as described in the section 3.1.1.1. The obtained CaS nanoparticles were precipitated, washed and annealed in the same manner as previously described.

3.1.2 Synthesis of $CaS:Eu^{3+}$

In order to synthesize $CaS:Eu^{3+}$ nanoparticles, the same approach as described in section 3.1.1.1 was followed; $Eu(NO_3)_3 \cdot 5H_2O$ was introduced as the source of Eu^{3+} to substitute for Ca^{2+} in the concentration ranging from 0.01 mol% to 1 mol%. Thus, a stock solution of $Eu(NO_3)_3 \cdot 5H_2O$ (0.5 mg/mL) in 20 mL ethanol (99%) was prepared and aliquots of the stock solution were mixed with the $CaCl_2 \cdot 2H_2O$ ethanolic solution. Table 3.1 summarizes the quantities of $CaCl_2 \cdot 2H_2O$ and $Na_2S \cdot 9H_2O$ used as well as the volume of the $Eu(NO_3)_3 \cdot 5H_2O$ stock solution used for all the synthesis to give the desired Eu^{3+} concentration for each sample prepared.

3.1.3 Reduction of Eu^{3+} to Eu^{2+}

A 4-hour annealing treatment was required to improve the crystallinity of the obtained CaS nanoparticles *via* the co-precipitation method. This heat treatment was also used for the reduction of Eu^{3+} to Eu^{2+}. $CaS:Eu^{3+}$ nanoparticles were annealed in the presence of sulfur powder using a ratio of 1:4 (CaS: sulfur powder by weight) under a N_2 atmosphere. A study was carried out to determine the annealing temperature at which the complete reduction of Eu^{3+} to Eu^{2+} was obtained. Table 3.2 summarizes the experimental parameters studied.

Table 3.1. Amount of salt precursors used for the preparation of CaS:Eu^{3+} nanoparticles varying the Eu^{3+} dopant concentration from 0.01 mol% to 1 mol%

	AMOUNT USED		
Eu^{3+} (mol%)	**$CaCl_2 \cdot 2H_2O$ (g)**	**$Na_2S \cdot 9H_2O$ (g)**	**$Eu(NO_3)_3 \cdot 5H_2O$ [a] (mL)**
0.01	0.0918	0.1500	0.10
0.02	0.0918	0.1500	0.21
0.05	0.0918	0.1500	0.53
0.07	0.0918	0.1500	0.75
0.1	0.0917	0.1499	1.07
0.5	0.0914	0.1493	5.35
0.7	0.0912	0.190	7.50
1	0.0909	0.1486	10.7

[a] Corresponds to the aliquot volume taken from the $Eu(NO_3)_3 \cdot 5H_2O$ stock solution and mixed with the $CaCl_2$ ethanolic solution prior to injection.

Table 3.2. Annealing temperatures studies for the reduction of Eu^{3+} to Eu^{2+} in CaS

Eu^{3+} (mol%)	**Annealing Time (h)**	**Annealing Temperature (°C)**
0.01	4	600
		700
		800
		900
1	4	600
		700
		800
		900

3.1.4 Synthesis of CaS:Eu^{2+}/Dy^{3+} Nanophosphors

Dy^{3+} was introduced as a co-dopant to induce the formation of trapping sites in CaS by the substitution of Ca^{2+} by Dy^{3+}. A stock solution of $Dy(NO_3)_3{\cdot}H_2O$ (0.25 mg/mL) in 20 mL ethanol (99%) was prepared and an appropriate aliquot was mixed with $Eu(NO_3)_3{\cdot}5H_2O$ and $CaCl_2{\cdot}2H_2O$ in a three-neck flask under vigorous stirring and a flow of argon. The concentration of Dy^{3+} was varied from 0.001 mol% to 1 mol%, while maintaining constant the concentration of Eu^{3+} (0.02 mol%). Next, the $Na_2S{\cdot}9H_2O$ solution was injected to the mixture of $Eu(NO_3)_3{\cdot}5H_2O$, $Dy(NO_3)_3{\cdot}H_2O$ and $CaCl_2{\cdot}2H_2O$ solution at a rate of 20 mL min^{-1} at room temperature under the flow of argon and vigorously stirred for 16 h. The synthesised CaS:Eu^{3+}/Dy^{3+} nanoparticles were precipitated and washed in the same manner as described is section 3.1.1.1 followed by annealing with sulfur powder for 4h at 700°C under N_2 atmosphere. Table 3.3 summarizes the experimental quantities of $CaCl_2{\cdot}2H_2O$ and $Na_2S{\cdot}9H_2O$ used as well the volume of the $Eu(NO_3)_3{\cdot}5H_2O$ and $Dy(NO_3)_3{\cdot}H_2O$ stocks solutions used for all the synthesis.

Table 3.3 Amount of salt precursors used for the preparation of CaS:Eu^{2+}/Dy^{3+} nanoparticles varying the Dy^{3+} dopant concentration from 0.001 mol% to 1 mol%

	AMOUNT USED			
Dy^{3+} (mol%)	**$CaCl_2{\cdot}2H_2O$ (g)**	**$Na_2S{\cdot}9H_2O$ (g)**	**$Eu(NO_3)_3{\cdot}5H_2O$ [a] (mL)**	**$Dy(NO_3)_3{\cdot}H_2O$ [b] (mL)**
0.001	0.0918	0.1500	0.21	0.017
0.002	0.0918	0.1500	0.21	0.035
0.005	0.0918	0.1500	0.21	0.087
0.01	0.0918	0.1500	0.21	0.174
0.05	0.0918	0.0918	0.21	0.871
0.1	0.0917	0.1498	0.21	1.75
0.5	0.0914	0.1493	0.21	8.70
0.7	0.0912	0.1490	0.21	12.20
1	0.0910	0.1485	0.21	17.40

[a,b] Corresponds to the aliquots volume taken from the $Eu(NO_3)_3{\cdot}5H_2O$ and $Dy(NO_3)_3{\cdot}5H_2O$ stock solutions and mixed with the $CaCl_2$ ethanolic solution prior to injection.

3.1.5 Synthesis of CaS: Dy^{3+}

In order to have a better understanding of the optical properties of Dy^{3+} ions as a dopant in the nano-sized sulfide based host, CaS:Dy^{3+} nanoparticles were synthesized. Na_2S and K_2S were evaluated as the sulfide source.

3.1.5.1 Using Na_2S as the Sulfide Precursor

CaS:Dy^{3+} nanoparticles were synthesized using the same precursors and conditions described in section 3.1.4. The concentration of Dy^{3+} was varied from 0.001 mol% to 1 mol%. Table 3.4 summarizes the experimental quantities of $CaCl_2 \cdot 2H_2O$, $Na_2S \cdot 9H_2O$ and the volume of $Dy(NO_3)_3 \cdot H_2O$ used from the prepared stock solution.

Table 3.4 Amount of salt precursors used for the preparation of CaS: Dy^{3+} nanoparticles varying the Dy^{3+} dopant concentration from 0.001 mol% to 0.01 mol%

	AMOUNT USED		
Dy^{3+} (mol%)	**$CaCl_2 \cdot 2H_2O$ (g)**	**$Na_2S \cdot 9H_2O$ (g)**	**$Dy(NO_3)_3 \cdot H_2O$ [a] (mL)**
0.001	0.0918	0.1501	0.017
0.002	0.0918	0.1501	0.035
0.005	0.0918	0.1501	0.087
0.01	0.0918	0.1500	0.174

[a] Corresponds to the aliquot volume taken from the $Dy(NO_3)_3 \cdot 5H_2O$ stock solutions and mixed with the $CaCl_2$ ethanolic solution prior to injection.

3.1.5.2 Using K_2S as the Sulfide Precursor

CaS:Dy^{3+} nanoparticles were synthesized using $CaCl_2 \cdot 2H_2O$, $Dy(NO_3)_3 \cdot H_2O$ and K_2S as the sulfide source. CaS:Dy^{3+} nanoparticles were synthesised *via* the injection of K_2S to a mixture of $CaCl_2 \cdot 2H_2O$ and $Dy(NO_3)_3 \cdot H_2O$ at a rate of 20 mL min^{-1} at room temperature under a flow of argon and under vigorous stirring for 16 h. CaS:Dy^{3+} nanoparticles were precipitated, washed and annealed following the same conditions described in section 3.1.4. The concentration of Dy^{3+} was varied from 0.001 mol% to 1 mol%. Table 3.5 summarizes the experimental quantities of $CaCl_2 \cdot 2H_2O$, K_2S and $Dy(NO_3)_3 \cdot H_2O$ used in all the synthesis.

Table 3.5 Amount of salt precursors used for the preparation of CaS: Dy^{3+} nanoparticles varying the Dy^{3+} dopant concentration from 0.001 mol% to 0.01 mol%

	AMOUNT USED		
Dy^{3+} (mol%)	**$CaCl_2 \cdot 2H_2O$ (g)**	**K_2S (g)**	**$Dy(NO_3)_3 \cdot H_2O$ [a] (mL)**
0.001	0.0918	0.0689	0.017
0.002	0.0918	0.0689	0.035
0.005	0.0918	0.0689	0.087
0.01	0.0918	0.0689	0.174

[a] Corresponds to the aliquot volume taken from the $Dy(NO_3)_3 \cdot 5H_2O$ stock solutions and mixed with the $CaCl_2$ ethanolic solution prior to injection.

3.2 Rendering CaS:Eu^{2+}/Dy^{3+} Nanophosphors Water Dispersible

The as-synthesized CaS:Eu^{2+}/Dy^{3+} exhibit a high degree of agglomeration as consequence of the annealing treatment. Thus, a method was developed to disrupt the CaS:Eu^{2+}/Dy^{3+} agglomerates before any surface modification were carried out.

3.2.1 Disruption of the Agglomeration

25 mg of the CaS:Eu^{2+}/Dy^{3+} as-synthesized nanophosphors were ground for 15 min with a mortar and pestle using 20 μL of ethanol (99%). The final product was dispersed in 2 mL of ethanol (99%) and sonicated for 30 min. The colloidal suspension was centrifuged at 5000 rpm for 10 min. The supernatant was stored and the pellet was re-dispersed in ethanol and the sonication and centrifugation process were repeated twice.

The supernatants were collected and ultrasonicated using a titanium tip sonicator probe (30 KHz). A time optimization study was carried out to determine the ideal conditions that would produce minimum agglomeration and a particle size distribution within the limits for biological applications. The times of immersion of the sonication probe in the supernatant studied were 1, 2, 3, 4 and 5 min.

3.2.2 Surface Modification Strategies

Two "type_add" surface modification strategies were evaluated to provide water dispersible properties to the CaS:Eu^{2+}/Dy^{3+} nanophosphor: *i)* conjugation of thiol ligands, *ii)* adsorption of polyvinylpyrrolidone (PVP-10) as a polymeric shell and grafting of a silica shell.

3.2.2.1 Conjugation of a Thiol Ligand

In order to render the CaS:Eu^{2+}/Dy^{3+} nanophosphors water dispersible, the presence of the sulfide dangling bonds on the surface of the CaS:Eu^{2+}/Dy^{3+} nanophosphor were exploited. The post-synthesis conjugation of the thiol molecules, 16-mercaptohexadecanoic acid, to the surface of the nanoparticles was carried out.

The following procedure was used to functionalize the thiol molecules to the surface of the nanoparticles. Following ultrasonication, the nanophosphors were centrifuged at 10000 rpm for 10 min. 5 mg of the wet pellet was mixed with 2 mL of a 5 mg/mL solution of the thiol ligand dispersed in methanol. The mixture was stirred at room temperature at 700 rpm for 5 days. The nanophosphors were centrifuged and washed several times with methanol to remove the remaining non-conjugated thiol ligand.

3.2.2.2 Adsorption of PVP-10

The adsorption of the polyvinylpyrrolidone ($M_w \approx 10000$) an amphiphilic polymer on the surface of CaS:Eu^{2+}/Dy^{3+} nanophosphors was evaluated as a post-synthetic method to produce dispersible nanoparticles in polar solvents without affecting the optical properties of the nanoparticles.

Following ultrasonication, the CaS:Eu^{2+}/Dy^{3+} nanophosphors were centrifuged at 10000 rpm for 10 min. 10 mg of the wet pellet was dispersed in 2 mL of ethanol (99%) and 110 mg of PVP-10 was dissolved in 3.5 mL of ethanol. Both solutions were sonicated for 30 minutes and were mixed and stirred for 24 hours at room temperature. The PVP-CaS:Eu^{2+}/Dy^{3+} nanophosphors were centrifuged and washed with a water:acetone mixture (1:10 w/w) three times to remove the non-adsorbed PVP-10 polymer.

3.2.2.3 Grafting of a Silica Shell

The grafting of a silica shell on the surface of CaS:Eu^{2+}/Dy^{3+} nanophosphors was evaluated as post-synthetic process to provide water dispersibility and to improve the isolation of the nano host from the surrounding aqueous media to prevent the hydrolysis of CaS.

Two procedures were carried out to graft the silica shell on the surface of the CaS:Eu^{2+}/Dy^{3+} nanophosphors: 5 mg of PVP-CaS:Eu^{2+}/Dy^{3+} nanophosphors were dispersed in 5 mL of ethanol (99%) and sonicated for 10 minutes to ensure a colloidal dispersion in the polar solvent. Following the sonication, PVP-CaS:Eu^{2+}/Dy^{3+} nanophosphors were mixed with 50 μL of concentrated ammonium hydroxide at a rate of 5μL/min under constant stirring of 700 rpm. The mixture was left under stirring at 700 rpm for 15 min prior the introduction of tetraethyl orthosilicate (TEOS) in the mixture. Furthermore, 5 μL of TEOS was introduced to the mixture by addition of 1.25 μL every 10 minutes and under stirring at 700 rpm. Finally, the mixture was stirred at 700 rpm for 24 hours at room temperature. The nanophosphors were isolated *via* precipitation with acetone followed by centrifugation. The isolated TEOS-PVP-CaS:Eu^{2+}/Dy^{3+} nanophosphors were subsequently washed three times with a water: ethanol mixture (1:10 w/w).

The second approach to graft a silica shell on the surface of the CaS:Eu^{2+}/Dy^{3+} nanophosphors was carried out in collaboration with Dr. Cyrille Richards at the Institut de Chemie of the French National Centre for Scientific Research. 2 mg of CaS:Eu^{2+}/Dy^{3+} nanophosphors were dispersed in 2 mL of ethanol (99%) and sonicated for 5 minutes. Followed, 222 μL of ethanol, 247 of water and 6.7 μL of TEOS were added in the dispersion and the mixture was sonicated for 5 minutes to activate the hydrolysis process of the TEOS. The, 25 μL of aqueous solution of NH_4OH were and the reaction is left for 4 days at room temperature in a rotator. The TEOS-CaS:Eu^{2+}/Dy^{3+} nanophosphors were precipitated *via* centrifugation and washed several times with a mixture of water: ethanol. The TEOS-CaS:Eu^{2+}/Dy^{3+} nanophosphors were stored in ethanol until use.

3.3 Characterization and Experimental Techniques and Methods

3.3.1 X-Ray Powder Diffraction

The X-Ray powder diffraction patterns were collected at room temperature with the Kα (45 kV and 40 mA) radiation of Cu using a Scintag XDS-2000 diffractometer equipped with a Si(Li) Peltier-cooled solid state detector. The 2θ scan range was set from 20-90° with a scanning step size of 0.02° and a counting time of 0.5 s per step. All samples were measured using a quartz zero background insert disk as the sample holder.

3.3.2 Inductively Coupled Plasma – Mass Spectroscopy (ICP-MS) Analysis

ICP-MS measurements were performed to determine the concentrations of Eu and Dy in the CaS:Eu^{2+}/Dy^{3+} nanophosphor using an Agilent 7500 instrument. Argon was used as the carrier gas. The nanophosphors were dissolved in a 5% HNO_3 solution. A calibration curve of 5 points was established using a SPEX lanthanide multi element standard solution (10 mg/mL).

3.3.3 Optical Characterization of the Persistent Luminescent Nanophosphors

The excitation spectra of CaS nanoparticles and CaS:Eu^{2+} and CaS:Eu^{2+}/Dy^{3+} were recorded on a Varian Cary Eclipse Fluorescence spectrophotometer at room temperature exciting the sample with a xenon flash lamp.

The emission spectra were collected over the 350 – 700 nm range using an UV lamp emitting at 254 nm as the excitation source with a power of 6W. The measurements were performed on powder samples placed in quartz capillary tubes. The emissions were collected from the samples at $\pi/2$ with respect to the incident beam and then dispersed by a 1 m Jarrell-Ash Czerny-Turner double monochromator with an optical resolution of approximate 0.15 nm. A thermoelectrically cooled Hamamatsu R943-02 photomultiplier tube was used to detect the emissions. The photomultiplier signals were processed by a preamplifier and transferred to a gated photon-counter model SR400 Standard Research System data acquisition system. The emission spectra were recorded using the Standard Research Systems SR465 software.

Persistent luminescence decay profiles were measured at room temperature on weight normalized powdered samples in a 1 cm-diameter sample holder. The samples were previously illuminated with an UV lamp (254 nm, 6W). The emission was detected *via* an optical fiber using a Scientific Pixis 100 CCD camera cooled at -65°C coupled with an Acton SpectraPro 2150i spectrometer for spectral analysis.

3.3.4 Thermal-Stimulated Luminescence

Thermal-stimulated luminescence measurements were performed with a home assembled measurement set-up. The sample prepared as a thin pressed pellet and silver glued on the cold finger of a cryostat (10K) and excited across the cryostat quartz window with an UV lamp (254 nm, 6W). Thermal-stimulated luminescence was detected *via* an optical fiber using a Scientific Pixis 100 CCD camera cooled at -65°C coupled with an Acton SpectraPro 2150i spectrometer for spectral analysis. The samples were heated at a rate of 10 K min^{-1}.

3.3.5 NIR Photostimulated Luminescence

Samples of CaS nanoparticles, CaS:Eu^{2+} and CaS:Eu^{2+}/Dy^{3+} were excited using UV irradiation (254 nm) for 10 min and the samples were subsequently placed in the dark until the persistent luminescence subsided. The samples were then excited using a 980 nm laser diode, with a maximum power density of 4000 mW/cm^2. The decrease in intensity of the NIR photostimulated luminescence was recorded as a function of time. The measurements were performed on powder samples placed in quartz capillary tubes. The visible emissions (486 nm and 650 nm) were collected from the samples at $\pi/2$ with respect to the incident beam and then dispersed by a 1 m Jarrell-Ash Czerny-Turner double monochromator. A thermoelectrically cooled Hamamatsu R943-02 photomultiplier tube was used to detect the visible emissions. The photomultiplier signals were processed by a preamplifier and transferred to a gated photon-counter model SR400 Stanford Research System data acquisition system. The excitation power density was varied by using neutral density filters of different optical densities. The excitation spectrum of CaS:Eu^{2+}/Dy^{3+} nanophosphors (λ_{ems} = 650 nm) was measured using a Ti-Saphire laser (model 3900S from Spectra

Physiscs, 850-1000 nm wavelength). The spectrum was recorded using the same experimental set up described above.

3.3.6 Transmission Electron Microscopy (TEM)

TEM was used to characterize the nanophosphors. TEM analysis of the colloidal dispersion of nanophosphors was performed using a Philips CM200 microscope operating at 200 kV equipped with a charge-coupled device (CCD) camera (Gatan). Prior to analysis, a 1 mg sample was dispersed in 1 mL of ethanol A drop of the resulting solution was evaporated on a formvar/carbon film supported on a 300 mesh copper grid (3 mm in diameter).

3.3.7 Fourier Transform Infrared Spectroscopy (FT-IR)

FT-IR spectra were measured on a Nicolet iS5 FT-IR spectrometer. All solids were dried under vacuum for 24 hours prior to analysis. The spectra in transmission mode were recorded using a wavenumber range of 4000 – 550 cm^{-1} with a 4 cm^{-1} resolution and a scan count of 64.

3.3.8 Persistent Luminescence Imaging

1 mg/mL of Thiol-CaS:Eu^{2+}/Dy^{3+}, PVP-CaS:Eu^{2+}/Dy^{3+} and TEOS-CaS:Eu^{2+}/Dy^{3+} nanophosphors were dispersed in ethanol and in water. The suspensions were excited for 5 min with a UV lamp (254 nm, 6W). The suspensions were placed in imaging wells and image of the persistent luminescence exhibited were acquired up to 30 minutes. Signal acquisition was carried out using a photon-counting system based on a cooled GaAs intensified charge-coupled (ICD) camera (Photon-Imager; Biospace, Paris, France) without external excitation source. Acquired images processing and ROI drawing were achieved using Biospace developed software, PhotoVision+.

3.3.9 *In vivo* systemic injections

0.3 mg of TEOS-CaS:Eu^{2+}/Dy^{3+} were dispersed in ethanol (99%) and centrifuged. The supernatant was removed and replaced by 300 μL of 5% sterile glucose solution. The

suspension was excited *ex vivo* for 5 min with a UV lamp (254 nm, 6W). Five-week-old female BALB/c mouse was anaesthetized by intraperitoneal injection of a mixture of ketamine (85.5 mg kg^{-1}, Centravet) and xylazine (3.1 mg $Kg^{-1,}$ Bayer) diluted in 150 mM NaCl. 200 µL of the prior charged suspension were intravenously injected into the animal. Immediately after the injection, the animal was placed on its back under the photon-counting device, and the acquisition was performed during 30 minutes. Signal acquisition was carried out using a photon-counting system based on a cooled GaAs intensified charge-coupled (ICD) camera (Photon-Imager; Biospace, Paris, France) without external excitation source. Acquired images processing and ROI drawing were achieved using Biospace developed software, PhotoVision+. Experiments were conducted following the NIH recommendations and in agreement with a regional ethic committee for animal experimentation.

Chapter 4 – Development of CaS:Eu^{2+}/Dy^{3+} Persistent and NIR Photo-Stimulated Nanophosphors

4.1 Development of CaS:Eu^{2+}/Dy^{3+}Nanophosphors

4.1.1 Choosing the synthetic route

The low number of hosts that can offer red persistent luminescence suitable for biological applications such as fluorescence optical imaging, has re-kindled the attraction for sulfides hosts, such as CaS. Research on persistent luminescent materials has been oriented in the search of synthetic procedures that will produce CaS with nanoscale dimensions. Solid state reaction and the flux method followed by a grinding process have been proposed however, crystals with average particle size in the micrometer range and high polydispersity are obtained. Wet chemical processes such as sol-gel and solvothermal could be used for the synthesis of oxysulfide hosts such as Y_2O_2S, however, the aqueous conditions used in these methods do not favour the precipitation of calcium sulfide since it is easily hydrolyzed in water. Co-precipitation method is another type of wet chemical process used to synthesize nanoparticles. It is based on the use of saturated solutions that induce nucleation followed by the growth of nanocrystals.[115] Although, most of the co-precipitation procedures make use of water as the solvent, Sun *et al*., reported for the first time a co-precipitation method to obtain nano-sized CaS crystals using ethanol (99%) as the solvent, minimizing the hydrolysis of the alkaline earth sulphide.[116] Thus, this method was selected as the synthetic procedure for the development of the CaS:Eu^{2+}/Dy^{3+} nanophosphor.

The first step in the synthesis requires the injection of a sulphide precursor into a saturated solution of $CaCl_2$. Nucleation occurs rapidly after the injection and continues until the precursors concentration drops below a critical threshold. This is followed by a particle growth stage *via* Ostwald ripening that favors the formation of CaS nanoparticles. Subsequently, CaS nanoparticles are precipitated under reduced pressure followed by a

dropwise injection of tetrahydrofuran. The nanoparticles are recovered by centrifugation and dried under vacuum.

4.1.2 Synthesis and characterization of CaS nano host

The first step in the development of the CaS:Eu^{2+}/Dy^{3+} nanophosphors was to optimize the conditions for the synthesis of CaS nanoparticles using the co-precipitation method described in section 4.1.1. In Table 4.1 the parameters used for the synthesis of the undoped CaS nano host are shown. These parameters were established based on the work of Sun *et al,* and other reported synthetic procedures of alkaline earth sulfide nano sized hosts.[116-117]

Table 4.1 Synthetic parameters used in the synthesis of CaS nanoparticles

Synthetic Parameter	
Solvent	Ethanol 99%
Precursors	$Na_2S{\cdot}9H_2O$ (0.62 mmol) $CaCl_2{\cdot}2H_2O$ (0.62 mmol)
Sulfide injection rate	20 mL/min
Reaction time	3 h
Temperature	Room temperature

After completion of the synthetic procedure, the white powder product was dried under vacuum and characterized by X-Ray powder diffraction (XRPD), a technique that provides information on the crystal phase of the nano host. In Figure 4.1B the XRPD experimental pattern of the as synthesized CaS nano host is shown. The presence of the principal diffraction peaks for the cubic phase (2 0 0) and (2 2 0) as well other diffraction peaks that are in agreement with reported pattern for CaS (JCPDS File No. 750893, Figure 4.1A) confirm the presence of cubic CaS crystallizing with space group $Fm\bar{3}m$.

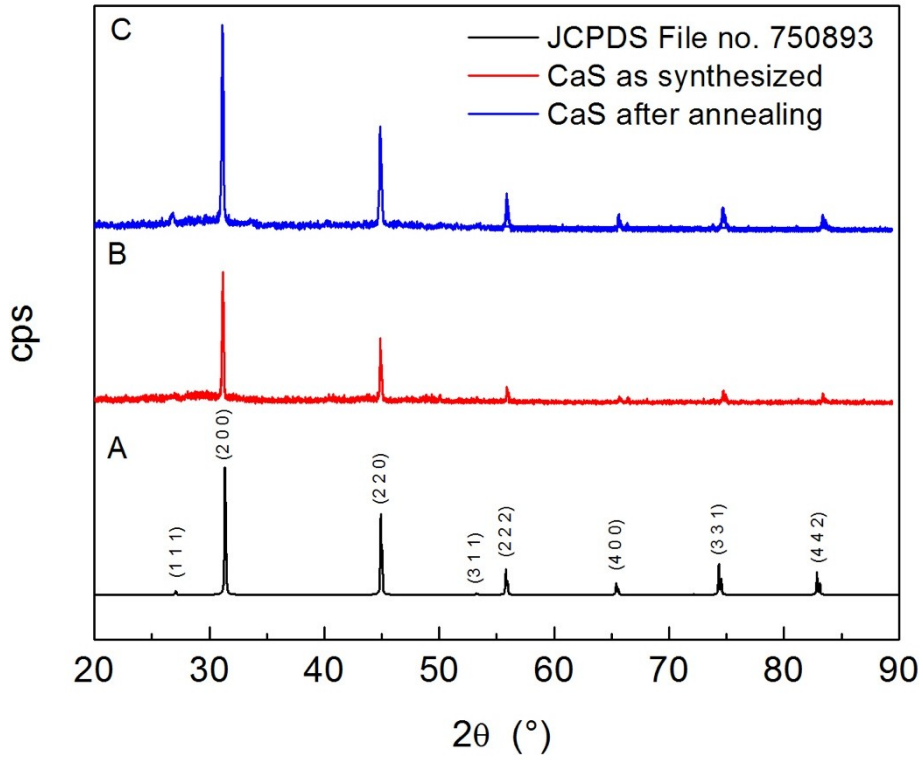

Figure 4.1 XRPD Patterns of (A) Reference Pattern JCPDS File No. 750893, (B) CaS nanoparticles as synthesized and (C) CaS nanoparticles after annealing treatment.

Crystallographic information such as the inter-planar spacing *(d-spacing)* and the lattice constant (a) of the CaS nanoparticles can be calculated using the XRPD experimental pattern. *d*-spacing is defined as the perpendicular distance between adjacent lattice planes and it can be calculated using equation 4.1,

$$d = \frac{\lambda}{2sin\theta} \qquad (4.1)$$

where λ is the wavelength of CuKα (1.543 Å) and θ is the angle of the most intense diffraction peak which corresponds to the (l =2, m =0, n =0) reflection. The lattice constant (a) refers to the physical dimension of the unit cell. CaS shows a cubic crystal phase therefore, all dimensions of the unit cell are equal (a=b=c). The lattice parameter is represented by (a), and it is calculated using equation 4.2.

$$a = d\sqrt{l^2 + m^2 + n^2} \qquad (4.2)$$

Table 4.2 summarizes the values obtained for the as synthesized CaS nanoparticles. The experimental value for the lattice parameter agrees with the reported lattice constant of 5.694 Å (JCPDS File no. 750893).

Table 4.2 Experimental *d-spacing* and lattice parameter *(a)* of CaS nanoparticles

Nanoparticle Type	d (Å) ± (Å)	a (Å) ± (Å)
CaS	2.85 ± 0.02	5.70 ± 0.03
Annealed CaS	2.84 ± 0.02	5.69 ± 0.03

In order to improve the crystallinity of the CaS nanoparticles, the sample was annealed at 700°C, for 4 hours under a flow of N_2 as reported by Vinay *et al.*[118] The XRPD pattern for CaS nanoparticles following the thermal procedure is shown in Figure 4.1C. The XRPD experimental pattern reveals higher counts per second for the diffraction peaks for the (2 0 0) and (2 2 0) planes as well for the (1 1 1), (2 2 2), (4 0 0), (3 3 1) and (4 4 2) planes, confirming the enhancement of the crystallinity of the nanoparticles. Using equations 4.1 and 4.2, *d-spacing* and a parameters were calculated for the annealed CaS nanoparticles and the results are shown in Table 4.2. As it can be seen, the calculated values of d and a do not change after annealing, suggesting that no changes in the crystal phase have occurred.

The size of the crystallite (D_{lmn}) can be calculated from the experimental XRPD pattern, using the Scherrer equation (Equation 4.3).

$$D_{lmn} = \frac{K\lambda}{B_{lmn}cos\theta} \qquad (4.3)$$

where D_{lmn} is the crystallite size in the direction perpendicular to the lattice planes, (l, m, n) are the Miller indices of the main diffraction peak, K is the crystallite-shape factor (K = 0.9, best approximation in the absence of shape information) and B_{lmn} is the full width at

half maximum of the main diffraction peak.[119] Thus, from the line broadening of the (2 0 0) diffraction peak of the annealed CaS nanoparticles (Figure 4.1C) a crystallite size ($D_{2\,0\,0}$) of 76 nm ± 10 nm was calculated.

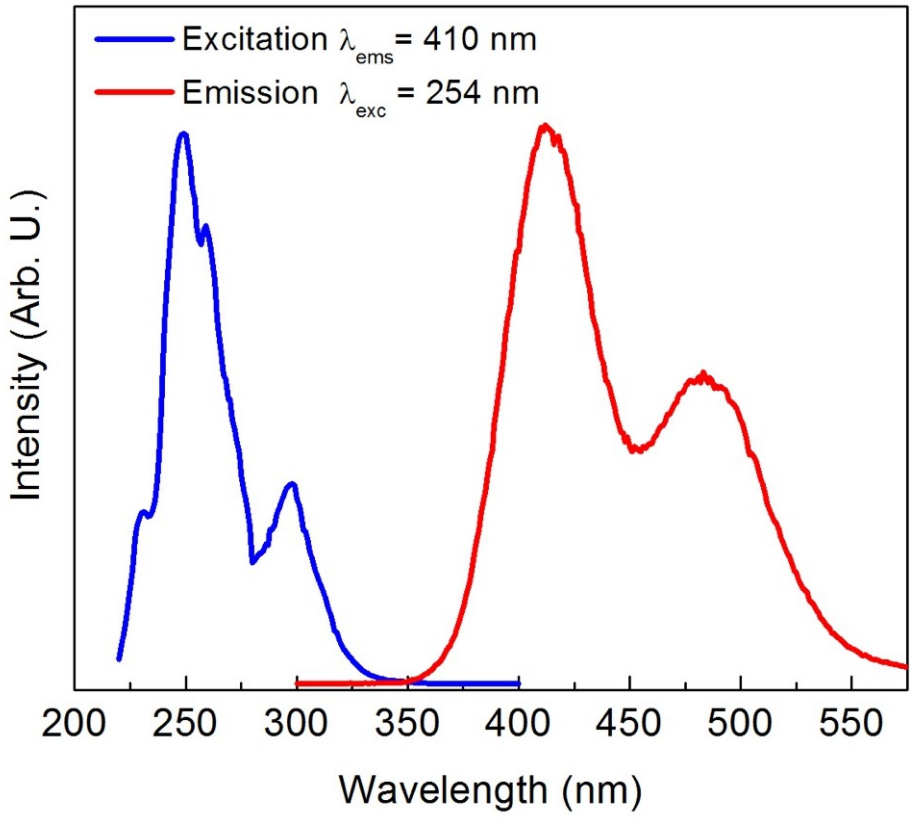

Figure 4.2 Excitation (blue) and emission (red) spectra of CaS nanoparticles.

The optical properties of annealed CaS nanoparticles were characterized by luminescence spectroscopy. Figure 4.2 shows the excitation spectrum (blue) of the nano-sized host material. This excitation spectrum exhibits two broad bands with maxima at 248 nm and 294 nm. The intense excitation peak (248 nm) corresponds to the transition from the valence band to the edge of the indirect band gap of the nano host. Thus, the experimental CaS indirect band gap obtained is 5 eV (Figure 4.3). This value is in agreement with results reported by Pandey *et al* and Stepanyuk *et al.* [120]

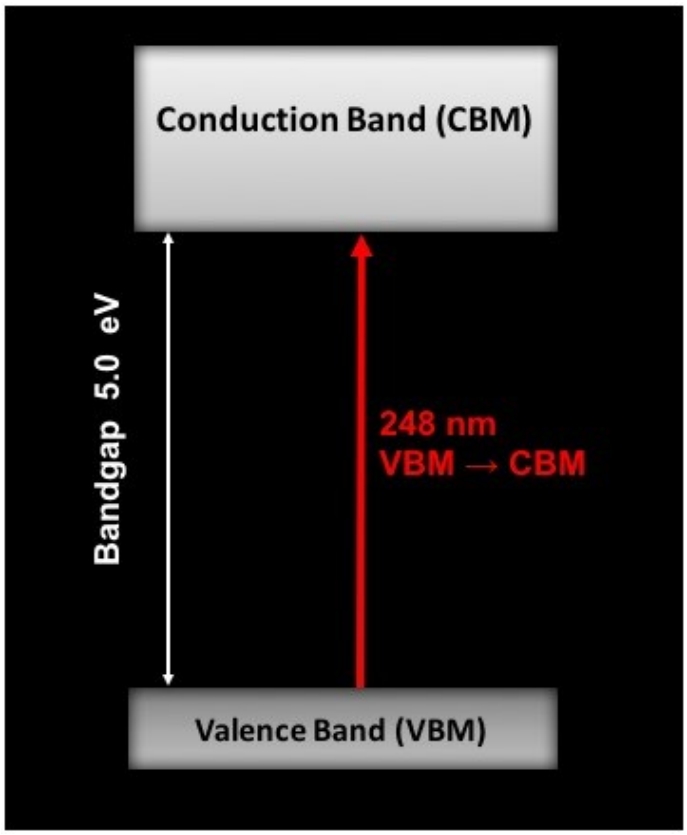

Figure 4.3 Scheme of the VBM → CBM transition in CaS nanocrystals

The second excitation peak at 297 nm (≈4.17 eV) is attributed to intrinsic point defect, such as sulfur vacancies (V_s) in the CaS nanocrystals. These defects form as a consequence of the synthetic method chosen and the post-synthetic heat treatment carried out. The crystal growth of CaS *via* the co-precipitation method leads to the production of a poor crystalline material with localized charge build up in the crystal lattice. During the annealing treatment, V_s defects are readily created in order to neutralize the charge accumulation.[88] These type of defects lead to the formation of 'meta-stable' energy levels that are usually localized below the conduction band and can trap electrons excited from the valance band (Figure 4.4).

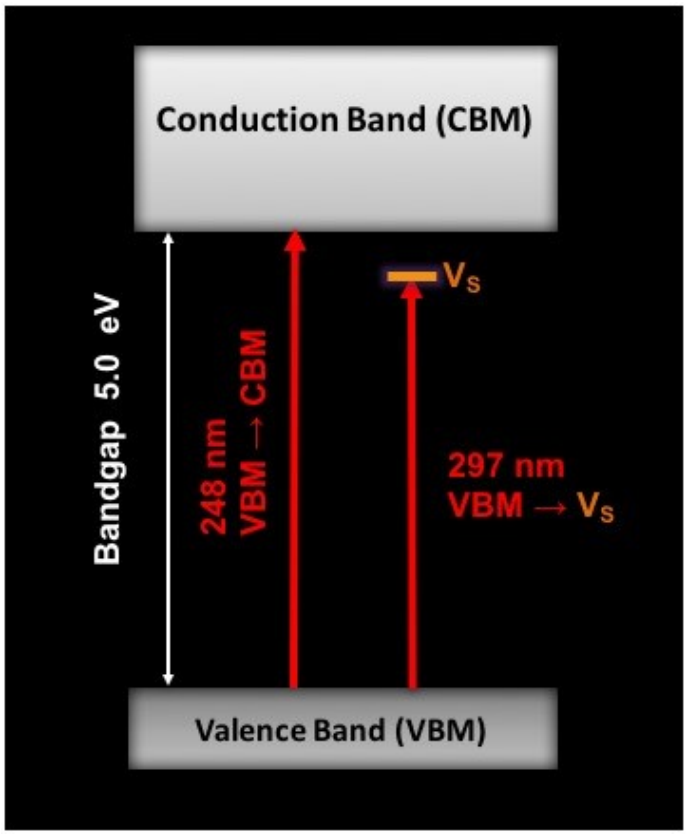

Figure 4.4 Scheme of the VBM → CBM and VBM → V_s transition in CaS nanocrystals

The band gap energy difference of 5 eV and the location of the sulfur vacancies at 4.17 eV from the VBM in the nano host have been confirmed by computational studies carried out by Huang after publication of our results.[98]The author used the DFT + Hubbard U method to calculate the band gap and the defect formation energies of different types of intrinsic defect points and their probabilities to be found in CaS. Computational results revealed an indirect band gap difference of 5.13 eV. In addition, it confirmed that the $V_{s,}$ defects are located 4.21 eV from the valence band, and it is the most probable intrinsic point defect in the CaS nanocrystal, which minimizes the charge build up.

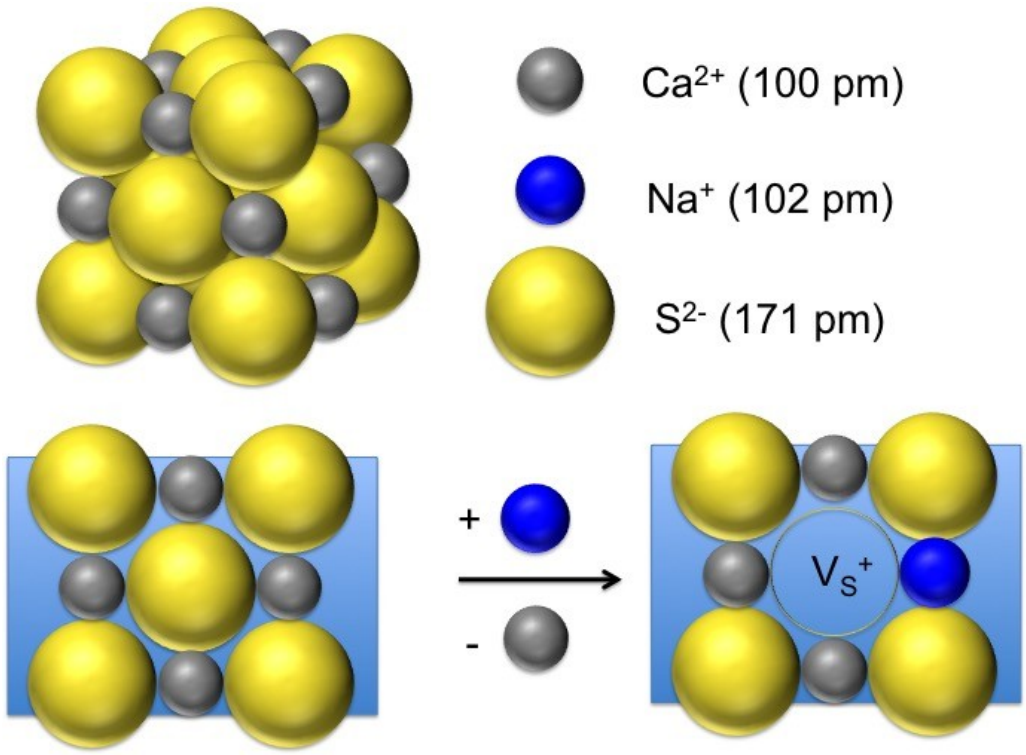

Figure 4.5 Formation of intrinsic defects in the CaS lattice due to the presence of Na^+ impurities.

Following the characterization of the optical properties of the nano host, the emission spectrum of the CaS nanoparticles was measured upon 254 nm irradiation was measured. The emission spectrum is shown in Figure 4.2 (red). It exhibits two broad bands in the range 350 nm to 550 nm attributed to Na^+ ions, optically active impurities, incorporated in the host lattice during the synthesis and annealing treatment. These impurities are intrinsic defects that act as luminescent centres responsible for the blue emission by the host.[88] The presence of Na^+ impurities in the CaS nanocrystals is a result of the use of Na_2S as the sulfide precursor. The incorporation of Na^+ ions (ionic radius of 102 pm) in the Ca^{2+} (ionic radius of 100 pm) cationic sites of the crystal is facilitated since their ionic radii are very similar. The introduction of a Na^+ ion in Ca^{2+} site induces a +1 charge imbalance that can be neutralized *via* the formation of a V_s defect with one electron trapped (V_s^+). Thus, acting as electron storage centers (Figure 4.5).

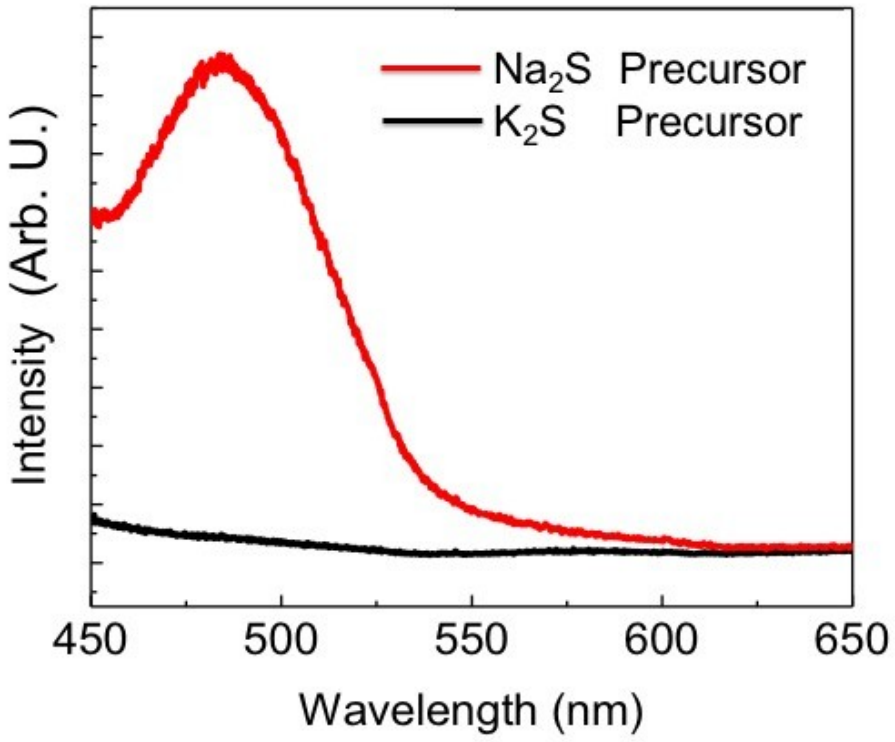

Figure 4.6 Emission spectra of CaS nanoparticles using two different sulphide precursors: Na_2S and K_2S (λ_{exc} = 254 nm)

To further confirm the introduction of the Na^+ ions as impurities, CaS nanoparticles were synthesized using K_2S as the sulphide precursor. The resulting nanoparticles do not exhibit any luminescence upon UV irradiation. The emission spectrum of these nanoparticles is shown in Figure 4.6 which shows the absence of the broad bands in the blue-green region. This is attributed to the fact that the ionic radius of the K^+ ion (138 pm) is significantly larger than that of Ca^{2+} ion (ionic radius of 100 pm). Since the presence of Na^+ induces the formation of electron trapping sites that may have an effect in the lengthening of the persistent luminescence, it was decided to maintain Na_2S as the sulphide source.

4.1.3 Introduction of Eu^{2+} as the emitting centre

From the different materials that have been studied as persistent luminescent hosts, alkaline earth sulfides draw attention as hosts that offer the largest crystal field splitting of the Eu^{2+} emitting centres favouring red persistent luminescence emission. The most common oxidation state of europium is +3, and there are not Eu^{2+} salt precursors that are soluble in ethanol, which can be introduced in the proposed synthetic procedure. However, Eu^{3+} can be easily reduced to the divalent state in a reducing atmosphere, thus $Eu(NO_3)_3{\cdot}5H_2O$ was used as the source to introduce Eu^{3+} as the dopant ion to replace the Ca^{2+} ions, producing CaS:Eu^{3+} nanoparticles. The introduction of an Eu^{3+} ion in Ca^{2+} site will translate in the formation of more lattice defects as consequence of the charge imbalance. Annealing the product using sulfur powder in a reducing atmosphere produces Eu^{2+}. Furthermore, the Eu^{2+} ions are more stable than the trivalent form in alkaline earth sulfides since Eu^{2+} minimizes some of the local charge imbalance produced in the introduction of Eu^{3+} ions.[121]

To determine the effect of the annealing temperature on reducing the Eu^{3+} to Eu^{2+} in CaS, 10 mg batches were annealed at different temperatures (600°C, 700°C, 800°C and 900°C) for 4 hours with sulfur powder under a flow N_2. The obtained products were characterized by emission spectroscopy (Figure 4.7).

The electronic configuration of Eu^{3+} is [Xe] $4f^7\ 5s^2\ 5p^6$, showing that the 4f orbitals are shielded by the 5s and 5p orbitals. Thus, the Eu^{3+} electronic transitions are observed as narrow lines since there is very little effect from the surrounding ions. In the case of the divalent oxidation state of europium, the electronic configuration is [Xe] $4f^7\ 5s^2\ 5p^6\ 5d$. In this case the 6s electrons are lost, leaving the 5d electrons exposed and more susceptible to be influenced by the surrounding ions, hence broad band emission is expected.[121] The difference in the band shape and broadness was used to ascertain the two oxidation states and the temperature at which complete reduction of the Eu^{3+} to Eu^{2+} was obtained.

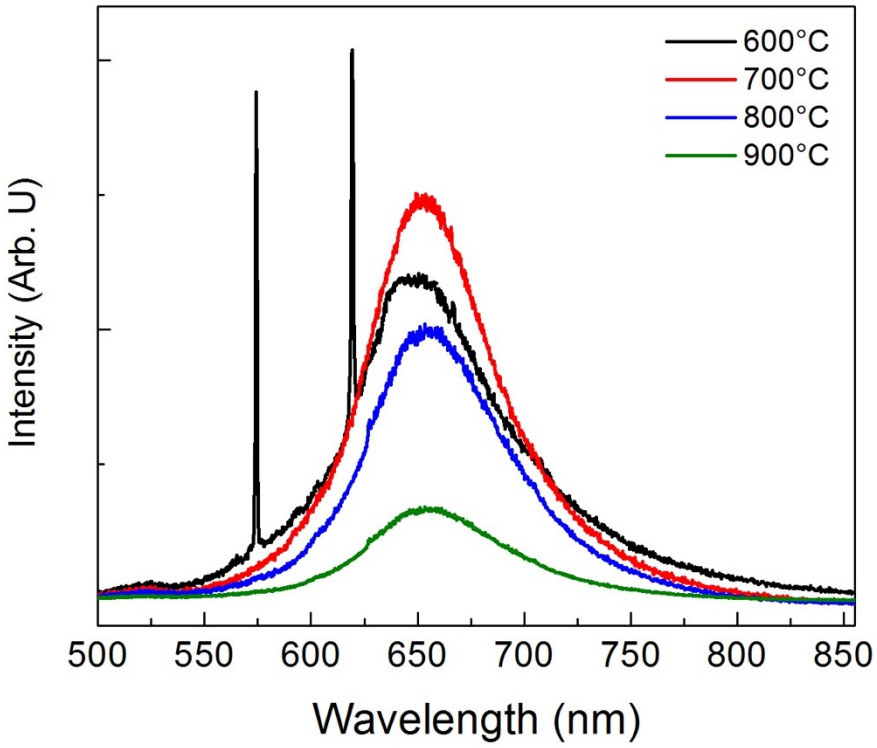

Figure 4.7 Emission spectra obtained after the annealing of CaS:Eu^{3+} (1 mol%) nanoparticles as a function of the temperature (λ_{exc} = 254 nm).

The product obtained after annealing at 600°C is a mixture of white and pink powders. The pink powder is characteristic of the color for Eu^{2+} in CaS whereas the white powder is the unreacted CaS:Eu^{3+}. The emission spectrum (Figure 4.7) reveals both, sharp and broad band peaks. The narrow peaks at 573 nm and 619 nm are attributed to the $^5D_o \rightarrow {}^7F_1$ and $^5D_o \rightarrow {}^7F_2$ transitions of Eu^{3+} respectively, while the broad band peak with a maximum at 650 nm corresponds to the Laporte allowed transition from the $4f^65d$ to the $4f^7$ levels of Eu^{2+} (Figure 4.7).[99, 122] At all other annealing temperatures evaluated, a fine pink powder was obtained and their corresponding emission spectra exhibit only the broad band peak of Eu^{2+}. However, the maximum intensity of the emission was obtained at an annealing temperature of 700°C. Thus, the complete reduction of Eu^{3+} (1 mol% dopant) to Eu^{2+} to produce CaS:Eu^{2+} nanoparticles was achieved *via* annealing for 4 hours at 700°C using sulfur powder under a flow of nitrogen.

Luminescence intensity is dependent on the dopant concentration. Therefore, a study was carried out to optimize the Eu^{2+} emission centres in CaS. This involved the synthesis of CaS:Eu^{3+} with different concentrations of Eu^{3+} in the range of 0.01 mol% to 1 mol%, each sample was annealed using the conditions described above. The luminescence spectra of each sample are shown in Figure 4.8. At all concentrations, the spectra exhibit the characteristic broadband emission of Eu^{2+} ($4f^6 5d^1 \rightarrow 4f^7$). The shape and the band position were found to be independent of the Eu^{2+} concentration. However, the absolute intensity of the band is concentration dependent. The maximum intensity was observed for a concentration of 0.02 mol% of Eu^{2+}. In addition, as the Eu^{2+} concentration increases, the intensity of the band decreases. This is attributed to concentration quenching.

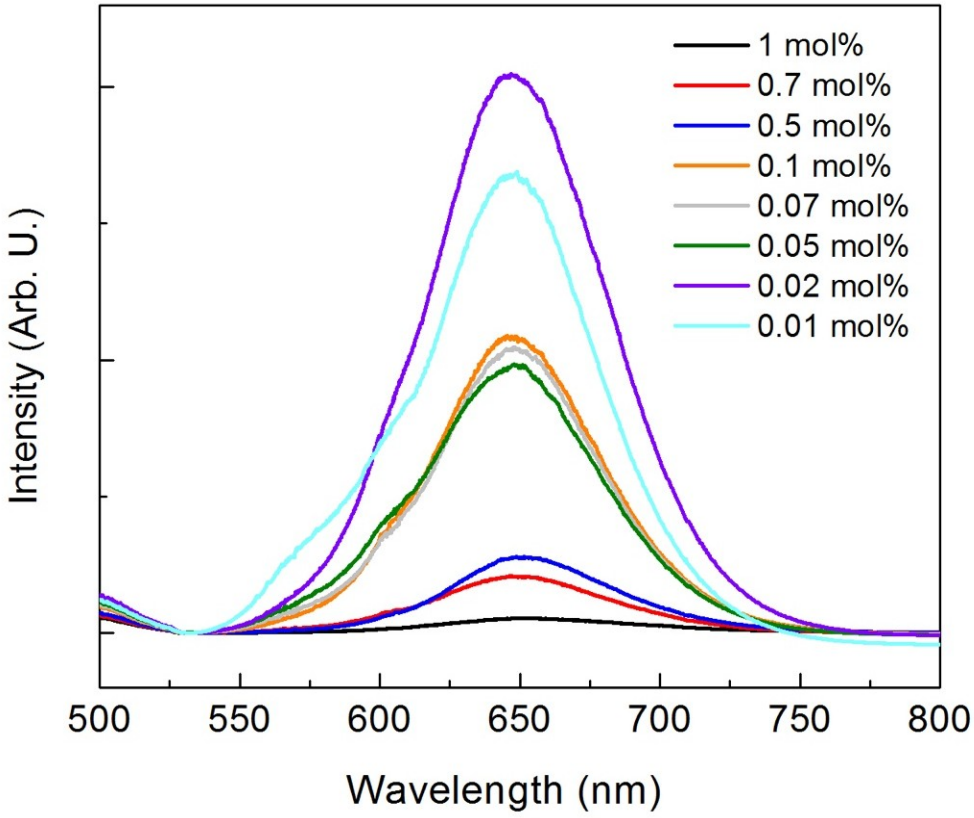

Figure 4.8 Emission spectra of CaS:Eu^{2+} (λ_{exc} = 254 nm). The mol% concentrations are based on the addition of Eu^{3+} precursor in the synthesis reaction.

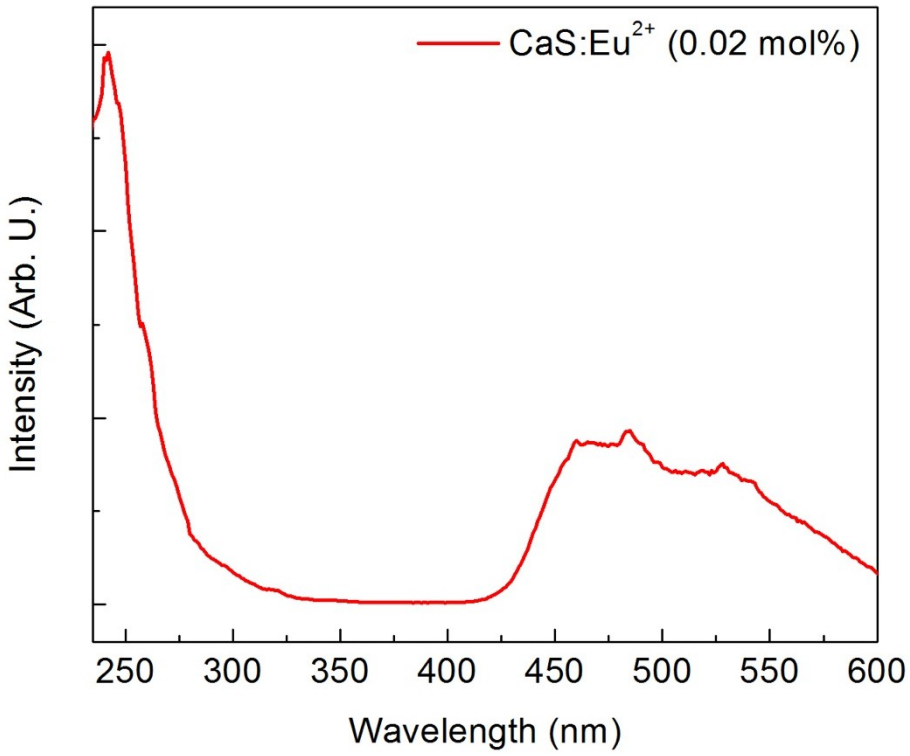

Figure 4.9 Excitation spectrum of CaS:Eu^{2+} (λ_{ems}=650 nm).

The excitation spectrum of the sample with the maximum emission intensity (CaS:Eu^{2+} 0.02 mol%) is shown in Figure 4.9. The peak at 248 nm corresponds to the energy bandgap transition of the nano host CaS. A broad excitation band is observed between 400 to 600 nm related to the $4f^7 \rightarrow 4f^6 5d^1$ transition of Eu^{2+}. The shape of the broad excitation band is in excellent agreement with the results reported by Yamashita *et al.*[123] The sharp lines observed on this broad band arise from the use of the Xe lamp as the excitation source.

From the results obtained from the emission and excitation spectra, it can be established that the energy levels of the Eu^{2+} ions are located within the band gap of the nano-host. Under 254 nm excitation, it is possible to activate these luminescent centres by exciting electrons from the ground state of Eu^{2+} to the conduction band, followed by a non-radiative decay to the $4f^6 5d^1$ excited state and a subsequent red radiative emission ($4f^6 5d^1 \rightarrow 4f^7$) (Figure 4.10).

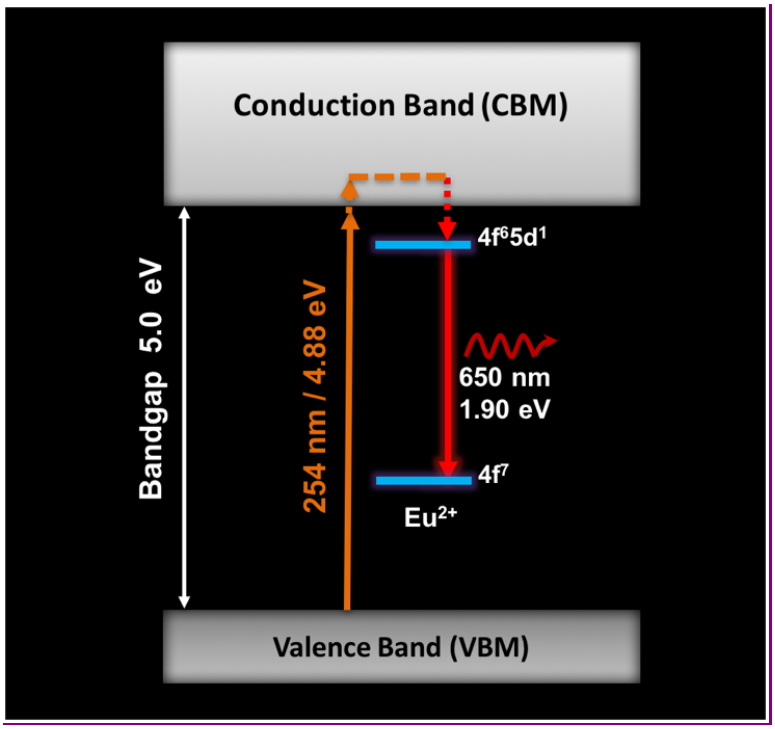

Figure 4.10 Scheme of the luminescence mechanism observed in CaS:Eu²⁺ nanoparticles upon 254 nm irradiation.

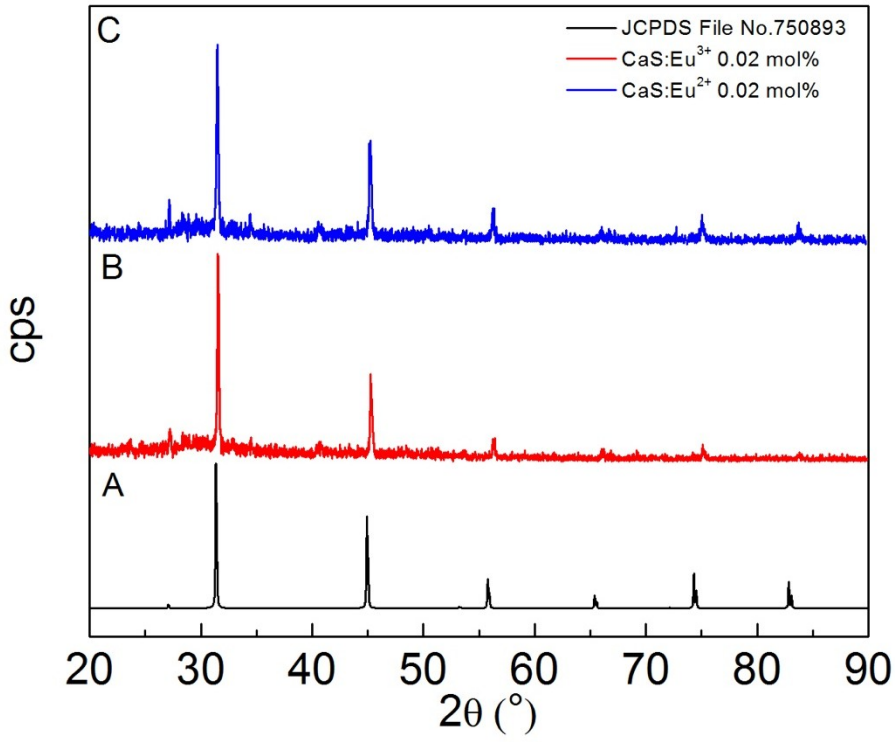

Figure 4.11 XRPD patterns of (A) reference pattern JCPDS File No. 750893, (B) CaS:Eu³⁺ (0.02 mol%) and (C) CaS:Eu²⁺ nanoparticles.

XRPD was used to characterize the crystal phase and crystallinity of CaS:Eu^{3+} (0.02 mol%) nanoparticles and CaS:Eu^{2+} nanophosphors obtained after the annealing treatment. The patterns are shown in Figure 4.11. The XRPD patterns of both CaS:Eu^{3+} and CaS:Eu^{2+} confirm the nanoparticles to be of the cubic phase. The XRPD pattern of CaS:Eu^{2+} (after the annealing treatment), exhibits higher crystallinity than the CaS:Eu^{3+} nanoparticles. The lattice parameters (a) of CaS:Eu^{3+} and CaS:Eu^{2+} were calculated using equation 4.2, with the θ values of the (2 0 0) reflections. In addition, from the line broadening of the same reflection and using equation 4.3, the average crystalline size of each of the samples was calculated and the values are shown in Table 4.3.

Table 4.3 Experimental lattice parameter (a) and particle size (D_{lmn}) of CaS:Eu^{3+} and CaS:Eu^{2+} nanoparticles

Nanoparticle Type	a (Å) ± (Å)	D_{lmn} (nm) ± (nm)
CaS:Eu^{3+}	5.62 ± 0.04	72 ± 10
CaS:Eu^{2+}	5.68 ± 0.04	80 ± 10

The calculated lattice constant of CaS:Eu^{3+} is slightly smaller than the reported lattice constant of 5.694 Å. This decrease is due to the replacement of Ca^{2+} (ionic radius: 100 pm) with Eu^{3+} ions which have a smaller ionic radius (ionic radius: 94.7 pm).[124] In the sample CaS:Eu^{2+}, the Eu^{2+} ion (ionic radius: 117 pm) is occupying the Ca^{2+} sites, which is reflected by an increase in the value of the lattice constant from 5.62 Å ± 0.04 Å to 5.68 Å ± 0.04 Å.

To evaluate the efficiency of doping with Eu^{3+} into the CaS nano host and to determine the final concentration of Eu^{2+} in CaS after the annealing treatment, inductively coupled plasma mass spectrometry (ICP-MS) was used to obtain the concentration of ^{153}Eu. A calibration curve of 5 points was stablished using a SPEX lanthanide multi element standard solution (10 mg/mL) (Figure 4.12). A final concentration of 1.910 ppm of ^{153}Eu was detected which corresponds to 0.018 mol% of ^{153}Eu. Thus, the introduction of Eu^{3+} as a dopant and the annealing treatment are considered to be efficient with a minimal loss of europium.

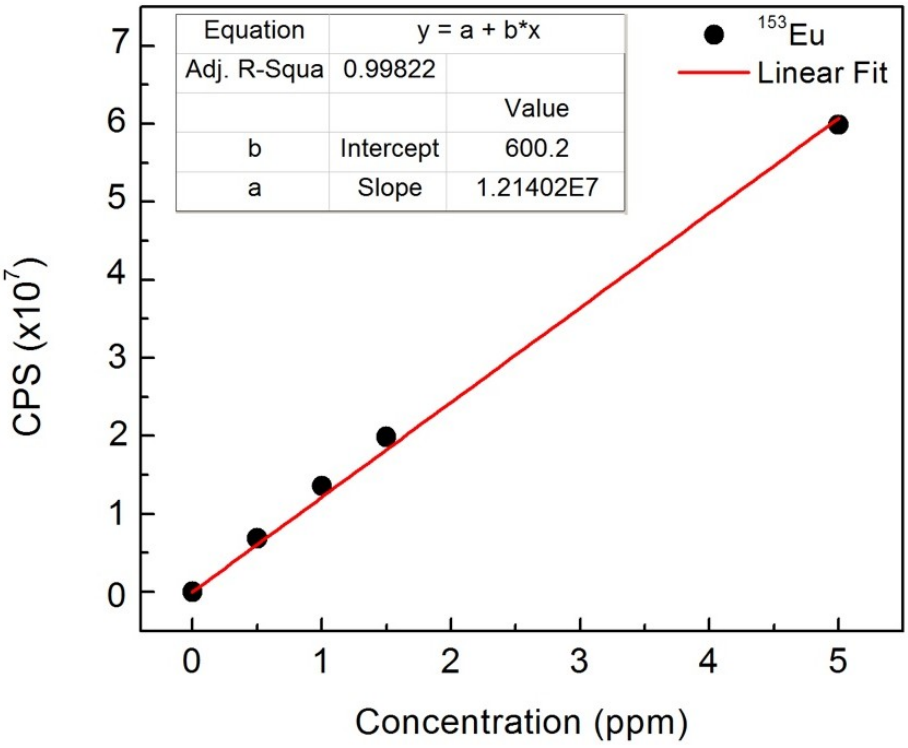

Figure 4.12 ICP-MS Calibration curve for the detection of ^{153}Eu.

4.1.4 Formation of Trapping Sites: Introduction of Dy^{3+}

Trivalent lanthanide ions have been used as co-dopants to extent the duration of the afterglow in hosts showing persistent luminescent. In the development of a CaS based red persistent luminescent material suitable for optical imaging, Dy^{3+} was chosen as the ion to provide the trapping states in the nano host by the substitution of Dy^{3+} ions into Ca^{2+} sites. Three advantages arise from the selection of Dy^{3+} ion as a co-dopant:

I. *A Dy^{3+} ion can occupy a Ca^{2+} site*. Dy^{3+} has an ionic radius of 91.2 pm thus it can be accommodated in a Ca^{2+} site (ionic radius of 100 pm) due to its smaller size but still cause a disruption in the charge balance.[124] This results in the formation of trapping sites in order to maintain the charge neutrality.

II. *It induces the formation of shallow and deeper trapping sites.* The vacuum referred binding energy level scheme constructed for lanthanide doped CaS (Figure 2.17) reveals that Dy^{3+} exhibits energy levels located near the conduction band that could generate shallow traps that can lengthen the persistent luminescence. In addition, it

reveals the presence of energy levels at approximately 1.3 eV below the conduction band. These levels may form trapping sites which can release electrons upon 980 nm photostimulation.

III. *Dy^{2+} ions are not generated.* The annealing conditions used to reduce Eu^{3+} to Eu^{2+} do not reduce Dy^{3+} to Dy^{2+} since the third oxidation energy for europium is higher than that of dysprosium thus favouring the 3+ oxidation state of dysprosium.

$$Dy^{2+} \rightarrow Dy^{3+} + e^{-} \; \Delta E = 2200 \; kJ \; mol^{-1}$$

$$Eu^{2+} \rightarrow Eu^{3+} + e^{-} \; \Delta E = 2400 \; kJ \; mol^{-1}$$

Based on the aforementioned advantages, Dy^{3+} ions were introduced as co-dopants using the same synthetic conditions described for the synthesis of CaS and CaS:Eu^{2+} nanoparticles. Albeit that the exchange of Ca^{2+} by Eu^{3+} and Dy^{3+} is viable due to their comparable ionic radii, it is not energetically favorable because of the difference in the oxidation state. This introduce an additional energy cost related to the formation of defects to neutralize the charge difference. Thus, it was necessary to optimize the reaction time to successfully introduce both trivalent lanthanide ions in the nano host, CaS. In Figure 4.13 the XRPD patterns of CaS:Eu^{3+} /Dy^{3+} as a function of reaction time are shown. After three hours of reaction, diffraction peaks of the cubic crystal phase CaS are observed, however two peaks are present that do not correlate to the reference pattern of CaS (JCPDS File No. 750893). These peaks were attributed to unreacted $Dy(NO_3)_3$. As the time of reaction is increased the signal of the unreacted $Dy(NO_3)_3$ decreases. A reaction time of 16 hours was found to be the optimum time required to obtain CaS:Eu^{3+}/Dy^{3+} nanoparticles.

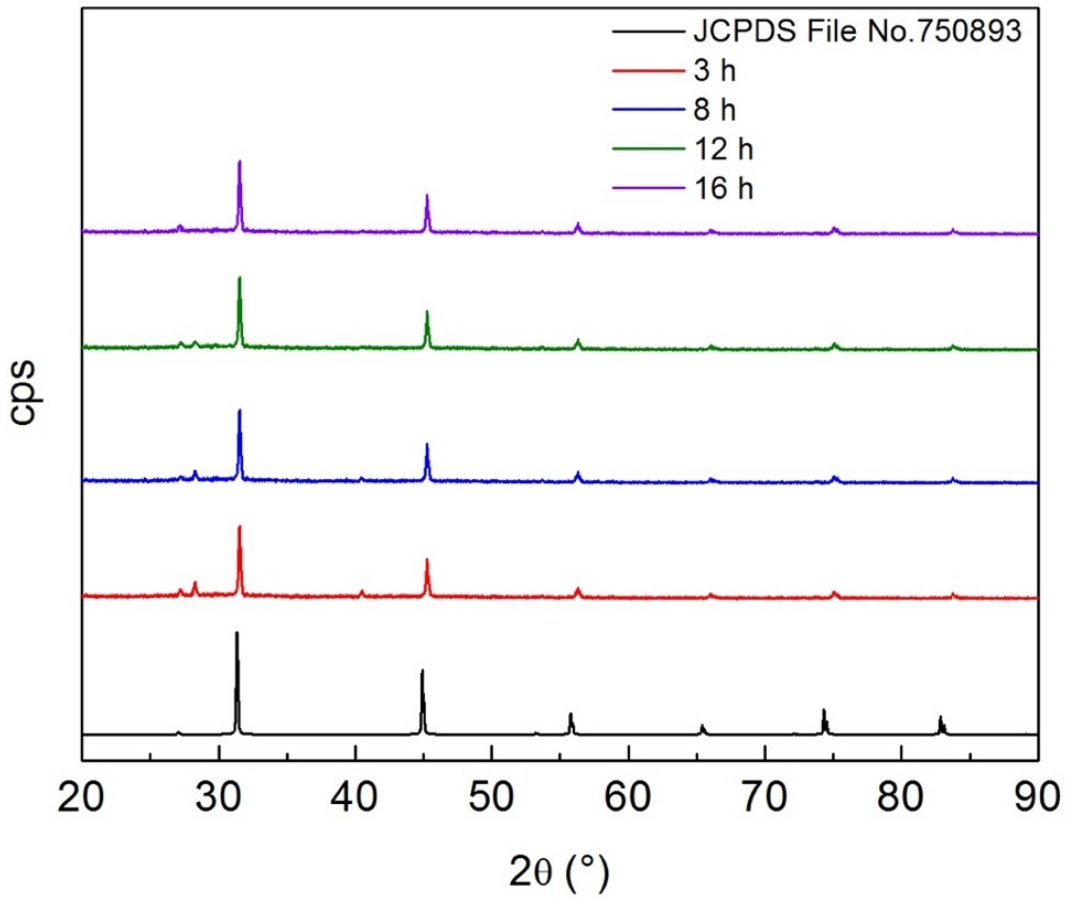

Figure 4.13 XRPD patterns of the CaS:Eu^{3+} (0.02 mol%)/Dy^{3+} (0.002 mol%) nanoparticles as a function of the reaction time.

Following the synthesis, the nanoparticles were annealed at 700°C for 4 hours in the presence of sulfur powder. The XRPD pattern of CaS:Eu^{2+}/Dy^{3+} is shown in Figure 4.14C). It confirms the cubic crystal phase of the product that shows improved crystallinity over the as-synthesized CaS:Eu^{3+}/Dy^{3+} nanoparticles (Figure 4.14B). Using equation 4.2 and 4.3 the lattice parameter (a) and the average crystalline size using the θ values of the (2 0 0) reflections were calculated. The values are shown in Table 4.4. The lattice parameter (5.61 Å ± 0.03 Å) of CaS:Eu^{3+}/Dy^{3+} is smaller due to the smaller ionic radii of the dopant ions. After the reduction of Eu^{3+} to Eu^{2+}, the calculated lattice parameter of 5.65 Å ± 0.03 Å, which is in excellent agreement with the lattice parameter reported for the cubic CaS (5.694 Å). The calculation of the D_{lmn} from the line broadening of CaS:Eu^{3+}/Dy^{3+} and CaS:Eu^{2+}/Dy^{3+} reveals a particle size of 78 nm ± 15 nm and 85 ± 15 nm respectively. No significant change in the size of the nanocrystals are observed because of the annealing process.

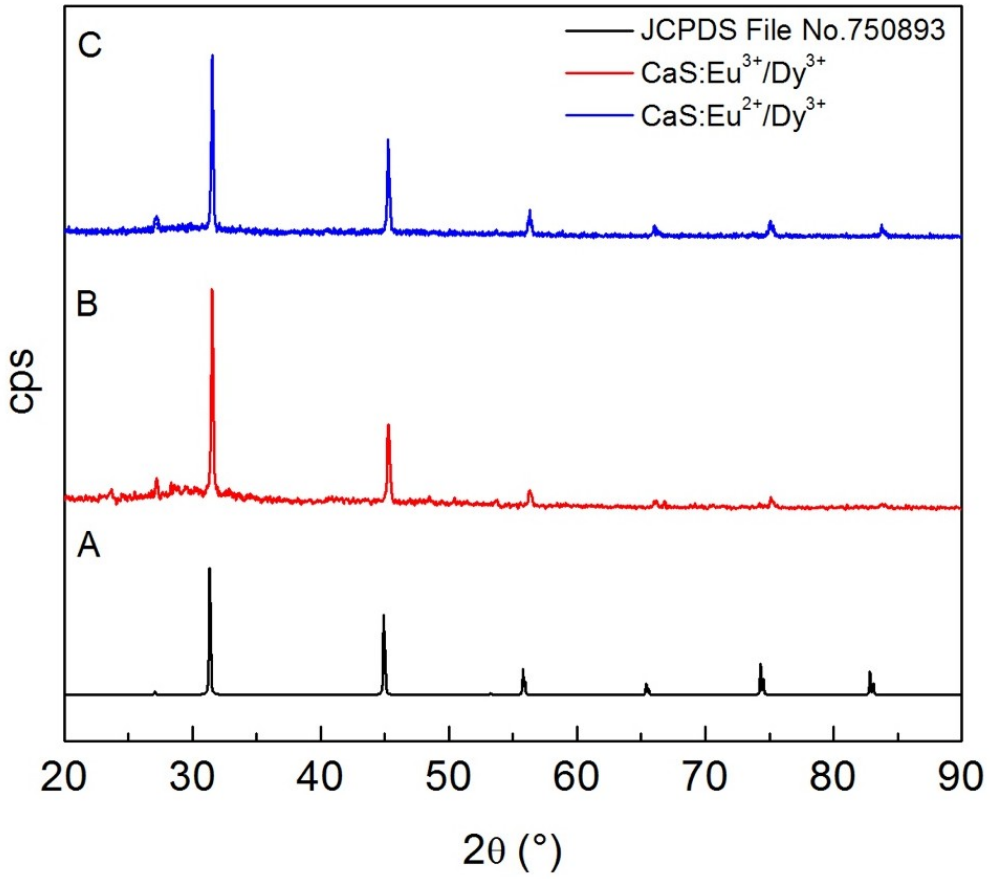

Figure 4.14 XRPD patterns of (A) reference pattern JCPDS File No. 750893, (B) CaS:Eu^{3+} (0.02 mol%)/Dy^{3+} (0.002 mol%) nanoparticles and (C) CaS:Eu^{2+} (0.02 mol%)/Dy^{3+} (0.002 mol%) nanophosphors.

Table 4.4 Experimental lattice parameter (a) and particle size (D_{lmn}) of CaS:Eu^{3+}/Dy^{3+} nanoparticles and CaS:Eu^{2+}/Dy^{3+} nanophosphors

Nanoparticle Type	a (Å) ± (Å)	D_{lmn} (nm) ± (nm)
CaS:Eu^{3+}/Dy^{3+}	5.61 ± 0.03	78 ± 15
CaS:Eu^{2+}/Dy^{3+}	5.65 ± 0.03	85 ± 15

The optimum concentration of Dy^{3+} that would favor a strong emission of red light at 650 nm and the release of trapped electrons at room temperature conditions was established by carrying out a study of the emission intensity as a function of the concentration of Dy^{3+} in the range of 0.001 mol% to 1 mol% and using a constant concentration of 0.02 mol% of Eu^{2+} which is the concentration that shows the maximum luminescence intensity (Figure 4.8). The emission spectra of the CaS:Eu^{2+}/Dy^{3+}

nanophosphor doped at different concentrations of Dy^{3+} excited upon UV irradiation are shown in Figure 4.15.

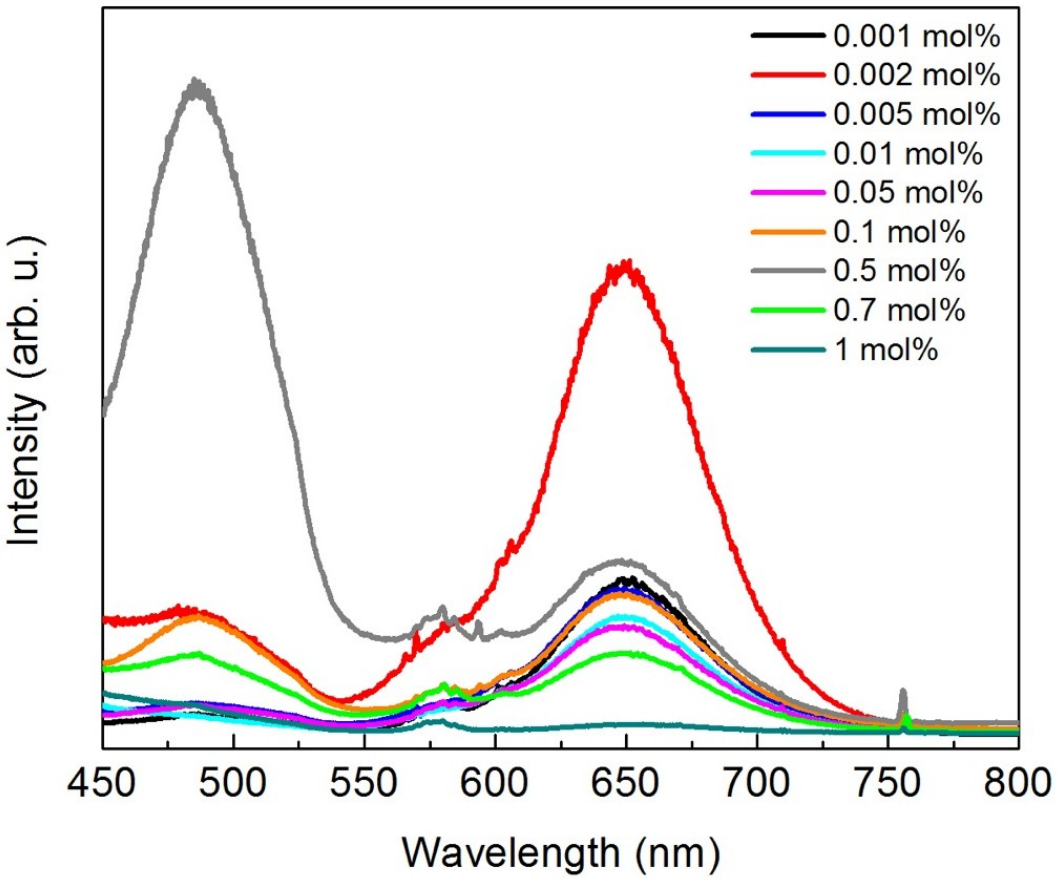

Figure 4.15 Emission spectra for CaS:Eu^{2+} (0.02 mol%)/Dy^{3+} (X mol%) upon 254 nm excitation.

The spectra of these samples exhibit four distinct emission bands (Figure 4.15). The red emission broad band with a maximum at 650 nm corresponds to the $4f^6 5d^1 \rightarrow 4f^7$ transition of Eu^{2+}. The broad band in the blue region at 486 nm corresponds to the emission from the intrinsic defects created in CaS as a result of using Na_2S in the synthesis procedure. This was discussed in section 4.1.2 and shown in Figure 4.6. The other two bands observed at 580 nm and the narrow peak at 756 nm are assigned to the $^4F_{9/2} \rightarrow {}^6H_{13/2}$ and the $^4F_{9/2} \rightarrow {}^6H_{9/2}$ respectively, in agreement with the assignments reported for Dy^{3+}.[125] The maximum emission intensity is observed at a Dy^{3+} concentration of 0.002 mol%. At higher concentrations of Dy^{3+} ions, a significant quenching of the red emission occurs, because of

the significantly higher number of Dy^{3+} ions as emission centers than the Eu^{2+} ions. This translates in a higher probability of radiative de-excitations occurring from the Dy^{3+} energy levels than from the $4f^6 5d^1$ of Eu^{2+} ions.

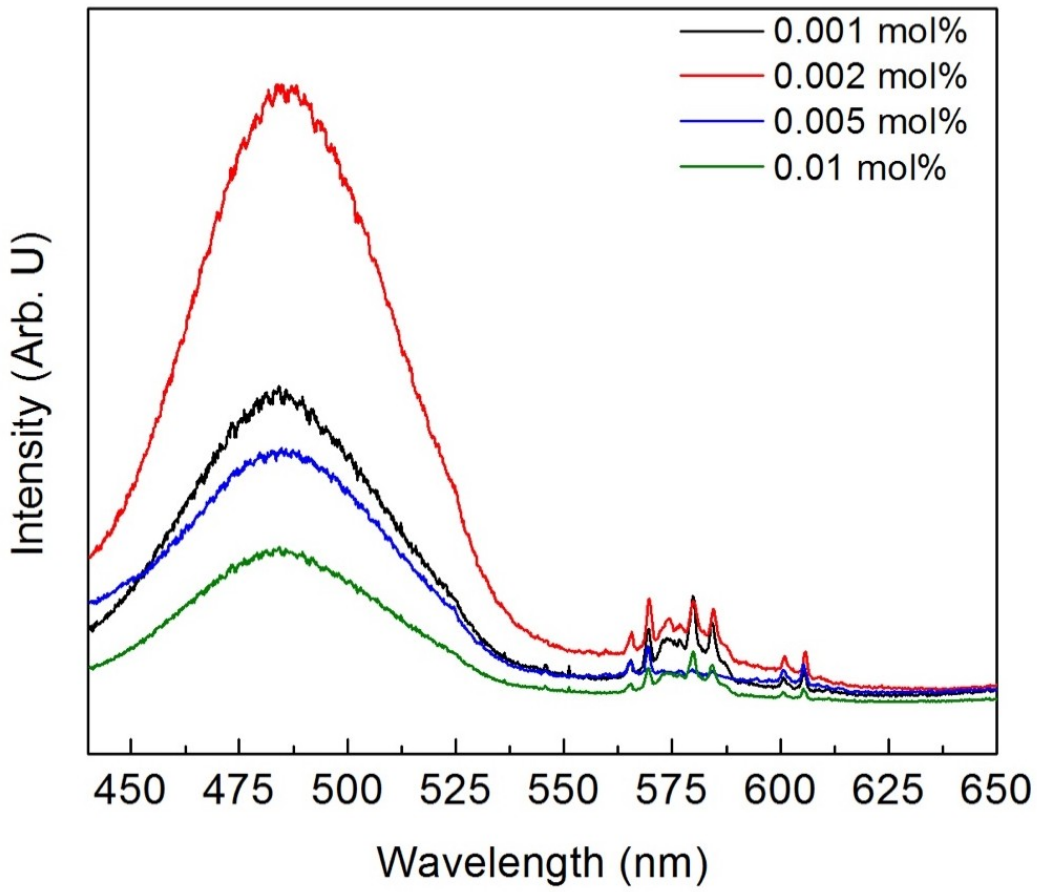

Figure 4.16 Emission spectra for CaS: Dy^{3+} upon 254 nm excitation using Na_2S as the sulfide precursor (Dy^{3+} mol% varied from 0.001 to 0.01 mol%).

CaS:Eu^{2+} (0.02 mol%)/Dy^{3+}(0.5 mol%) exhibits white luminescence upon 254 nm irradiation that persist after the excitation has been switched off. This emission is consequence of the combination of red, green and blue emissions. In the blue-green region there is an overlap of the emission peaks that originate from the intrinsic defects and Dy^{3+} ions. In order to clearly identify the emission peaks of the Dy^{3+} ion in this region, CaS:Dy^{3+} nanoparticles were synthesized using Na_2S and K_2S sulfide precursors, and varying the concentration of Dy^{3+} from 0.001 mol% to 0.01 mol%. In Figure 4.16 the emission spectra

of the CaS:Dy^{3+} nanoparticles synthesized using Na_2S as the sulfide precursor are shown. The spectra exhibit a broad band in the blue-green region attributed to the Na^+ ions introduced in the nano host as a consequence of the favored $Na^+ \rightarrow Ca^{2+}$ exchange during the synthesis procedure. In the yellow region, the transition, $^4F_{9/2} \rightarrow {}^6H_{13/2}$ of Dy^{3+} is observed. On the contrary, when K_2S precursor is used and the cation exchange is not favored, the intrinsic defect emission band is not observed, however the $^4F_{9/2} \rightarrow {}^6H_{15/2}$ transition of Dy^{3+} is clearly observed (Figure 4.17). Thus, the overlapping of emission peaks from the intrinsic defects and Dy^{3+} ions contribute to the total emission of blue light that combine with the yellow transition of Dy^{3+} and the red emission of Eu^{2+} produce white persistent luminescence.

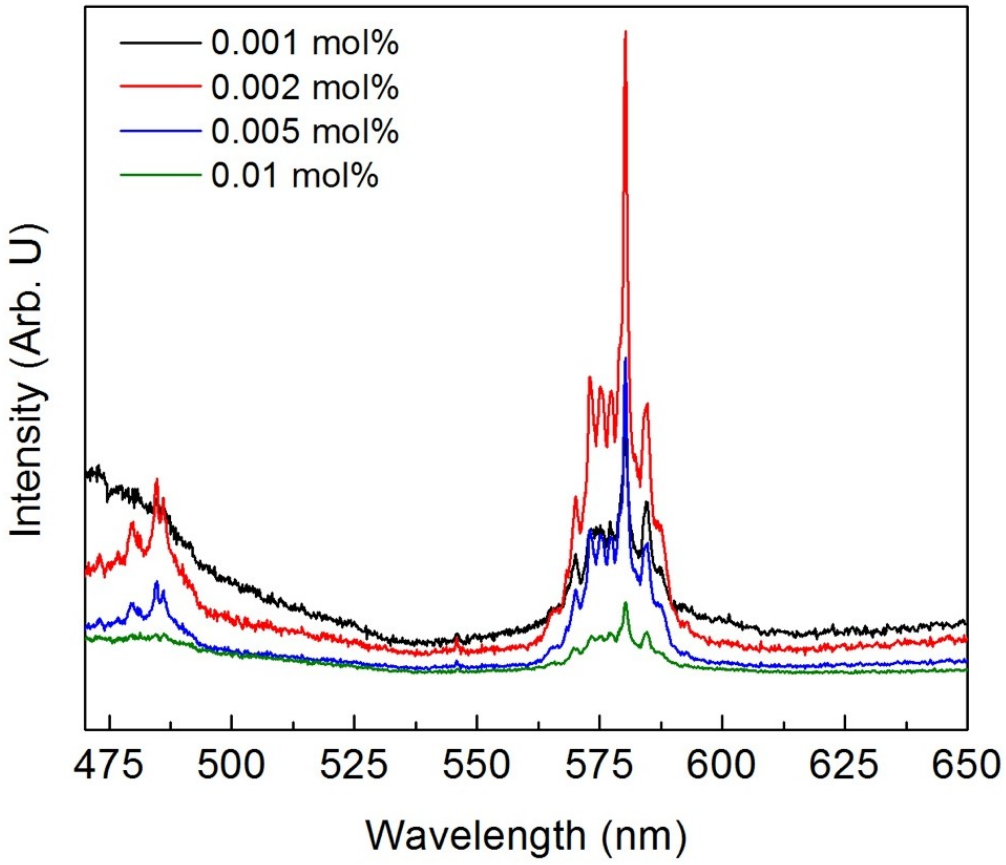

Figure 4.17 Emission spectra for CaS: Dy^{3+} upon 254 nm excitation using K_2S as the sulfide precursor (Dy^{3+} mol% varied from 0.001 to 0.01 mol%).

The strong red emission of the CaS:Eu^{2+}(0.02 mol%)/Dy^{3+}(0.002 mol%) sample was one of the important characteristics that was key to choosing this sample as the potential candidate for optical imaging applications. The excitation spectrum shown in Figure 4.18 does not show any significant changes from the one reported above for the CaS:Eu^{2+} nanoparticles. It exhibits the peak at 248 nm that corresponds to the energy bandgap transition of CaS and the broad excitation band in the region 400 to 600 nm related to the $4f^7 \rightarrow 4f^6 5d^1$ transition of Eu^{2+}.

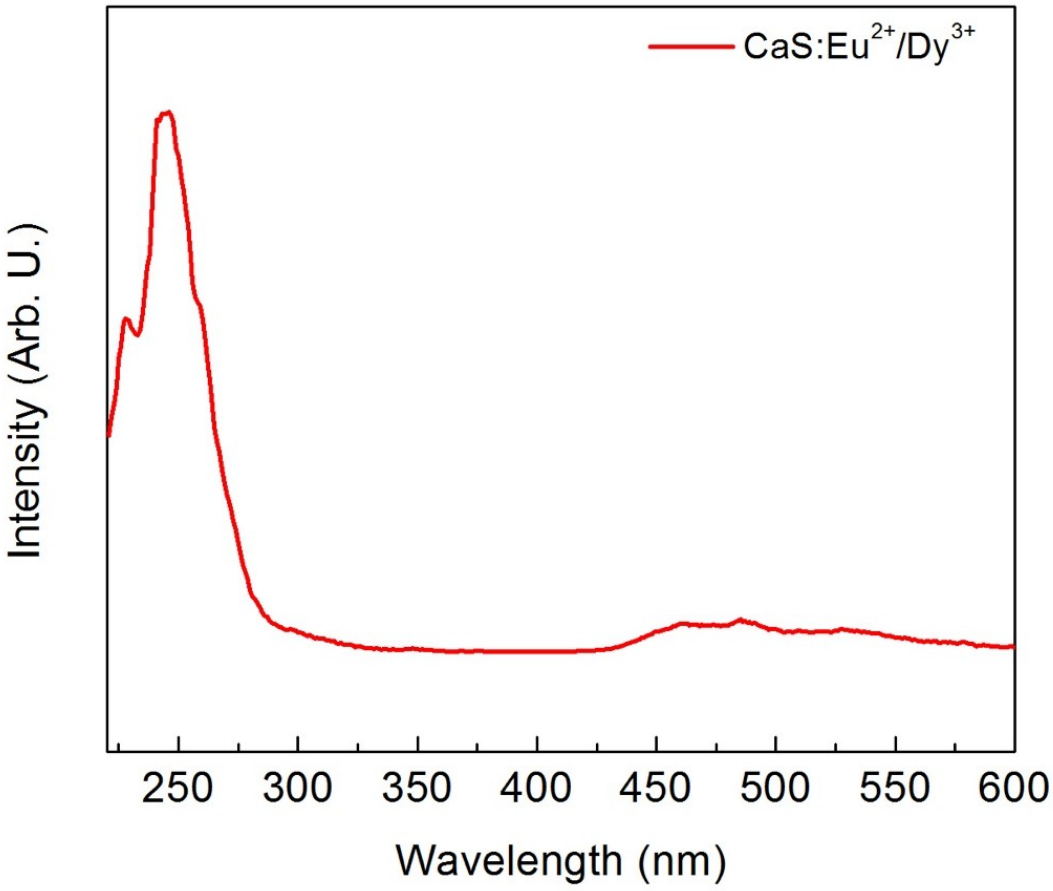

Figure 4.18 Excitation spectrum of CaS:Eu^{2+} (0.02 mol%)/Dy^{3+} (0.002 mol%) nanophosphors (λ_{ems} = 650 nm).

In addition, ICP-MS was used to determine the doping concentration of ^{153}Eu and ^{163}Dy in the CaS nanoparticles. Using calibration curves for concentration of ^{153}Eu (Figure 4.12) and ^{163}Dy (Figure 4.19), final concentrations of 1.634 ppm of ^{153}Eu and 0.191 ppm of ^{163}Dy were detected which corresponds to 0.017 mol% and 0.0016 mol% respectively. These results agree with the initial concentration used in the mixture.

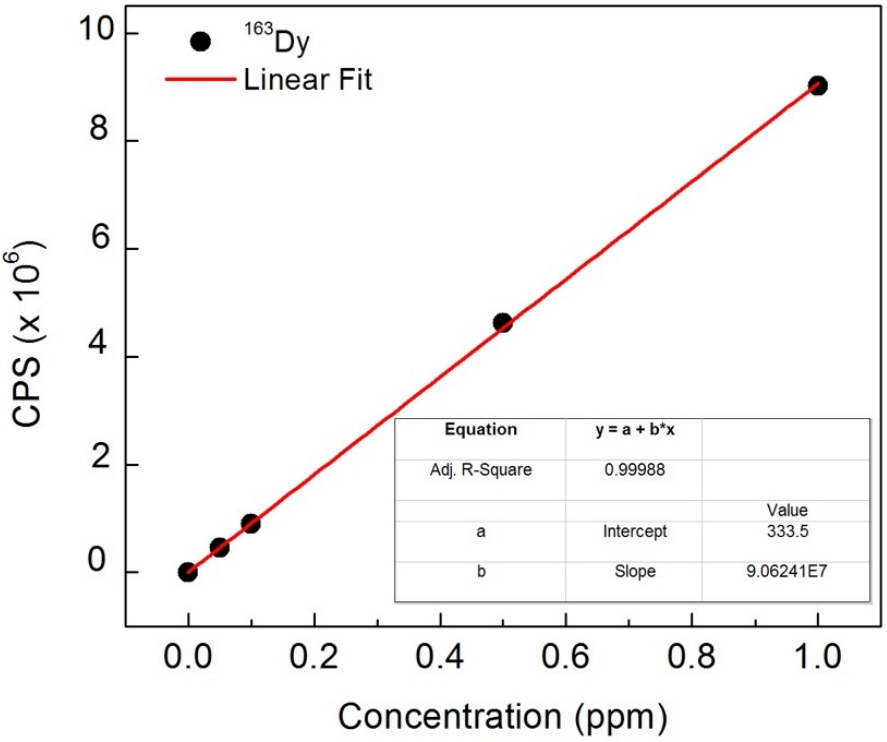

Figure 4.19 ICP-MS Calibration curve for the detection of ^{163}Dy.

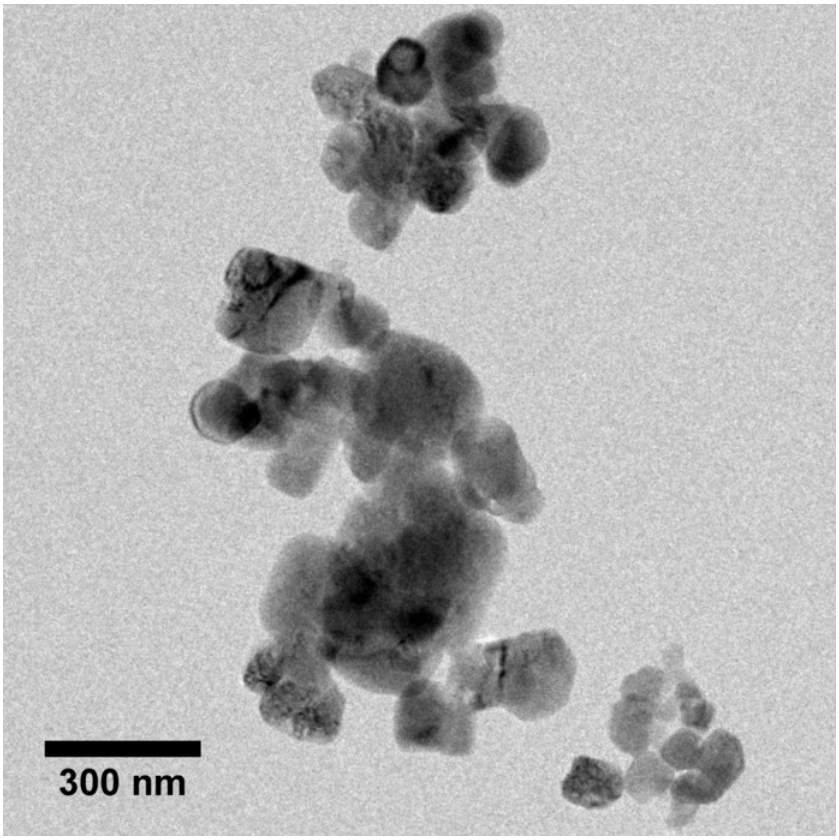

Figure 4.20 TEM of CaS:Eu^{2+} (0.02 mol%)/Dy^{3+}(0.002 mol%) nanophosphors (scale bar: 300 nm).

A consequence of the annealing process required for the reduction of Eu^{3+} ions is the a high degree of agglomeration exhibited by the CaS:Eu^{2+}/Dy^{3+} nanophosphors due to the high temperature and the annealing time required.[126] Figure 4.20 shows a TEM image of CaS:Eu^{2+}/Dy^{3+} after the annealing treatment. Proposed post-synthetic alternatives to disrupt the agglomeration of nanoparticles are rotor stator mixers, piston homogenizers, wet milling and direct ultrasonication using sonication probes. Among the alternatives, ultrasonication is the most used technique to de-agglomerate and disperse nanoparticles in a liquid media as it can be used from low to high viscosity media and in a large range of volumes.[127] Nanoparticles that show agglomeration require application of a high stress process in order to overcome the adhesion forces. The stress needed can be provided by ultrasonic vibrating waves with a fixed amplitude propagating through a liquid medium. As the waves propagate, alternating compression (high-pressure) and rarefaction (low-pressure) cycles are generated. During the rarefaction cycle, the average distance between agglomerates decreases below a critical distance generating the formation of cavities

(bubbles). When the pressures increases, the distance between agglomerates decreases, forcing the cavities to collapse.[127] The collapse of bubbles, also known as cavitation, causes the release of a large amount of energy that generates a mechanical stirring effect with shock waves and micro-jets that cause the disruption of agglomerates.[128]

Direct ultrasonication was carried out by inserting a sonication probe directly into the liquid media where the nanophosphors were suspended. Using a frequency of 30 KHz, different ultrasonication times were investigated (1 min to 5 min) in dispersions of CaS:Eu^{2+}/Dy^{3+} nanophosphors in ethanol at an approximate concentration of 0.5 mg/mL. TEM images after ultrasonication process and the particle size distribution of the CaS:Eu^{2+}/Dy^{3+} nanophosphors obtained from the counting of 100 nanoparticles are shown in Figure 4.21. The TEM images revealed that the agglomeration exhibited by the nanophosphors was disrupted, producing individual nanoparticles. The average sizes after 1, 2 and 3 min of ultrasonication are 150 nm ± 28 nm, 108 nm ± 32 nm and 82 nm ± 32 nm respectively. Although a broad size distribution is still observed, a significant decrease in the average size is obtained because of the disruption of the large agglomeration of nanophosphors. After 3 minutes of ultrasonication, it was observed that the highest population of nanoparticles (75%) was below 100 nm in comparison to the other studied ultrasonication times. On the other hand, a significant increase in the average size at ultrasonication times higher than 3 min is observed. Average sizes of 109 nm ± 34 nm and 161 nm ± 50 nm was measured after 4 and 5 min of ultrasonication respectively. This increase in the average size is attributed to an Ostwald ripening process. The nanoparticles with particle sizes below 40 nm obtained after 3 min of ultrasonication are no longer observed after 5 min of ultrasonication. Thus, dissolution of the small nanocrystal followed by the deposition of the material to the larger nanophosphors may be occurring increasing the average size.

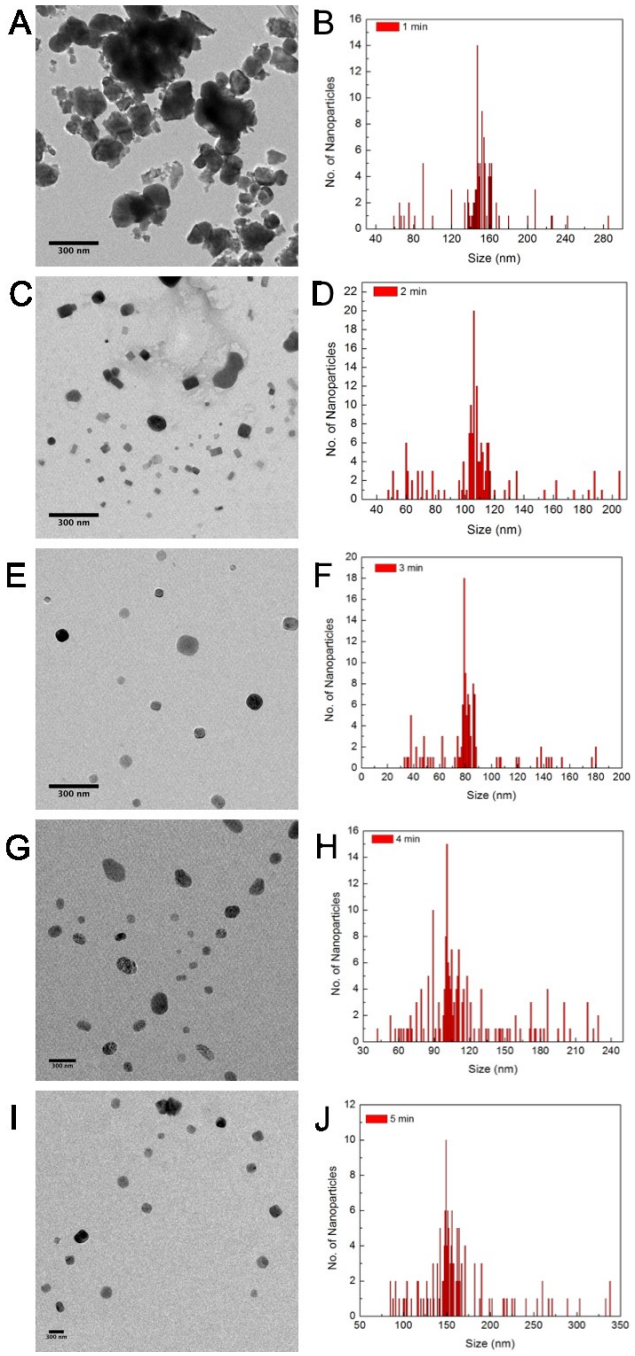

Figure 4.21. TEM and particle size distribution of CaS:Eu^{2+}/Dy^{3+} nanophosphor after (A-B) 1, (C-D) 2, (E-F) 3, (G-H) 4 and (I-J) 5 min of ultrasonication at 30 KHz.

Furthermore, ultrasonication at 30 KHz for 3 minutes was carried out in CaS nanoparticles, CaS:Eu^{2+} and CaS:Eu^{2+}/Dy^{3+} nanophosphors dispersed in ethanol. The nanocrystals were precipitated and analyzed by XRPD, and it was found that all experimental patterns measured agree with the pattern reported in the literature, confirming that the ultrasonication process do not modify or alter the crystal phase and crystallinity of the nanocrystals (Figure 4.22).

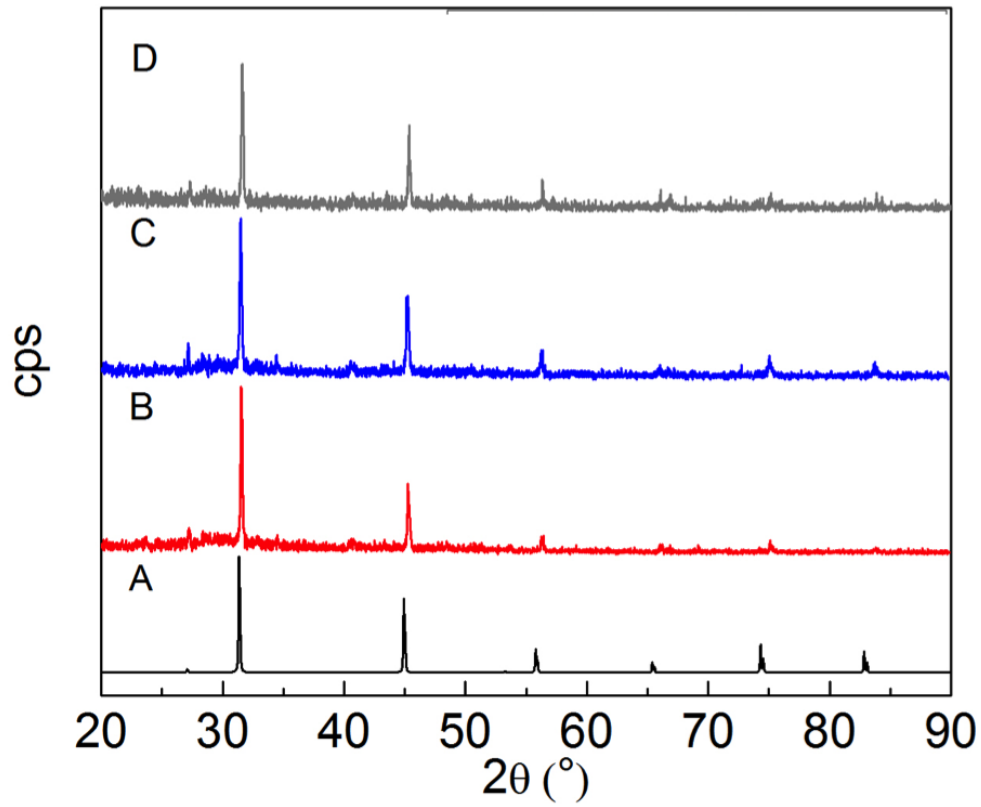

Figure 4.22. XRPD Patterns of (A) Reference Pattern JCPDS File No. 750893, (B) CaS nanoparticles, (C) CaS:Eu^{2+} (0.02 mol%) and (D) CaS:Eu^{2+}/Dy^{3+} (0.02 mol%/0.002 mol%). All XRPD patters were measured after ultrasonication (3 min, 30 KHz).

4.2 Persistent an NIR Photostimulated Red Luminescence of CaS:Eu^{2+}/Dy^{3+} Nanophosphors

Upon 254 nm irradiation CaS nanoparticles, CaS:Eu^{2+} and CaS:Eu^{2+}/Dy^{3+} nanophosphors exhibit a characteristic and common luminescent property, persistent luminescence. The generation and duration of a persistent luminescent emission exhibited by the CaS nano host and the CaS:Eu^{2+} and CaS:Eu^{2+}/Dy^{3+} nanophosphors originates in the trapping centres found within. As it has been discussed, trapping centres are readily created to neutralize local charge build up due to the presence of intrinsic defects such as anionic vacancies or the introduction of impurities or dopant ions in the crystal lattice.

4.2.1 Persistent Luminescence and Thermoluminescence Studies

In order to characterize the trapping centres and elucidate the trapping mechanism of the persistent luminescence exhibited by CaS nanoparticles, CaS:Eu^{2+} and CaS:Eu^{2+}/Dy^{3+} nanophosphors, wavelength-resolved thermoluminescence studies were carried out. To determine the location of the trapping centres with respect to the conduction band (trap depths), the Urbach empirical formula (Equation 2.22) was used.

4.2.1.1 CaS Nano Host

The characterization of the trapping centres formed in the CaS nano host and responsible for the blue persistent luminescence was carried out by measurement of its thermal glow curve. CaS nanoparticles were cooled down to 10 K and irradiated with UV light (254 nm for 10 min). The irradiation was switched off and the nanoparticles were heated at a constant heating rate of 10 K min^{-1} from 10 K to 650 K and the thermal-stimulated luminescence was recorded as a function of the temperature.

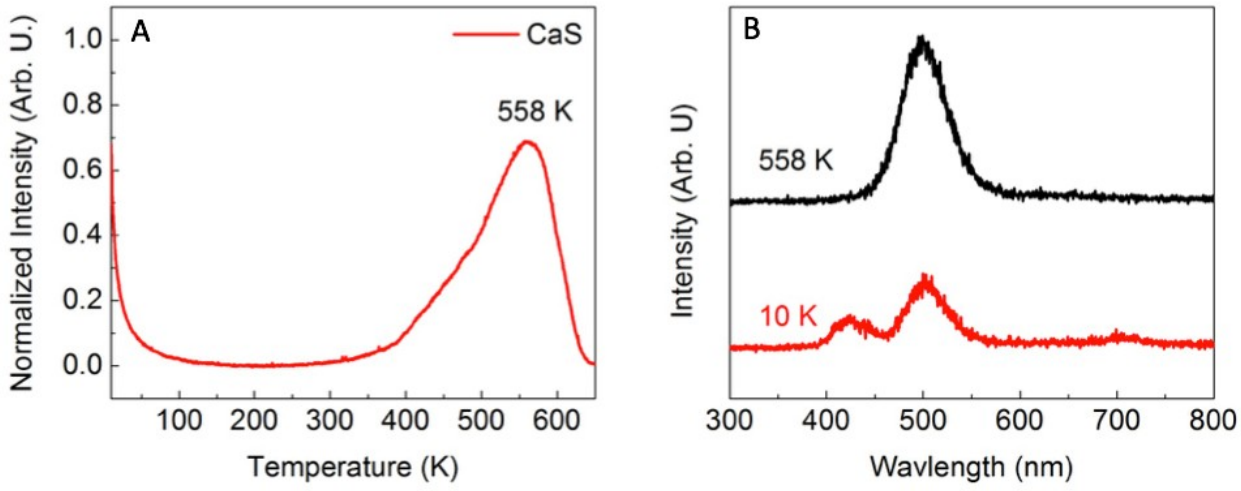

Figure 4.23 (A) Thermal glow curve and (B) thermally stimulated emission spectrum of CaS nanoparticles.

The thermal glow curve for CaS nanoparticles is shown in Figure 4.23A. The glow curve exhibits a fast decay at low temperatures in the range of 10 to 100 K attributed to a fast athermal tunneling recombination process occurring in the proximity of the conduction band, most likely related to electrons being released from shallow traps. A thermal peak is observed with a temperature maximum (T_m) at 558 K that corresponds to intrinsic trapping sites found in the nano host. Using equation 4.4, it was established that these intrinsic trapping sites are located at 1.1 eV below the conduction band. The thermal stimulated emission spectra of each of the identified traps in the thermal glow curve of CaS nanoparticles is shown in Figure 4.23B. At 10 K and 558 K emission in the blue-green and blue region are observed respectively. The emission features at 10K are similar to those observed in the emission spectrum obtained under 254 nm excitation (Figure 4.2); however, a difference in the emission intensity for two bands is observed. The spectrum collected upon UV irradiation represents the intensity of the complete trap distribution (10 to 100 K) whereas the thermally stimulated spectrum collects only the thermal-stimulated luminescence generated a 10 K.

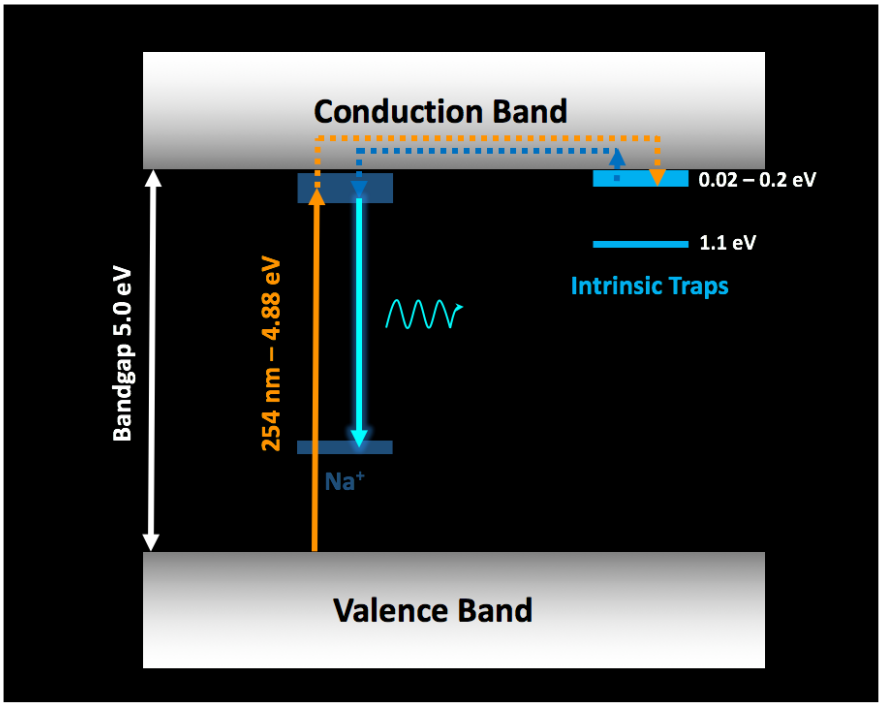

Figure 4.24 Scheme of the electron trapping – detrapping mechanism for CaS nanoparticles.

The generation of the blue-green persistent luminescence at low temperatures is related to the presence of a shallow trap distribution in the range of 0.02 to 0.2 eV (10 to 100K) below the conduction band. At room temperature conditions, a fast release of electrons occur from this trap distribution to the conduction band followed by a rapid recombination in the Na^+ ions emission centers (Figure 4.24). This fast detrapping process translates in a persistent luminescence time of 1.2 min ± 0.4 min shown by the persistent luminescence decay profile (Figure 4.29).

4.2.1.2 CaS:Eu^{2+} Nanophosphors

The thermal glow curve for CaS:Eu^{2+} was recorded using the same linear heating rate and charging time described for the CaS nanoparticle. However, two different charging excitation wavelengths, 254 and 482 nm were used. The thermal glow curves are shown in Figure 4.25A. Both thermal glow curves show two peaks at 120 and 210 K and a fast decay at low temperatures in the range of 10 to 100 K. The latter corresponds to the athermal tunneling recombination observed in the CaS nanoparticles. The most intense peak at 210 K corresponds to the presence of shallow traps at approximately 0.4 eV below the conduction

band. A lower intensity peak at 120 K reveals the presence of other shallow traps located at 0.2 eV below the conduction band. The trapping sites located 120 K and 210 K are shallow traps formed by the introduction of Eu^{3+} as a dopant ion followed by its reduction to Eu^{2+} during the annealing treatment. The generation of the red persistent luminescence exhibited by the CaS:Eu^{2+} nanophosphors arises from the Eu^{2+} $4f^65d^1$ (T_{2g}) → $4f^7$ ($^8S_{7/2}$) transition. At 120 and 210K, the trapped electrons move into the conduction band and nonradiatively decay to the Eu^{2+} emitting level. The thermal stimulated emission spectra is shown in Figure 4.25B.

Intrinsic traps at higher temperatures (400 to 600 K) are only observed following irradiation of the nanophosphors using 254 nm light. Using 482 nm irradiation to charge the nanophosphors, the deeper traps are no longer observed. The absence of these traps is related to the energy required to excite electrons up to the conduction band and non-radiatively decaying into the trapping sites. Using 482 nm excitation, electrons of the ground state are excited to the $4f^65d^1$ energy levels of Eu^{2+} from where they can migrate, to a lesser degree, to the shallow traps located in the vicinity. Once the excitation period is terminated, electrons can rapidly migrate back to the $4f^65d^1$ energy levels follow by the radiative emission to the $4f^7$ ($^8S_{7/2}$) ground state.[129]

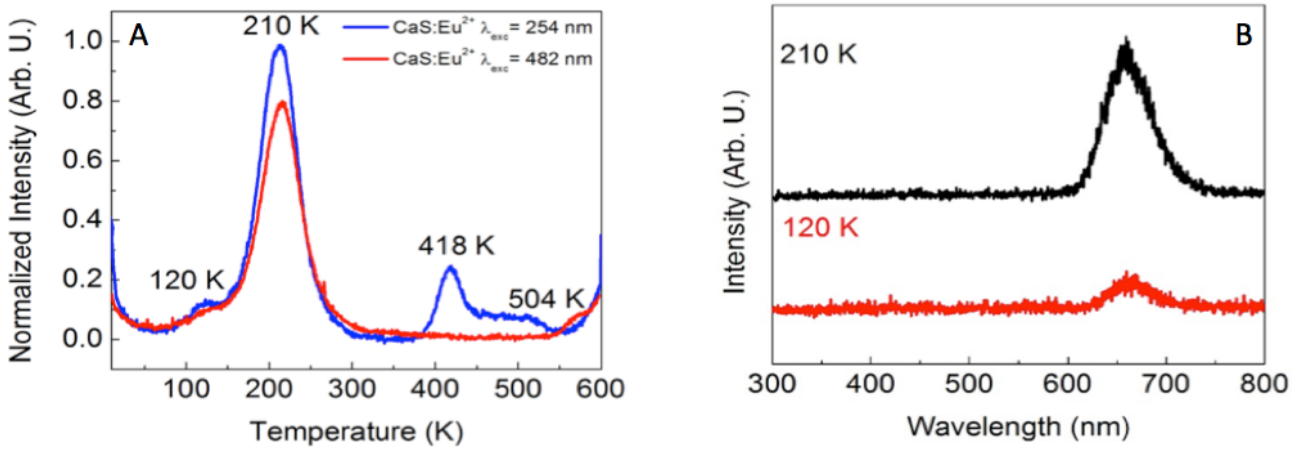

Figure 4.25 (A) Thermal glow curve and (B) thermally stimulated emission spectrum (corresponding to the thermal glow curve after 254 nm irradiation) of CaS:Eu^{2+} (0.02 mol%) nanophosphors.

When the CaS:Eu^{2+} nanophosphors are irradiated with 254 nm light, electrons are promoted from the occupied $4f^7$ levels ($^8S_{7/2}$ ground state) to the conduction band followed by the trapping of electrons in all of the identified shallow traps (Figure 4.26). At room temperature, these electrons can be released to the conduction band or a retrapping process can occur by a trap closer in proximity to the conduction band. This generates a trapping-detrapping process that translates in the lengthening of the persistent luminescence to 8 min ± 2 min as it is shown in the persistent luminescence decay profile (Figure 4.29). Once the electrons reach the conduction band, a nonradiative decay to the 5d orbitals of Eu^{2+} occurs followed by a radiative decay to produce a red persistent emission (Figure 4.26).

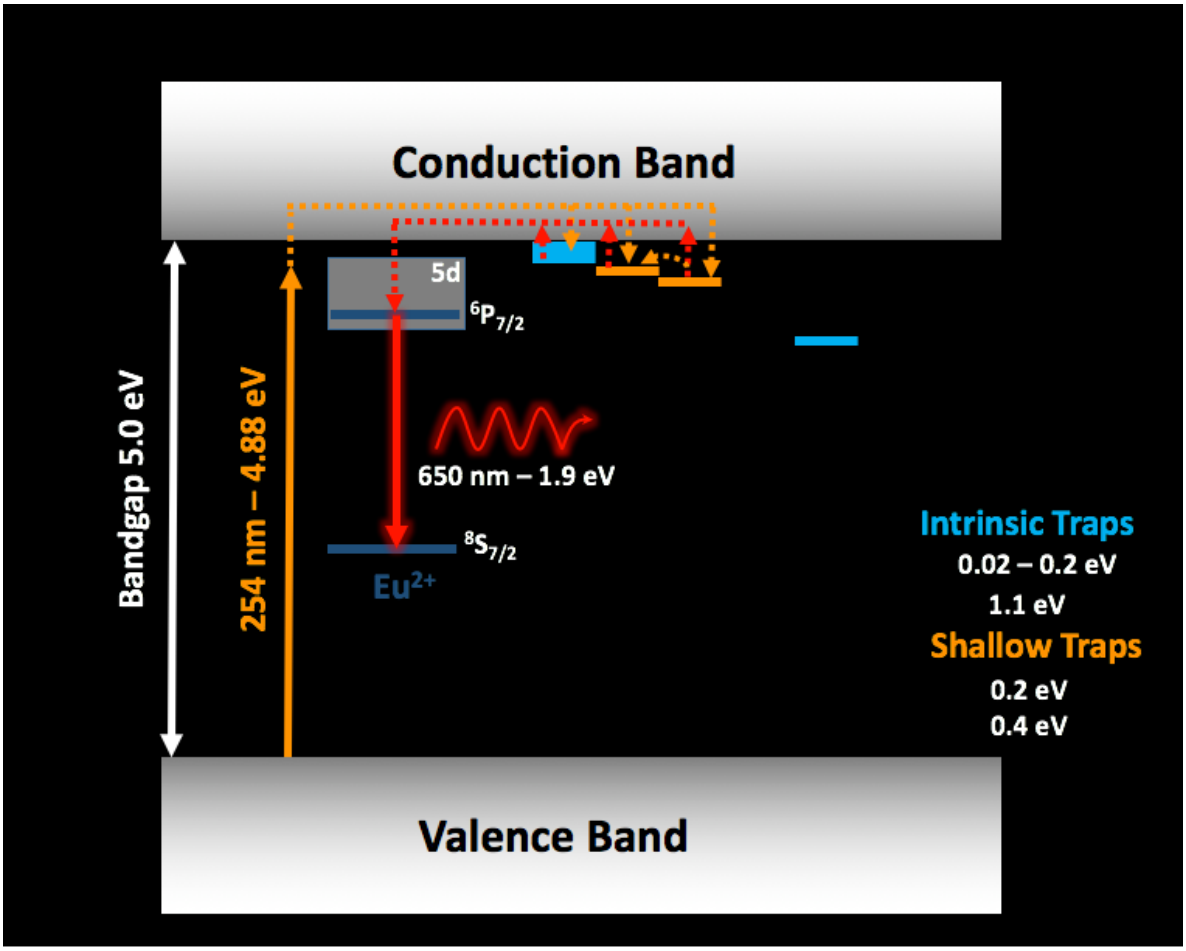

Figure 4.26 Scheme of the electron trapping – de-trapping mechanism for CaS:Eu^{2+} nanophosphors.

4.2.1.3 CaS:Eu^{2+}/Dy^{3+} Nanophosphors

The thermal glow curve for CaS:Eu^{2+} (0.02 mol%)/Dy^{3+} (0.002 mol%) is shown in Figure 4.27A. The thermal glow curve exhibits three thermal peaks at 100, 194 and 305 K that correspond to traps located at 0.2, 0.4 and 0.6 eV below the conduction band, respectively. The shallow traps at 0.2 eV and 0.4 eV correspond to the previously identified traps. The trap at 0.6 eV is formed upon the introduction of Dy^{3+} as a codopant. This third trap is classified as an intermediate trap, which favors the lengthening of the red persistent luminescent time of CaS:Eu^{2+}/Dy^{3+}.

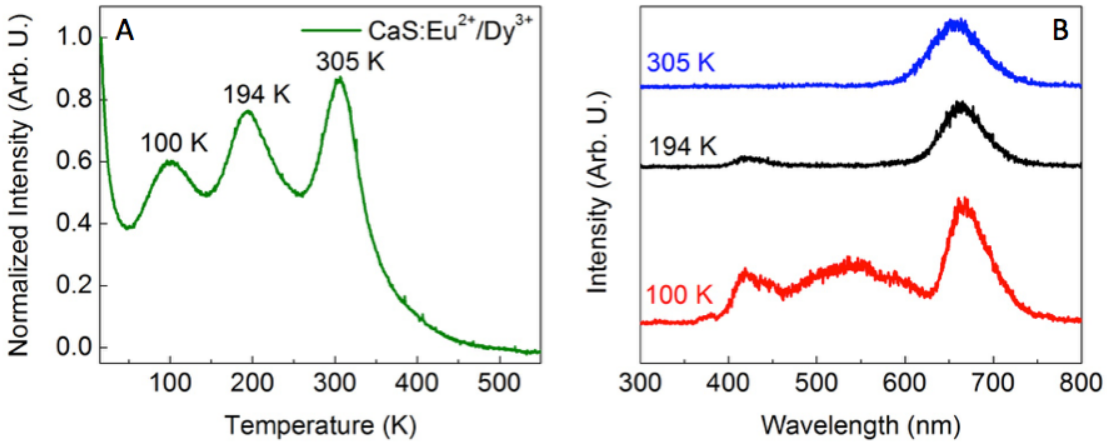

Figure 4.27 (A) Thermal glow curve and (B) thermally stimulated emission spectrum of CaS:Eu^{2+} (0.02 mol%)/Dy^{3+} (0.002 mol%) nanophosphors.

The thermal stimulated emission spectra of CaS:Eu^{2+}/Dy^{3+} nanophosphors is shown in Figure 4.27B. A red emission band with a maximum at 650 nm is attributed to the $4f^6 5d^1$ (T_{2g}) → $4f^7$ ($^8S_{7/2}$) transition of Eu^{2+} and observed for the three temperatures. In addition, at 100 K two broad peaks in the range of 400 to 625 nm are observed. These peaks are attributed to a recombination followed by a radiative process occurring in the intrinsic defects and Dy^{3+} emission centers. Upon 254 nm irradiation of the CaS:Eu^{2+}/Dy^{3+} nanophosphors electrons are promoted from the occupied $4f^7$ levels ($^8S_{7/2}$ ground state) to the conduction band followed by the trapping of electrons in all the identified shallow and intermediate traps (Figure 4.28). The presence of the intermediate trap favors a detrapping-retrapping process over direct release to the conduction band. Electrons trapped in the intermediate trap cannot be released directly to the conduction band,

however, they can be released to and re-trapped by a nearby shallow trap in closer proximity to the conduction band. This process may continue until the electron reaches the conduction band, nonradiative decay to the 5d orbitals of Eu^{2+} and finally a radiative decay to produce a red persistent emission (Figure 4.28). The generation of the shallow trap at 0.6 eV results in the further lengthening of the persistent luminescence time to 300 min ± 15 min (Figure 4.29).

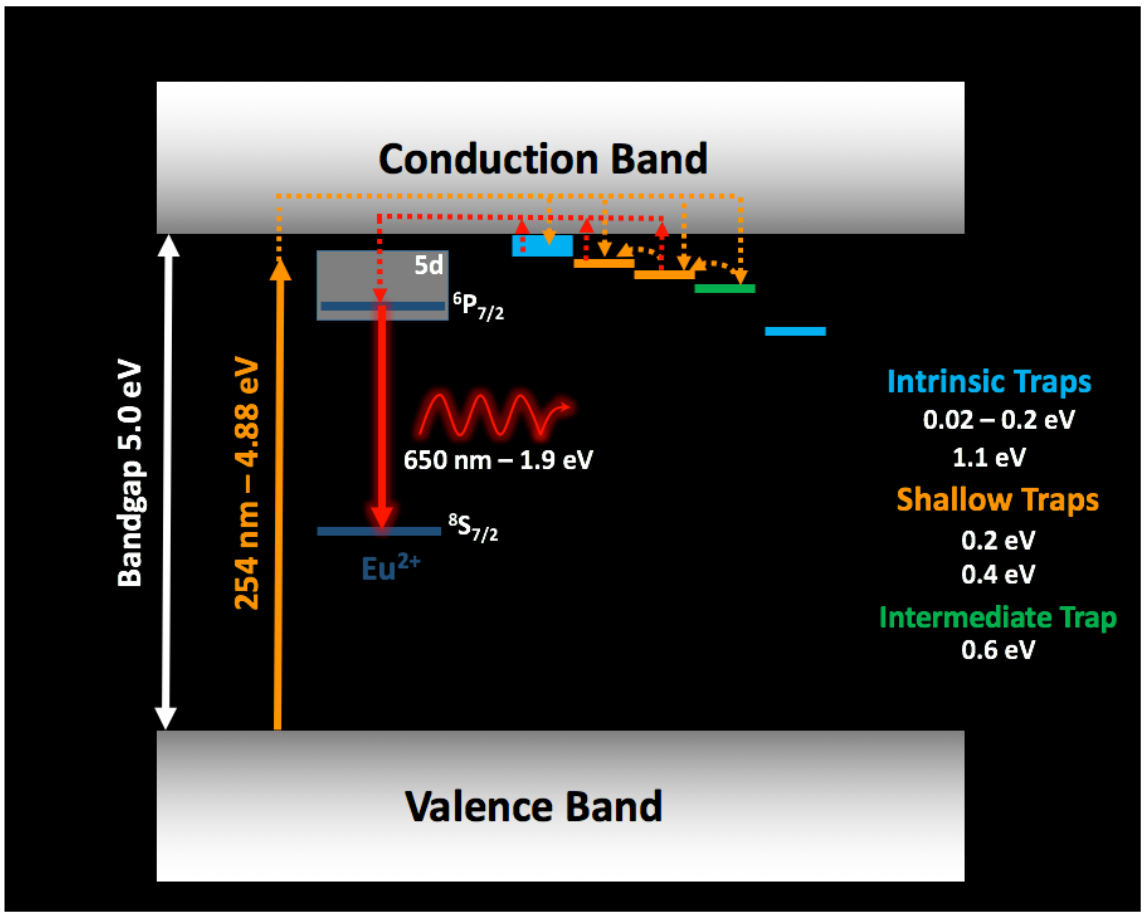

Figure 4.28 Scheme of the electron trapping – de-trapping mechanism for CaS:Eu^{2+}/Dy^{3+} nanophosphors.

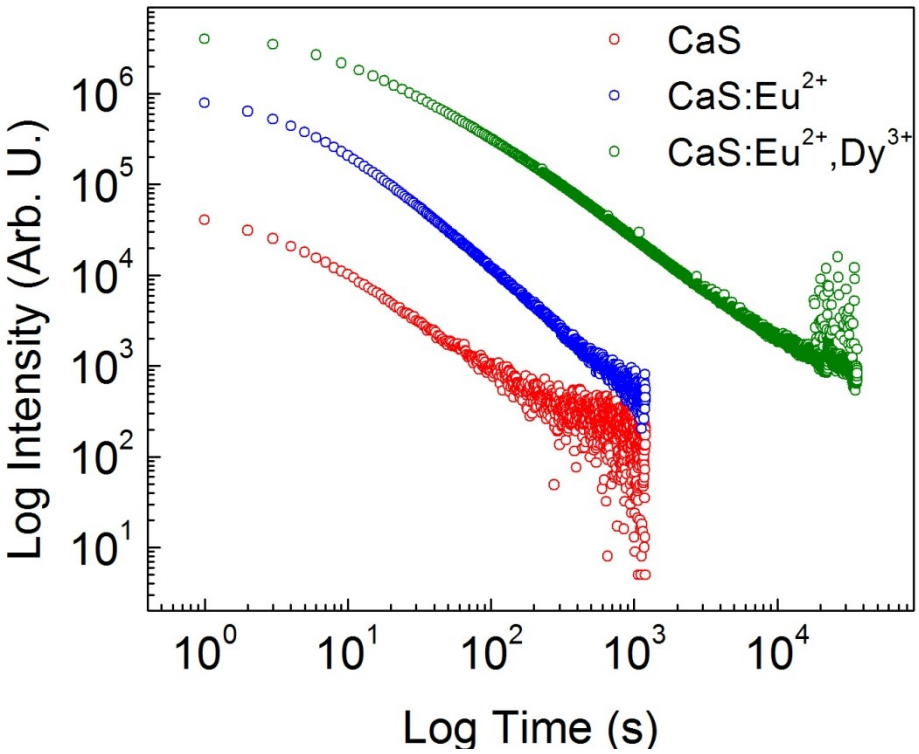

Figure 4.29 Persistent luminescence decay profile for CaS nanoparticles (red dots), CaS:Eu^{2+} (0.02 mol%) (blue dots) and CaS:Eu^{2+} (0.02 mol%)/Dy^{3+} (0.002 mol%) (green dots) nanophosphors.

4.2.2 NIR Photostimulated Luminescence

As shown from the thermal-stimulated luminescence studies, the electrons trapped in the intrinsic traps in CaS and CaS:Eu^{2+} are released at temperatures in the range of 400 K to 650 K, that corresponds to a distribution of deeper traps located in the range 0.8 eV to 1.3 eV below the conduction band. Using light of an appropriate energy may also trigger the detrapping of electron from these deeper traps.

CaS nanoparticles were excited using UV irradiation (254 nm) for 10 minutes and were subsequently placed in the dark until the blue persistent luminescence subsided. Subsequently, the nanoparticles were irradiated using 980 nm light (≈1.3 eV) with a power density of 4000 mW/cm^2. A decrease in intensity of the 486 nm band was observed as a function of time. The blue emission persisted for 7 s ± 2 s and it is known as photostimulated emission. In addition, the power density of the 980 nm irradiation was varied from 4000 mW/cm^2 to 980 mW/cm^2. The photostimulated emission profiles as a

function of the time for the CaS nanoparticles using the maximum and minimum power densities are shown in Figure 4.30, and the photostimulated emission times obtained are shown in Table 4.5.

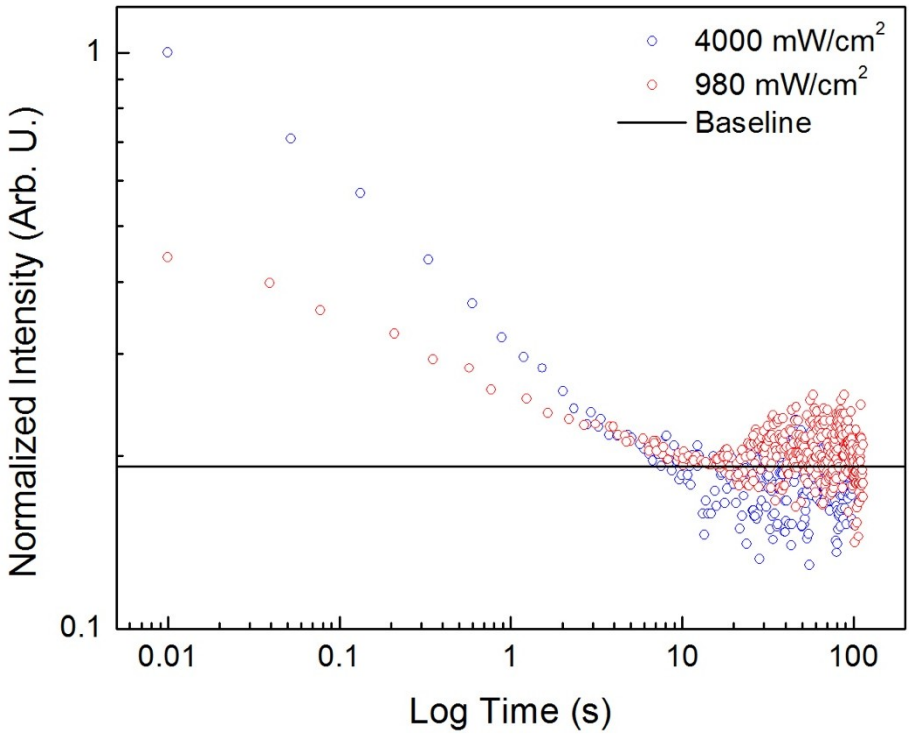

Figure 4.30 NIR Photo-stimulated luminescence decay profile for CaS nanoparticles using a power density of 4000 mW/cm² (red dots) and 980 mW/cm² (blue dots) (λ_{ems} = 486 nm).

Table 4.5 Photostimulated emission times of CaS nanoparticles as a function of the power density using 980 nm excitation.

Power Density (mW/cm²)	Photostimulated Time (s) ± 2 s
4000	7
3300	10
1100	12
980	15

Using the same experimental parameters the NIR photo-stimulation of the 650 nm emission of CaS:Eu^{2+} nanophosphor was evaluated. Using a power density of 4000 mW/cm^2 a photostimulated emission time of 10 s ± 3 s. was obtained. Moreover, the power density of the 980 nm irradiation was varied from 4000 mW/cm^2 to 300 mW/cm^2. The photostimulated emission profiles as a function of time for the CaS:Eu^{2+} nanophosphors using the maximum and minimum power densities are shown in Figure 4.31 and the photostimulated emission times obtained are shown in Table 4.6.

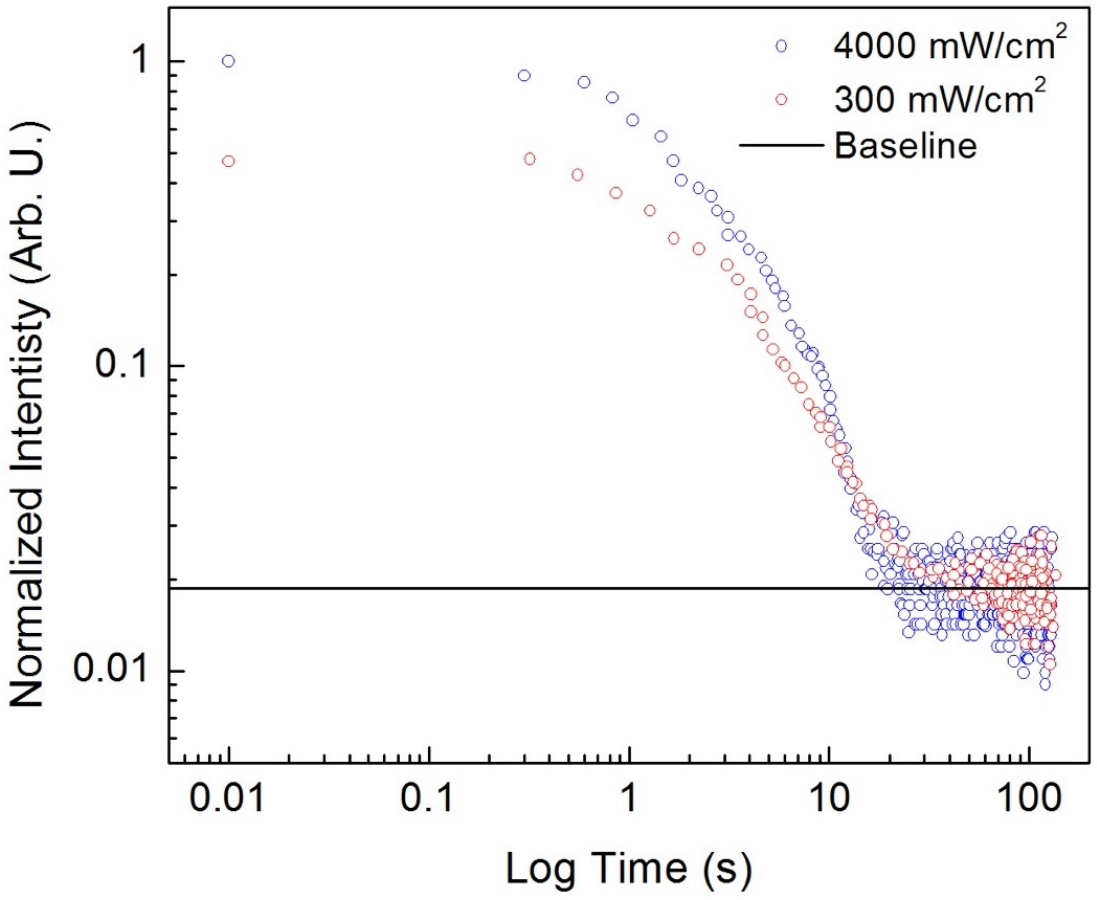

Figure 4.31 NIR Photostimulated luminescence decay profile for CaS:Eu^{2+} nanoparticles using a power density of 4000 mW/cm^2 (red dots) and 300 mW/cm^2 (blue dots) (λ_{ems} = 650 nm).

Table 4.6 Photostimulated emission times of CaS:Eu^{2+} nanophosphors as a function of the power density using 980 nm excitation.

Power Density (mW/cm^2)	Photostimulated Time (s) ± 3 s
4000	10
3300	15
1100	20
400	25
300	30

From the photostimulated experiments carried out on the CaS nanoparticles and the CaS:Eu^{2+} nanophosphors, we observe that, as the power density decreased, the photostimulated emission times are longer. The increase in the photostimulated emission times is attributed to the decrease in the number of photons per area per time, also known as photon flux. This results in less photons impinging on the sample consequently, trapped electrons are released at a lower rate.

Introducing Dy^{3+} ion as a codopant, not only lengthens the time of persistent luminescence by the presence of the intermediate trap, but it could also form deeper traps that are found at approximately 1.3 eV below the conduction band, as it was shown in the VRBE diagram, and that corresponds to an energy excitation of 980 nm. Electrons excited into the conduction band using 254 nm can also be trapped in these deeper traps. At room temperature, the energy provided is not sufficient for the electrons to escape, however 980 nm excitation can promote the release of deeper trapped electrons followed by the Eu^{2+} characteristic red emission at 650 nm. After charging the CaS:Eu^{2+}/Dy^{3+} nanophosphors using 254 nm light, and once the persistent luminescence has subsided, the codoped nanophosphors exhibit a NIR photostimulated red emission. Studies on the NIR photostimulated red emission duration as a function of the power density were carried out and the profiles are shown in Figure 4.32 and the photostimulated emission times are summarized in Table 4.7 As in the case of the CaS nanoparticles and the CaS:Eu^{2+} nanophosphors, as the power density of the 980 irradiation is decreased, the photostimulated emission times exhibited by the CaS:Eu^{2+} /Dy^{3+} increases, confirming the

possibility to control the rate of release of the electrons by tuning the power density of the 980 irradiation.

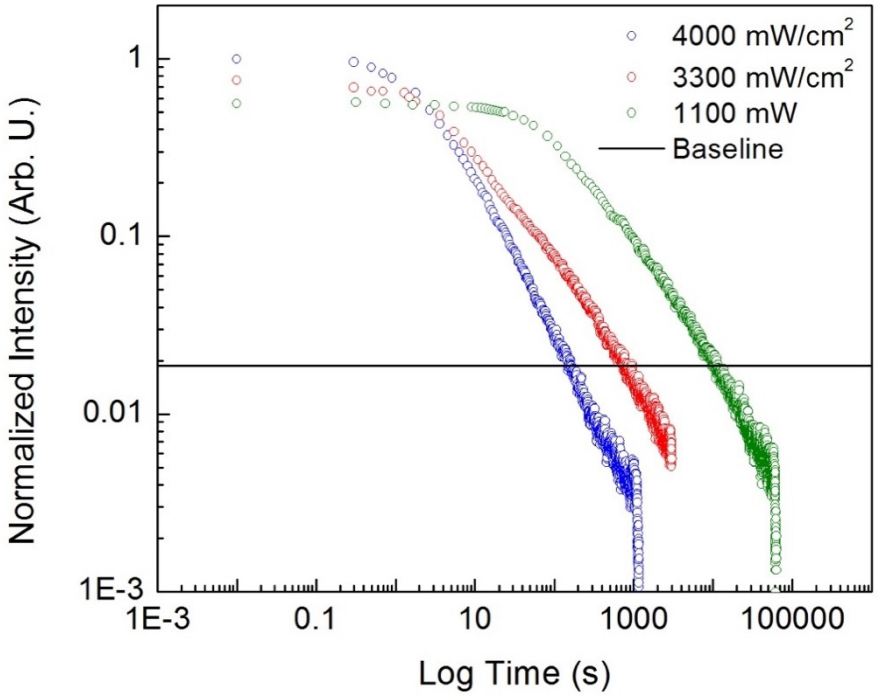

Figure 4.32 NIR Photostimulated luminescence decay profile for CaS:Eu^{2+}/Dy^{3+} nanophosphors as a function of the power density of the 980 nm irradiation (λ_{ems} = 650 nm).

Table 4.7 Photo-stimulated emission times of CaS:Eu^{2+}/Dy^{3+} nanophosphors as a function of the power density using 980 nm excitation.

Power Density (mW/cm^2)	Photostimulated Time (s) ± 60 s
4000	300
3300	500
1100	800
400	900
300	1000
250	1100

Furthermore, the presence of deeper traps was also resolved by measuring the excitation spectrum of the CaS:Eu^{2+}/Dy^{3+} nanophosphors using a Ti-Sapphire laser after charging the sample with UV light and allowing the persistent luminescence to subside. Two bands are observed at 950 nm and 900 nm that are attributed to deeper traps that belong to a distribution of traps located between 1.1 at 1.4 eV below the conduction band (Figure 4.33) formed as consequence of the charge unbalance generated by the intrinsic defects and the introduction of Dy^{3+} as codopant. Conveniently for the use of this nanophosphors in fluorescence optical imaging, NIR excitation can be used to release electrons trapped in this distribution of traps back to the conduction band, non radiatively decaying to the $4f^6 5d^1$ energy levels of Eu^{2+} and finally radiative decay to the $4f^7$ ground state of Eu^{2+} (Figure 4.34). The presence of the deeper traps provides the possibility of releasing the stored energy at any time after the persistent luminescence has subsided.

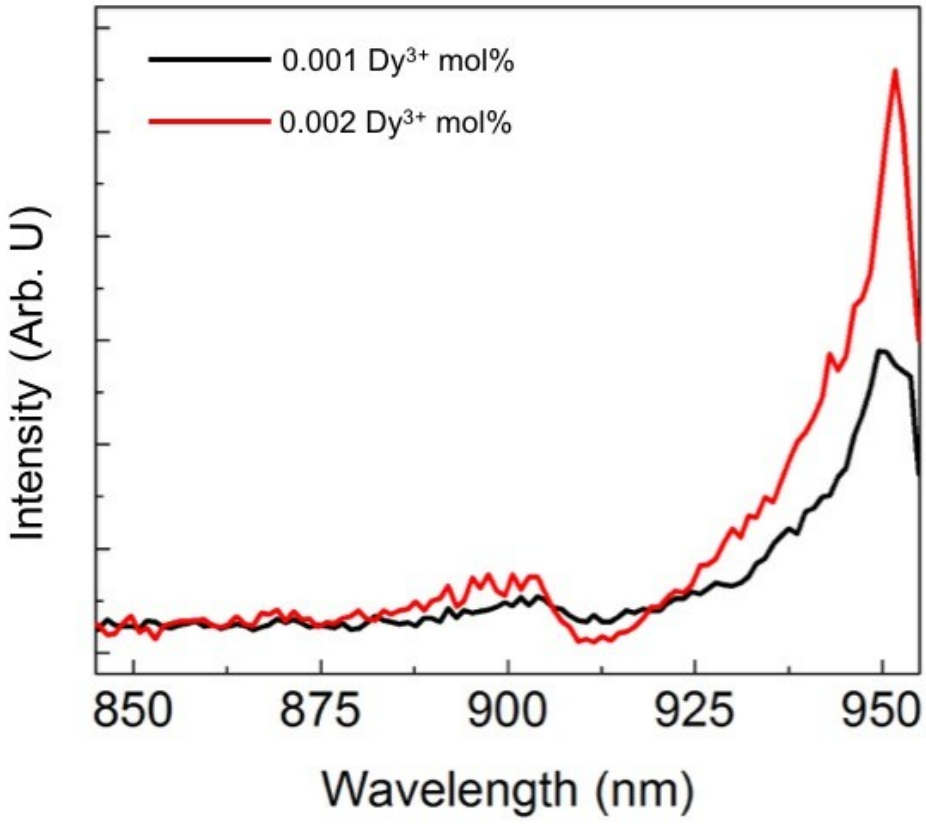

Figure 4.33 Excitation spectra of CaS:Eu^{2+} (0.02 mol%)/Dy^{3+} (X mol%) (λ_{ems} = 650 nm).

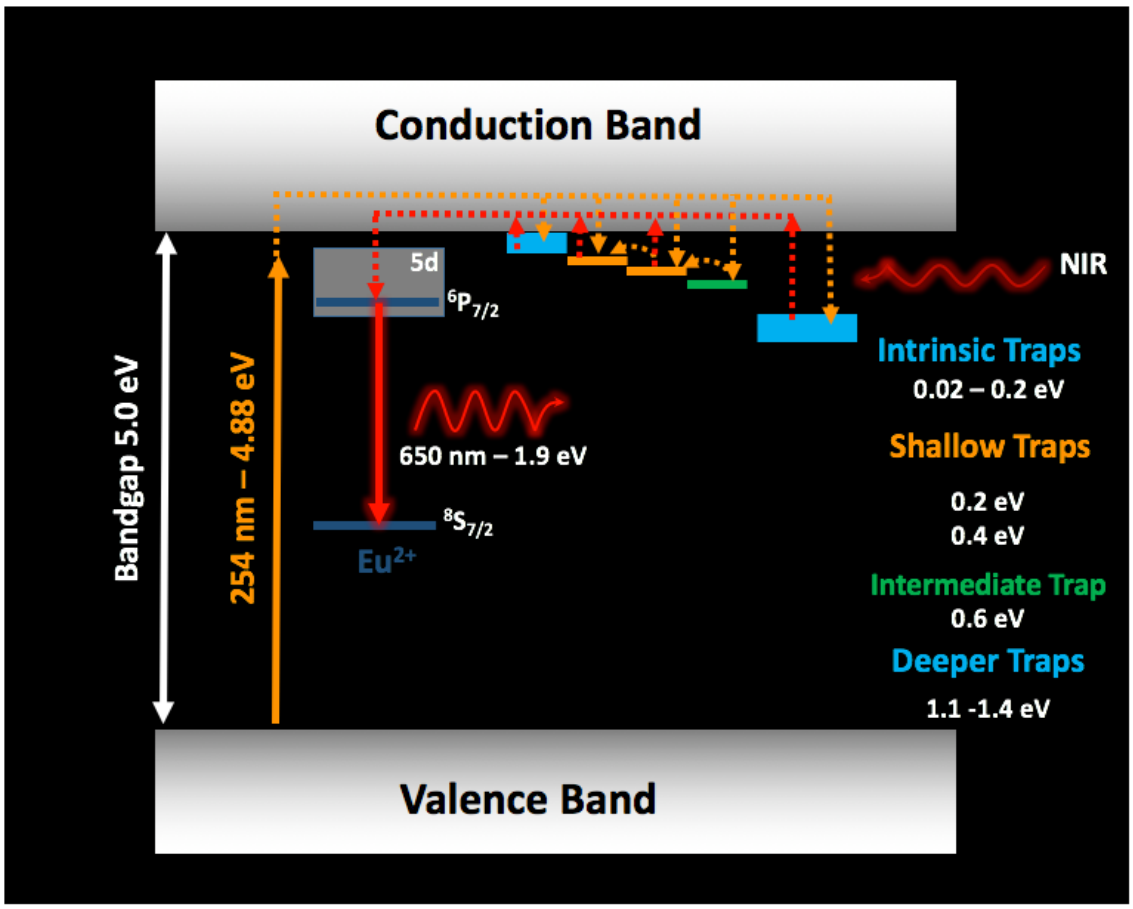

Figure 4.34 Scheme of the electron trapping and detrapping *via* thermal and photo-stimulation for CaS:Eu^{2+}/Dy^{3+}.

4.3 Rendering CaS:Eu^{2+}/Dy^{3+} Nanophosphors Water Dispersible

4.3.1 Surface Modification Strategy I: Conjugation of a Thiol Ligand

Two main drawbacks arise from the requirement of an annealing treatment to obtain CaS:Eu^{2+}/Dy^{3+} nanophosphors: aggregation accompanied by broad size distribution and the rendering of nanocrystals without a capping ligand. The capping ligand is required to produce nanocrystals that are water dispersible and show colloidal stability. Ultrasonication was implemented to minimize the aggregation and the post-synthetic conjugation of 16-mercaptohexadecanoic acid as a capping ligand was proposed to overcome the absence of capping ligand. The high surface energy exhibited by the nanophosphors due to the presence of sulfide dangling bonds could potentially favor the

formation of sulfide-sulfide bonds between the thiol moiety of the capping ligand and the surficial sulfide ions (Figure 4.35).

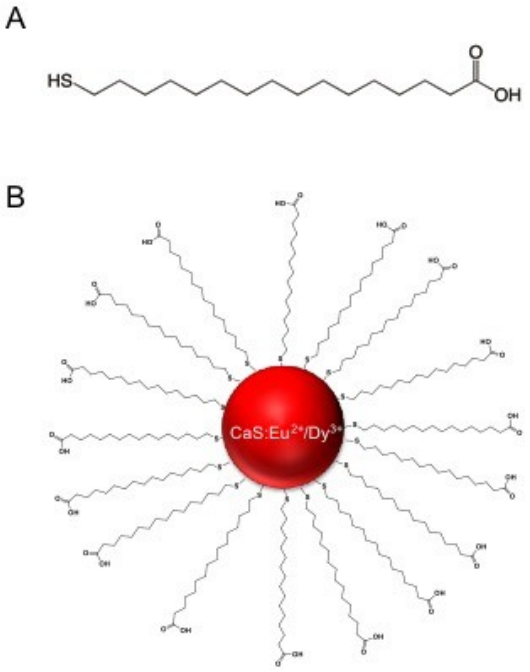

Figure 4.35 (A) Chemical formula of 16-mercaptohexadecanoic acid and (B) graphic representation of the thiolate modified CaS:Eu^{2+}/Dy^{3+} nanophosphor.

The conjugation of the thiol ligand was attempted by dispersing the ultrasonicated nanophosphors and 16-mercaptohexadecanoic acid in methanol. The mixture was left under stirring at 700 rpm and the stirring time was varied from 1 to 7 days. FTIR was used to confirm the presence of the thiolate ligand conjugated to the surface of the CaS:Eu^{2+}/Dy^{3+} nanophosphors obtained after 1 day of reaction and compared with the FTIR spectra of 16-mercaptohexadecanoic acid and the unmodified CaS:Eu^{2+}/Dy^{3+} (Figure 4.35). The FTIR spectrum of 16-mercaptohexadecanoic acid exhibits two peaks at 2926 cm^{-1} and 2853 cm^{-1} that correspond to the asymmetric and symmetric $-CH_2-$ stretching respectively. Furthermore, it exhibits a band at 1710 cm^{-1} and 1465 cm^{-1} that correspond to the C=O stretching vibration and $-CH_2-$ bend vibration. Moreover, a broad week band is observed in the region from 2700 cm^{-1} to 2800 cm^{-1} that corresponds to the –SH stretch. The FTIR spectrum characteristic of the vacuum dried CaS:Eu^{2+}/Dy^{3+} nanocrystal exhibit two broad bands at 1240 cm^{-1} and 650 cm^{-1}. The thiolate modified CaS:Eu^{2+}/Dy^{3+} shows the

vibrational frequencies characteristic of the CaS:Eu^{2+}/Dy^{3+} nanophosphors as well the corresponding –CH_2– symmetric and asymmetric stretching and –CH_2– band of the alkane chain. The band of the C=O stretch vibration is also present whereas the broad band of the –SH stretching is absent. This provides preliminary insights of the possible formation of a S-S bond. The FTIR spectra of the surface modified nanophosphors obtained after the different reaction times show the same distinct features.

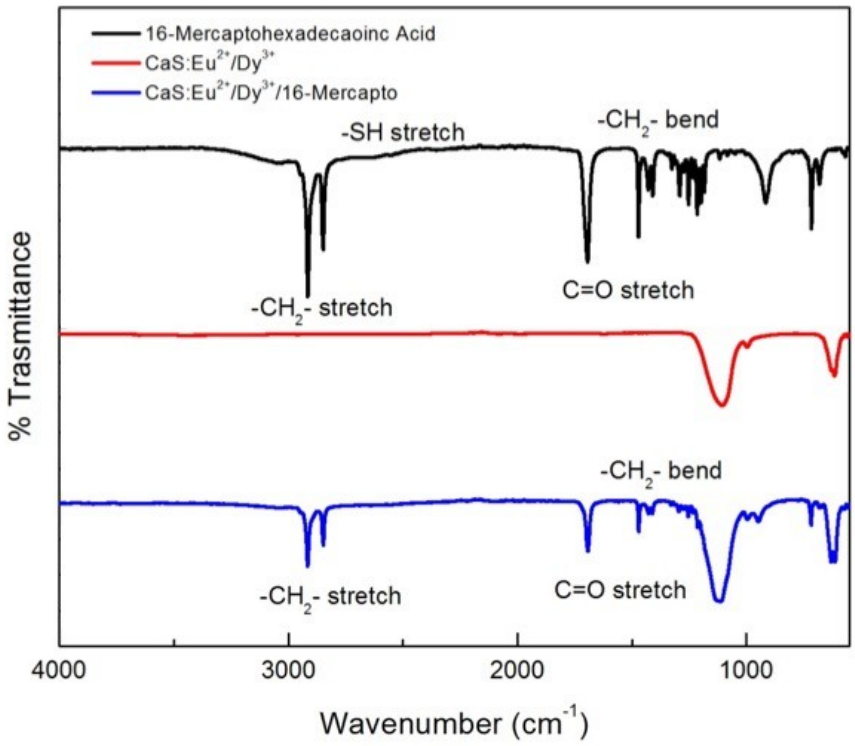

Figure 4.36 FTIR spectra of (black) 16-mercaptohexadecanoic acid, (red) CaS:Eu^{2+}/Dy^{3+} and (blue) CaS:Eu^{2+}/Dy^{3+}/16-mercapto nanophosphors obtained after 1 day of reaction.

The emission spectrum of the CaS:Eu^{2+}/Dy^{3+}/16-mercaptohexadecanoic acid nanophosphors in the solid state was measured upon 254 nm irradiation and compared with the unmodified CaS:Eu^{2+}/Dy^{3+} nanophosphors (Figure 4.37). Both spectra exhibit the red emission broad band with a maximum at 650 nm corresponds to the $4f^6 5d^1 \rightarrow 4f^7$ transition of Eu^{2+} and the broad band in the blue region at 486 nm that corresponds to the emission from the intrinsic defects. No significant differences in the shape and band position are observed when comparing both spectra. The difference in intensity is

attributed to a lower number of CaS:Eu^{2+}/Dy^{3+}/16-mercaptohexadecanoic acid nanophosphors in the measured sample in comparison to the unmodified CaS:$Eu^{2+}Dy^{3+}$ nanophosphors.

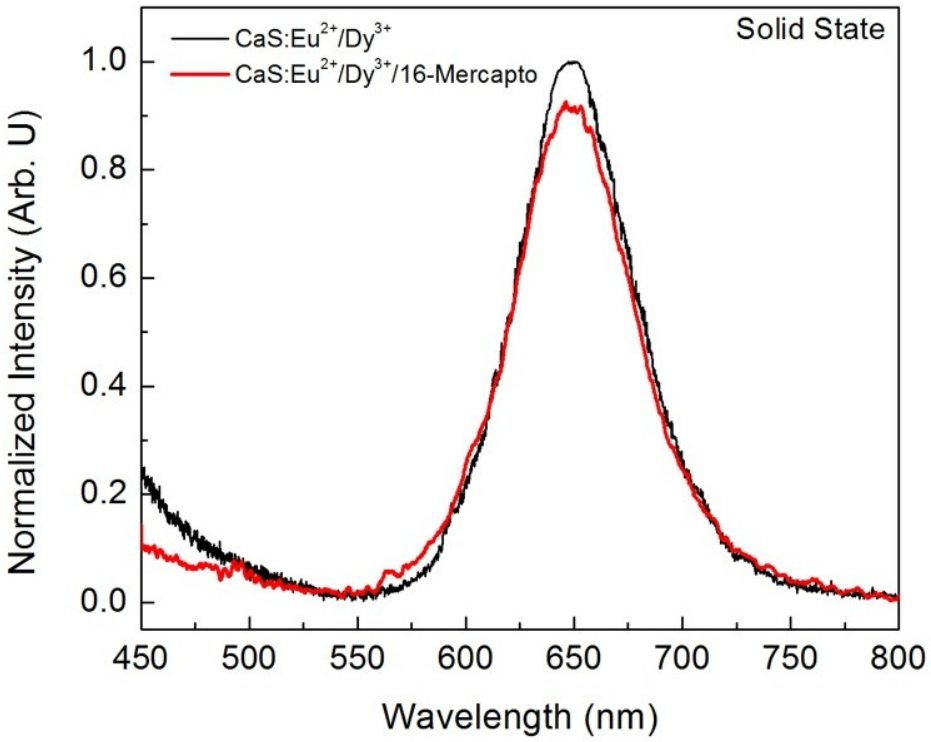

Figure 4.37 Emission spectra of (black) CaS:Eu^{2+}/Dy^{3+} and (red) CaS:Eu^{2+}/Dy^{3+}/16-mercapto nanophosphors (λ_{exc} = 254 nm).

The persistent luminescent properties of the CaS:Eu^{2+}/Dy^{3+}/16-mercaptohexadecanoic acid nanoparticles obtained at the different reaction times were evaluated in the solid state (1 mg) using a persistent luminescence imaging set up. Unmodified CaS:Eu^{2+}/Dy^{3+} nanophosphors in solid state were used as the control sample. In Figure 4.38 the persistent luminescence images as a function of the reaction time are shown. The images were acquired 25 minutes after UV irradiation using no external excitation. It can be observed that as the reaction time is increased, the area exhibiting persistent luminescence from the CaS:Eu^{2+}/Dy^{3+}/16-mercaptohexadecanoic acid nanophosphors is significantly smaller in comparison to that exhibited by the unmodified CaS:Eu^{2+}/Dy^{3+} nanophosphors. Thus, as the reaction time is increased the duration of the persistent luminescence is considerably decreased.

Moreover, the NIR photo-stimulated red luminescence of the CaS:Eu^{2+}/Dy^{3+}/16-mercaptohexadecanoic acid nanophosphors obtained after 1 day of reaction was evaluated by using 980 nm irradiation with a power density of 4000 mW/cm^2. The NIR photo-stimulated luminescence decay is shown in Figure 4.39. A NIR photo-stimulated luminescence duration of 30 s ± 5 s was obtained. The total duration of this luminescent process is reduced by a 90% in comparison to the NIR photo-stimulated luminescence exhibited by the unmodified CaS:Eu^{2+}/Dy^{3+} nanophosphors (See Table 4.7).

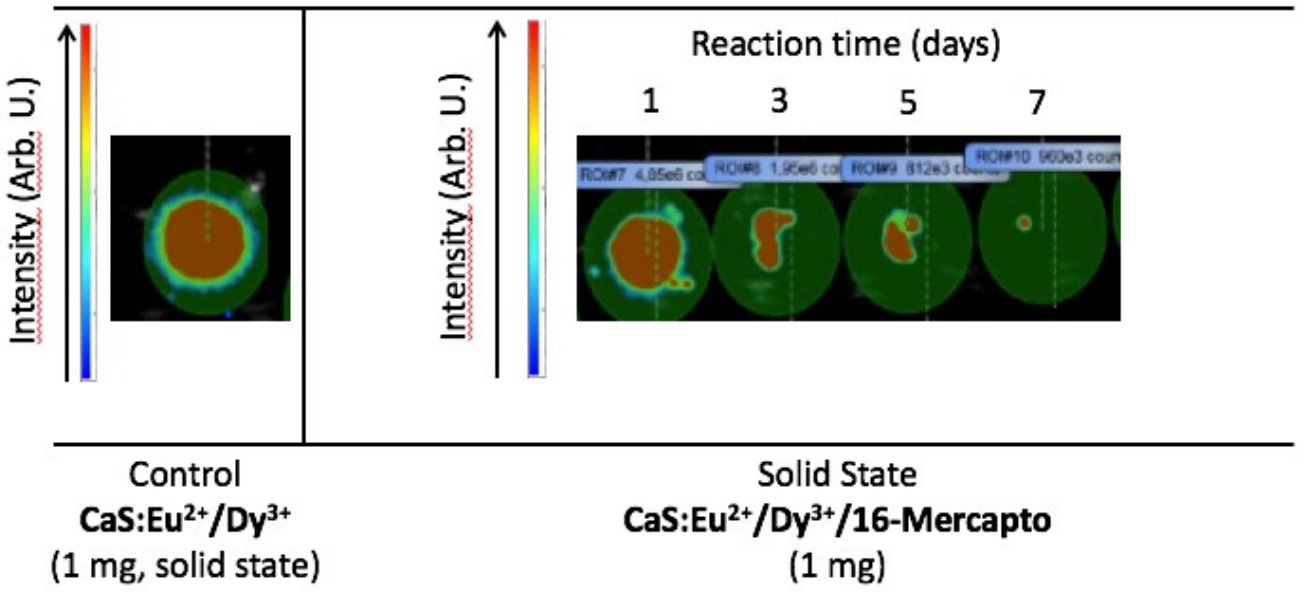

Figure 4.38 Imaging of the persistent luminescence exhibited by CaS:Eu^{2+}/Dy^{3+}/16-Mercapto as a function of the reaction time. Images acquired after 25 minutes of irradiation with 254 nm light.

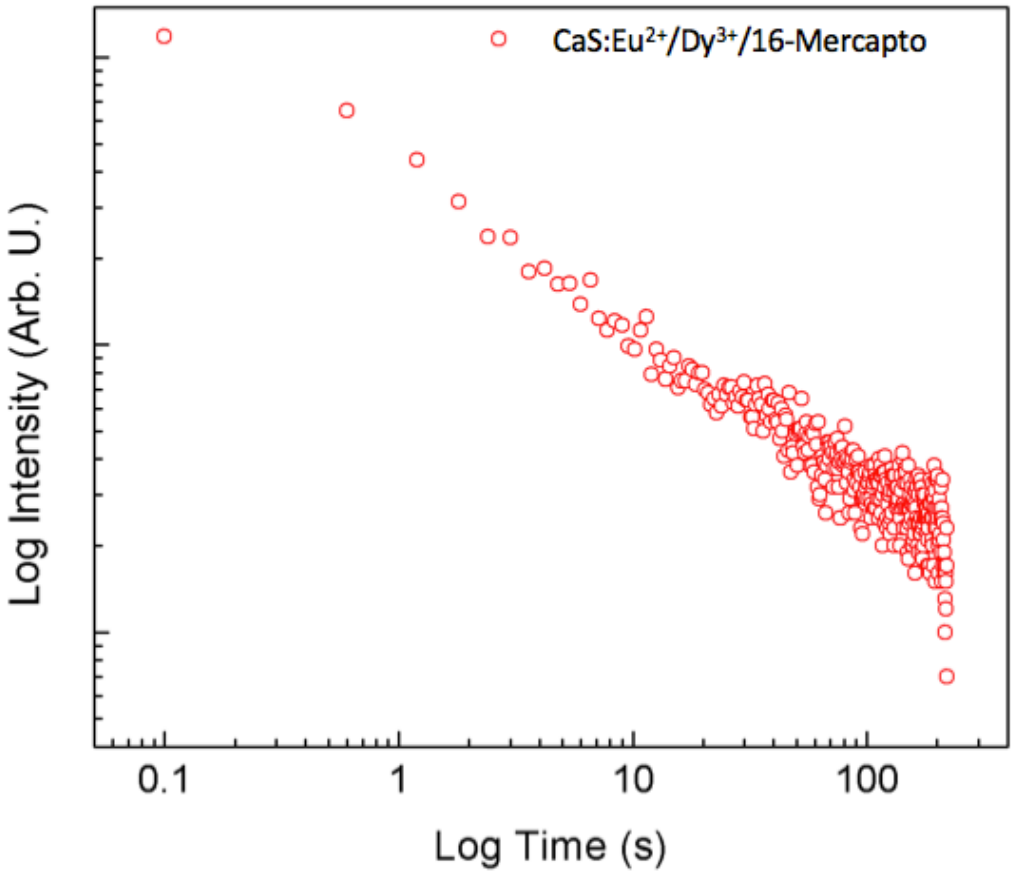

Figure 4.39 NIR Photostimulated luminescence decay profile for CaS:Eu^{2+}/Dy^{3+}/16-mercapto nanophosphors using 980 nm irradiation and a power density of 4000 mW cm^{-2} (λ_{ems} = 650 nm).

The results of the persistent luminescence imaging and NIR-photo-stimulated luminescence decay led to hypothesize that the conjugation of the thiol ligand affects the optical properties of the CaS:Eu^{2+}/Dy^{3+} nanophosphors. We postulated that the thiolate ligand could potentially bond to the surficial sulfide dangling bonds forming sulfide-sulfide bonds. However, the presence of sulfur vacancies in the surface of the nanophosphor can lead to occupancy of the vacancy by the thiolate ligand. As consequence, decreasing the number of trapping sites, which translates in short persistent and photo-stimulated emissions duration times (Figure 4.40). The significant effect on the optical properties by the conjugation of a thiolate ligand on the surface of the CaS:Eu^{2+}/Dy^{3+} was the main reason to propose a different surface modification strategy.

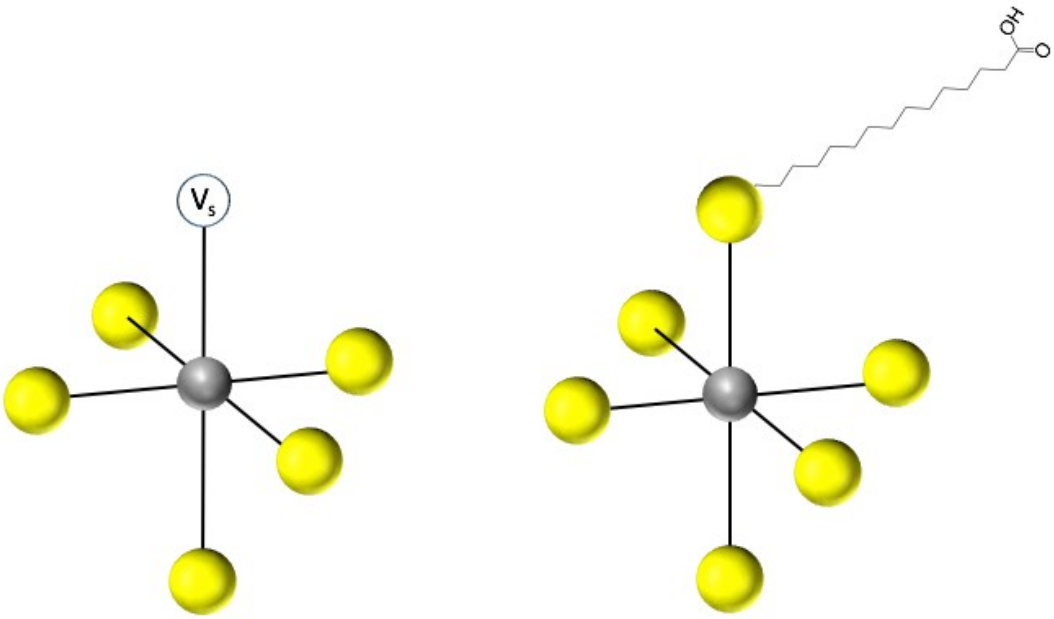

Figure 4.40 Thiolate ligand fills the sulfur vacancy eliminating an electron trapping site.

4.3.2 Surface Modification Strategy II: Polymer Encapsulation and Grafting of a Silica Shell

4.3.2.1 Adsorption of Poly(vinylpyrrolidone)

Polymer encapsulation of nanoparticles has become a commonly used alternative to provide colloidal stability and prevention of aggregation processes.[130] It involves the coating of nanoparticles with amphiphilic polymers through an adsorption process.[131] Poly(vinylpyrrolidone) is an amphiphilic non-ionic polymer that adsorbs readily to broad range of different types of nanomaterials such as metallic nanoparticles, quantum dots, iron oxide and lanthanide based upconverting nanoparticles.[132] Its amphiphilic character arises from the polar amide group within the pyrrolidone ring and the apolar methylene and methane groups in the ring and its carbon backbone chain (Figure 4.41A).[133] When the CaS:Eu^{2+}/Dy^{3+} nanophosphors are dispersed in a polar medium such as ethanol, the hydrophobic portion is adsorbed on the nanoparticles surface leaving the hydrophilic portion exposed to the polar medium (Figure 4.41B).

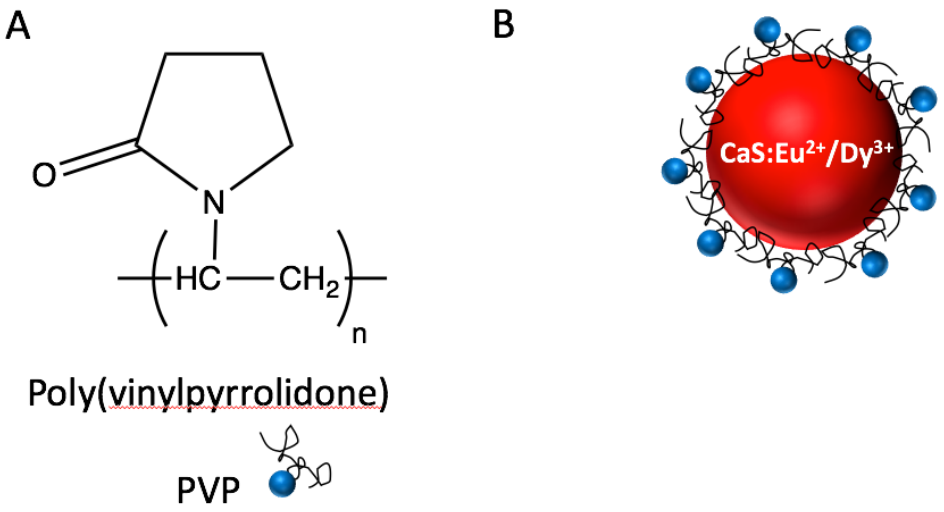

Figure 4.41 (A) Chemical formula of Poly(vinylpyrrolidone) and (B) graphic representation of the PVP polymer adsorbed on the surface of the CaS:Eu^{2+}/Dy^{3+} nanophosphor.

Poly(vinylpyrrolidone) (M_w=10000) (PVP-10) was chosen as the amphiphilic polymer stabilizer to be adsorbed on the surface of CaS:Eu^{2+}/Dy^{3+} after the ultrasonication process in order to provide the nanophosphor colloidal stability in a polar medium as well to prevent further aggregation due to the repulsion between the polar amide groups. To carry out the adsorption of the amphiphilic polymer, the CaS:Eu^{2+}/Dy^{3+} nanophosphors and PVP-10 are dispersed in ethanol and left under stirring at 700 rpm for 24 hours. The PVP-CaS:Eu^{2+}/Dy^{3+} nanophosphors are precipitated *via* centrifugation and washed several times to remove all the non-adsorbed amphiphilic polymer. FTIR was used to confirm the presence of PVP-10 adsorbed to the surface of the CaS:Eu^{2+}/Dy^{3+} nanophosphors. Figure 4.42 shows the FTIR spectra of PVP-10, the unmodified CaS:Eu^{2+}/Dy^{3+} and the PVP-CaS:Eu^{2+}/Dy^{3+} nanophosphors. The FTIR spectrum of PVP-10 exhibits a broad -OH absorption at 3400 cm^{-1}. The hydrophobic portion of the hydrophobic chain is characterized by the presence of two absorbing peaks at 2928 cm^{-1} and 2855 cm^{-1} that correspond to the asymmetric and symmetric $-CH_2-$ stretching respectively and a peak at 1463 cm^{-1} attributed to the $-CH_2$ bending. The polar portion is represented by the C=O stretching at 1685 cm^{-1} and the –CN stretching and bending of the amide bond at 1402 cm^{-1} and 620 cm^{-1} respectively. The FTIR spectrum of the vacuum dried CaS:Eu^{2+}/Dy^{3+} nanocrystal exhibit the

characteristic vibrations at 1240 cm^{-1} and 650 cm^{-1}. The PVP-CaS:Eu^{2+}/Dy^{3+} nanophosphors show the vibrational frequencies characteristic of CaS:Eu^{2+}/Dy^{3+} nanophosphors and the corresponding hydrophobic backbone vibrations and the hydrophilic vibrations of the C=O stretch vibration and –CN stretching and bending of the PVP-10.

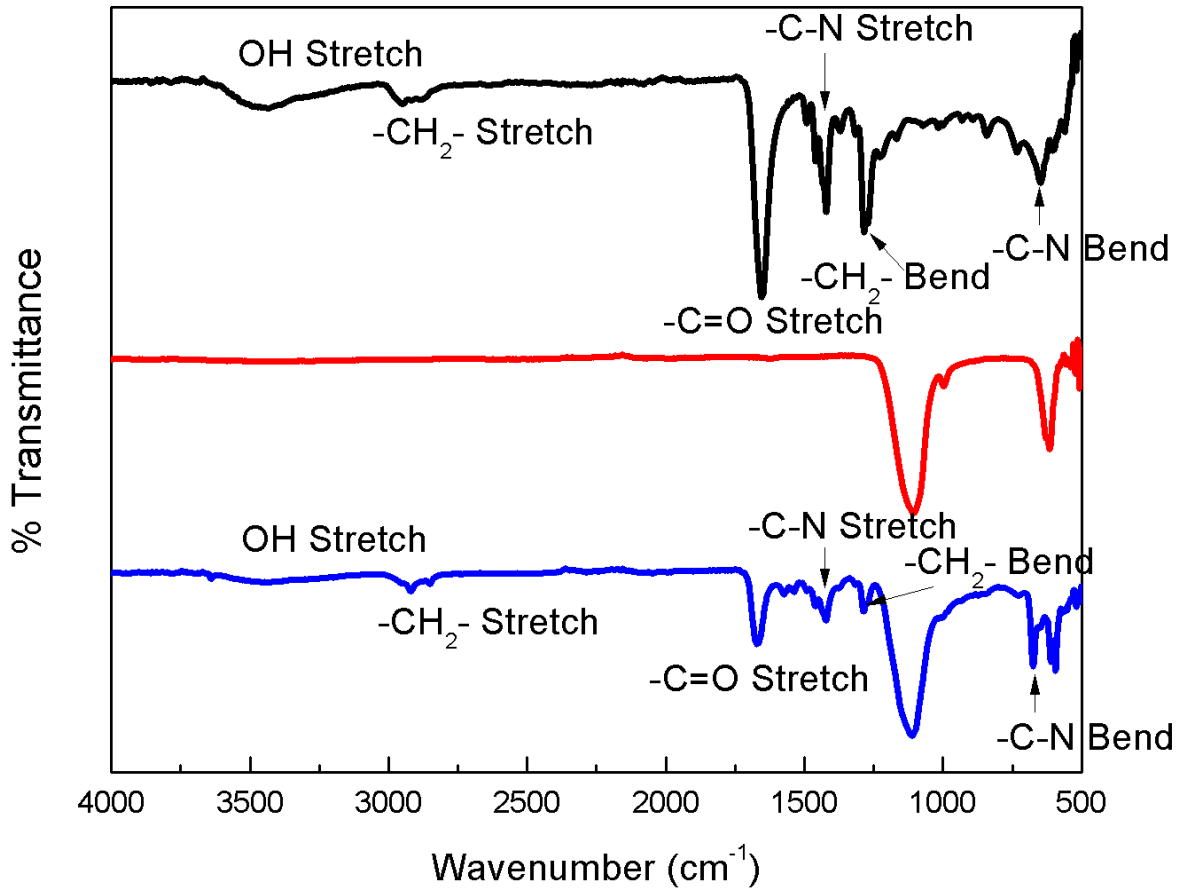

Figure 4.42 FTIR spectra of (black) Poly(vinylpyrrolidone) (M_w=10000), (red) CaS:Eu^{2+}/Dy^{3+} and (blue) PVP- CaS:Eu^{2+}/Dy^{3+} nanophosphors

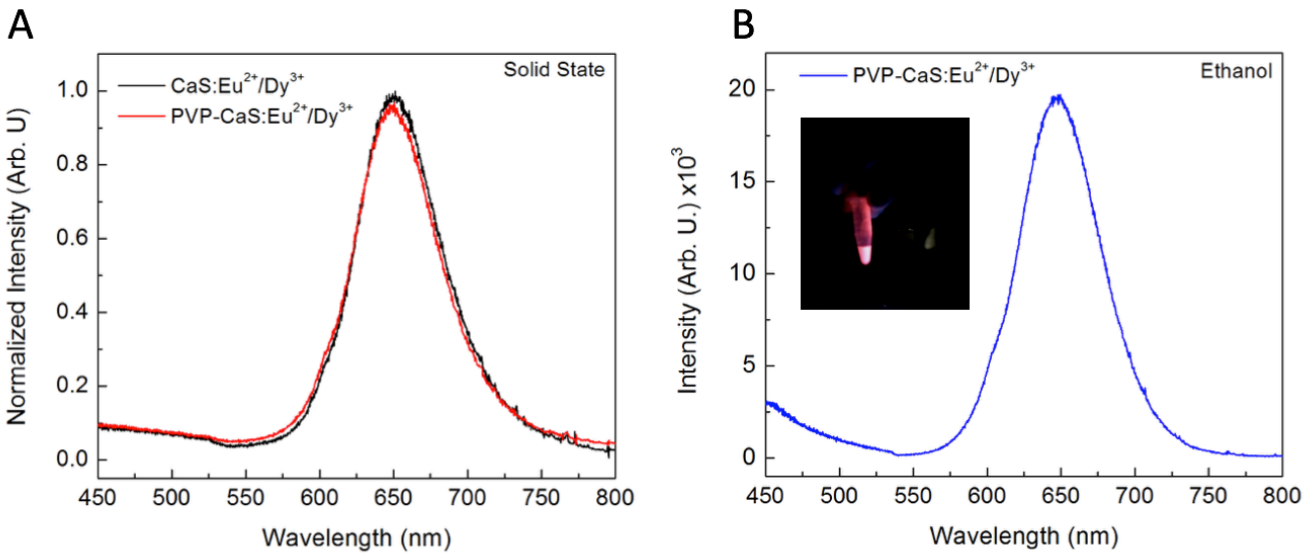

Figure 4.43 (A) Emission spectra of CaS:Eu^{2+}/Dy^{3+} and PVP-CaS:Eu^{2+}/Dy^{3+} nanophosphors in solid state upon 254 nm excitation. (B) Emission spectrum and picture of PVP-CaS:Eu^{2+}/Dy^{3+} nanophosphors dispersed in ethanol (1 mg/mL) upon 254 nm excitation.

The luminescence properties of the PVP-CaS:Eu^{2+}/Dy^{3+} were measured upon 254 nm excitation. Figure 4.43A shows the emission spectra of the CaS:Eu^{2+}/Dy^{3+} and the PVP-CaS:Eu^{2+}/Dy^{3+} nanophosphors in solid state. Both spectra exhibit the characteristic red emission broad band with a maximum at 650 nm corresponds to the $4f^6 5d^1 \rightarrow 4f^7$ transition of $Eu^{2+}$and the broad band in the blue region that corresponds to the emission from the intrinsic defects. Furthermore, the polymer coated nanophosphors were easily dispersed in ethanol (1 mg/mL) and the emission spectrum was measured using upon 254 nm irradiation (Figure 4.43B). No significant changes in the optical properties were observed thus, the adsorption of the amphiphilic PVP polymer does not affect the Eu^{2+} luminescent centres.

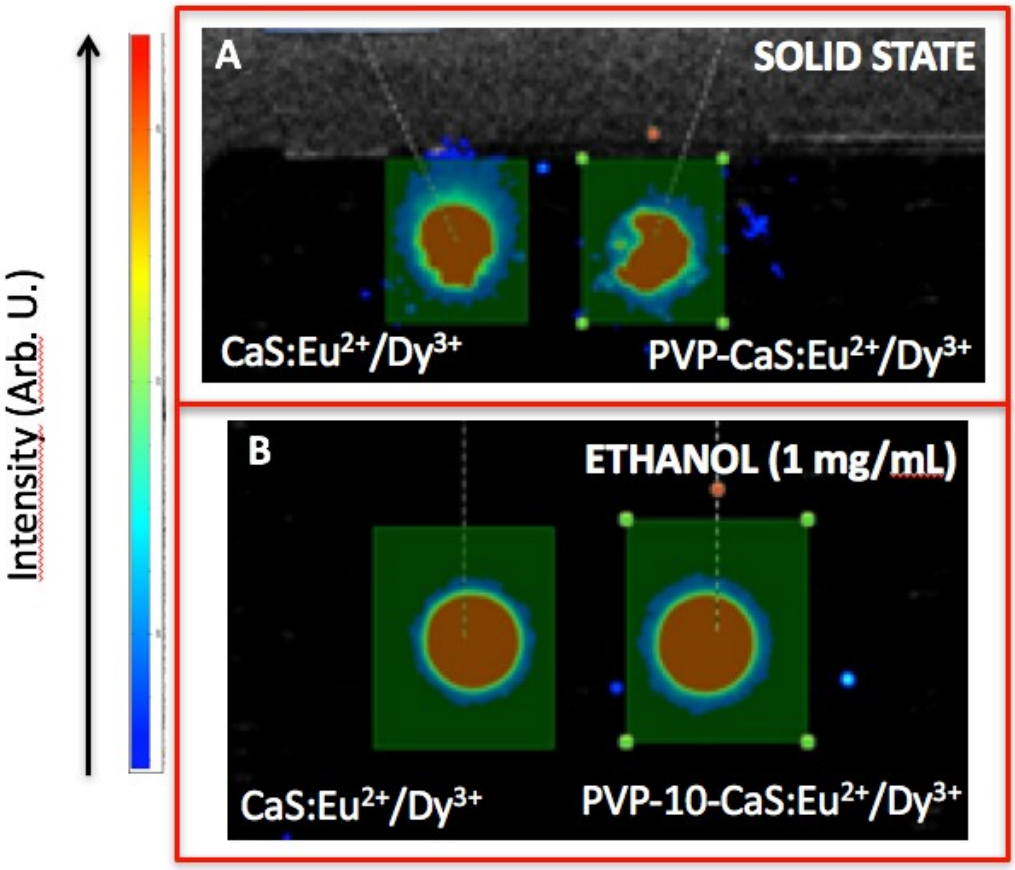

Figure 4.44 Imaging of the persistent luminescence exhibited by CaS:Eu^{2+}/Dy^{3+} and PVP- CaS:Eu^{2+}/Dy^{3+} nanophosphors in (A) solid state (1 mg) and (B) dispersed in ethanol (1 mg/mL). Images acquired under no excitation 30 min after being charging process with 254 nm light.

The persistent luminescent properties of the PVP-CaS:Eu^{2+}/Dy^{3+} nanophosphors were evaluated in solid state (1 mg) and dispersed in ethanol (1 mg/mL) using a persistent luminescence imaging set up (Figure 4.44). Unmodified CaS:Eu^{2+}/Dy^{3+} nanophosphors and polymer coated PVP- CaS:Eu^{2+}/Dy^{3+} nanophosphors in solid state were charged using 254 nm irradiation. The persistent luminescence red emission of both nanophosphors was imaged 30 minutes after the irradiation was terminated (Figure 4.44A). Both samples exhibit similar intensity indicating similar persistent luminescence decay profiles.

Furthermore, once the red persistent luminescence subsided, both samples were dispersed in ethanol and re-charged using 254 nm irradiation. The dispersed nanophosphors in the polar solvent exhibit similar intensities in the red persistent luminescence as it is confirmed by the images acquired after 30 minutes in the absence of

external excitation (Figure 4.44B). The similarity in the intensity observed on the solid state and in dispersion lead to postulate that the adsorption of the PVP polymer in the surface does not have an effect in the shallow and intermediate traps responsible of the red persistent luminescence.

Moreover, the NIR photo-stimulated properties of the PVP-CaS:Eu^{2+}/Dy^{3+} nanophosphors in solid state were evaluated using the same experimental parameters reported for the CaS:Eu^{2+}/Dy^{3+} nanophosphors. The polymer coated nanophosphors exhibits a NIR photo-stimulated red emission with a duration of 250 s ± 60 s at the maximum power density of 4000 mW/cm^2 (Figure 4.45). A study of the NIR photo-stimulated time as a function of the power density was also undertaken and the results are shown in Table 4.8. The photo-stimulated emission times measured are in the same range of the values obtained for the unmodified CaS:Eu^{2+}/Dy^{3+} nanophosphors. Thus, the adsorption of the PVP polymer on the surface does not have an effect in deeper traps present in the nano-sized red persistent luminescent CaS:Eu^{2+}/Dy^{3+}.

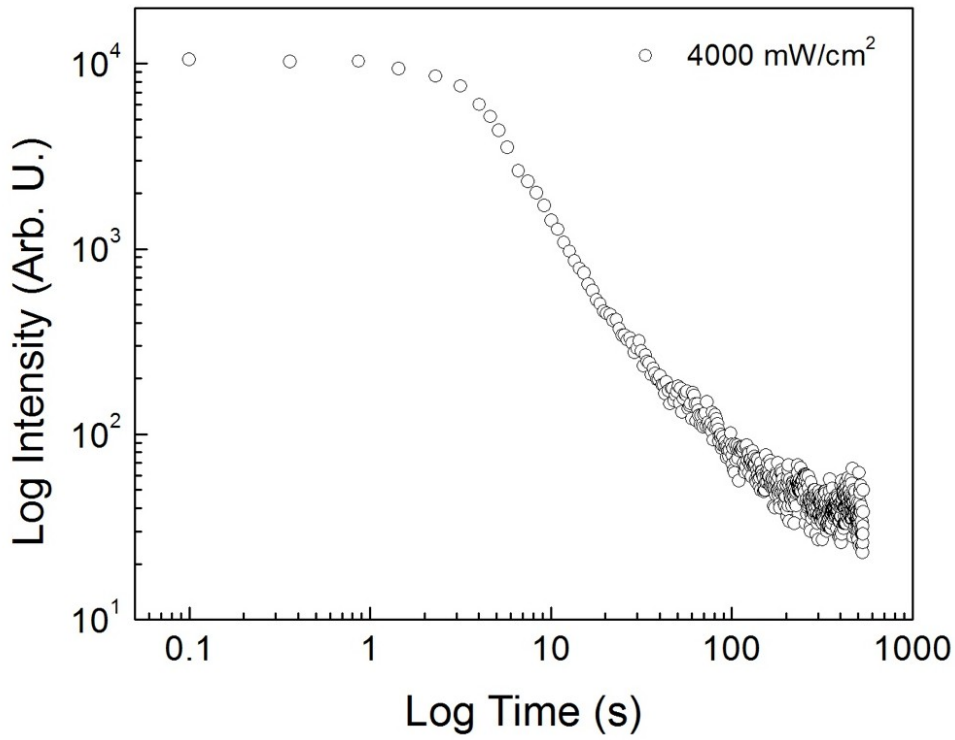

Figure 4.45 NIR Photostimulated luminescence decay profile for PVP-CaS:Eu^{2+}/Dy^{3} nanophosphors using 980 nm irradiation and a power density of 4000 mW cm^{-2} (λ_{ems} = 650 nm).

Table 4.8 NIR photo-stimulated emission times of CaS:Eu^{2+}/Dy^{3+} and PVP- CaS:Eu^{2+}/Dy^{3+} nanophosphors as a function of the power density using 980 nm excitation.

Power Density (mW/cm^2)	CaS:Eu^{2+}/Dy^{3+} Photostimulated Time (s) ± 60 s	PVP-CaS:Eu^{2+}/Dy^{3+} Photostimulated Time (s) ± 60 s
4000	300	250
3300	500	480
1100	800	740
400	900	850
300	1000	980
250	1100	1080

4.3.2.2 Grafting of a Silica Shell

Grafting of a silica shell on the surface of nano-sized materials is one of the surface modification methods used to achieve water dispersibility, colloidal stability and facilitate

the decoration of the surface with ligands of biological interest by taking advantage of the surficial Si-OH moieties.

The formation of silica micro-sized particles was first reported by Stöber *et al* in 1968.[134] The authors proposed a method to produce a monodisperse suspension of silica spheres in the size range between 0.05 μm to 2 μm. The method was based on results reported by Kolbe in 1954 that describe the formation of silica particles as consequence of a chemical reaction between tetraalkyl silicate with water in alcoholic medium using a base as a catalyst.[135] Stöber *et al*, found that the formation of silica particles was not always achieved and in most of the cases the synthesis resulted in the formation of a gel like structure. As consequence, the authors carried out a rigours systematic study to determine the experimental conditions to obtain silica particles. The authors found that the reaction of tetraethyl orhtosilicate (TEOS) undergoes trough an hydrolization followed by a condensation reaction in the presence of concentrated ammonium hydroxide as catalyst and ethanol as solvent resulting in the formation of 'sphere-like' silica particles (Figure 4.46).

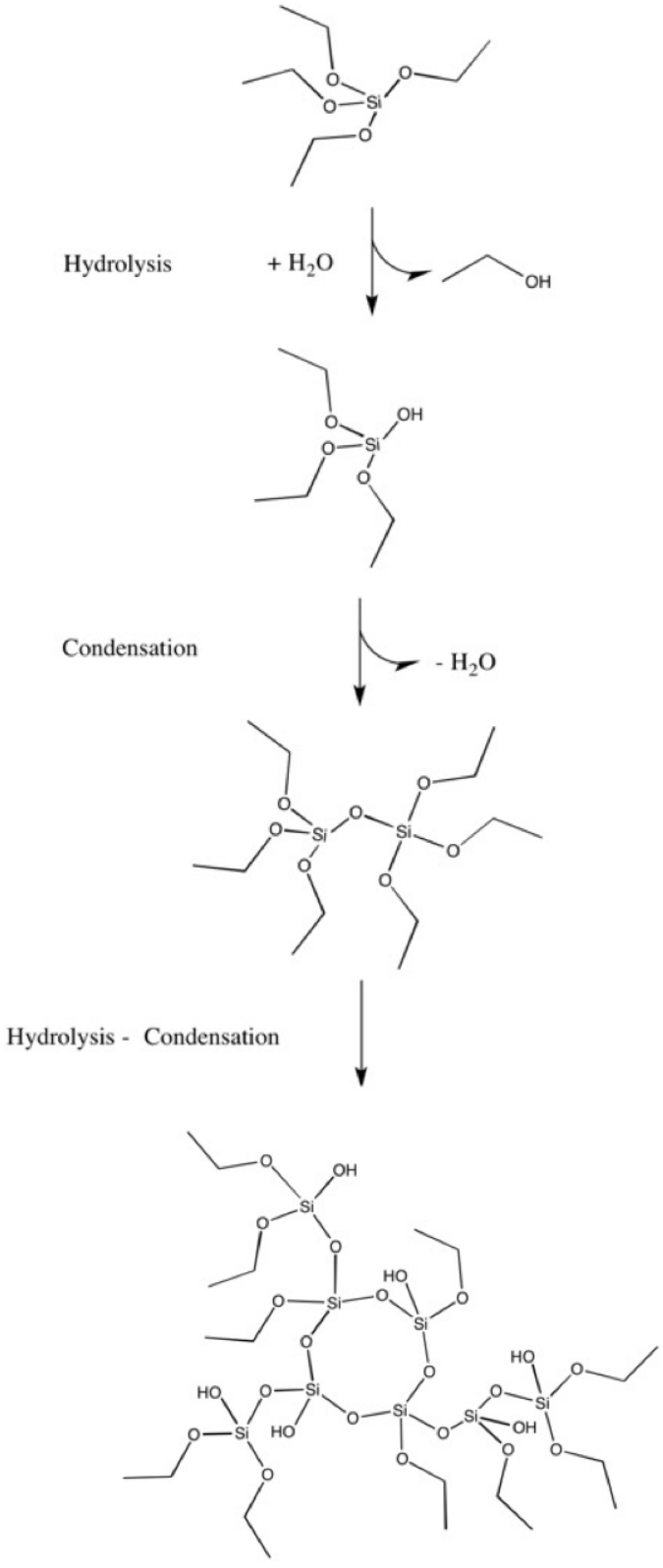

Figure 4.46 Representation of the hydrolysis and condensation of TEOS

The Stöber method has been modified to achieve the formation of a silica shell around the core of different types of nanoparticles,[31, 136] including $CaS:Fe^{2+}$ nanoparticles.[137] Wu *et al*., reported the formation of the silica shell on the surface of $CaS:Fe^{2+}$ nanoparticles using PVP as stabilizing agent and ethanol as the solvent medium. The authors postulate that PVP adsorbs on the surface of $CaS:Fe^{2+}$ nanoparticles forming a polymeric shell that provides stability, prevents aggregation and the hydrophilic part of the of the PVP would act as a nucleation sites for further silica shell growth. The authors reported that after stabilizing the $CaS:Fe^{2+}$ nanoparticles with PVP, the PVP-$CaS:Fe^{2+}$ nanoparticles may be dispersed in ethanol and 1 mL of a solution of ammonium hydroxide is added dropwise to the dispersion. Immediately following this step, 100 μL of TEOS are added and stirred for 24 hours. The nanoparticles are precipitated *via* centrifugation and washed several times with ethanol.

The silica coating procedure reported by Wu *et al.,* was carried out on the PVP-$CaS:Eu^{2+}/Dy^{3+}$ nanophosphors. The products obtained were characterized by TEM and the images are shown in Figure 4.47. TEM results revealed that silica nanoparticles with an average size of 147 nm ± 10 nm main are formed. However, a significantly lower number of TEOS-PVP-$CaS:Eu^{2+}/Dy^{3+}$ nanophosphors were found. This is can be attributed to an incomplete coverage of the surface of the nanophosphor by the PVP polymeric shell. This results in the hydrolysis of the CaS host by the excess of water molecules, that are not involved in the hydrolysis of TEOS, and additionally in the absence of the smaller in size PVP-$CaS:Eu^{2+}/Dy^{3+}$ nanophosphors and a low number of the larger in size PVP-$CaS:Eu^{2+}/Dy^{3+}$ nanophosphors. Moreover, the lower number of cores lost to the hydrolysis reaction and the excess of TEOS favours the formation of silica nanoparticles.

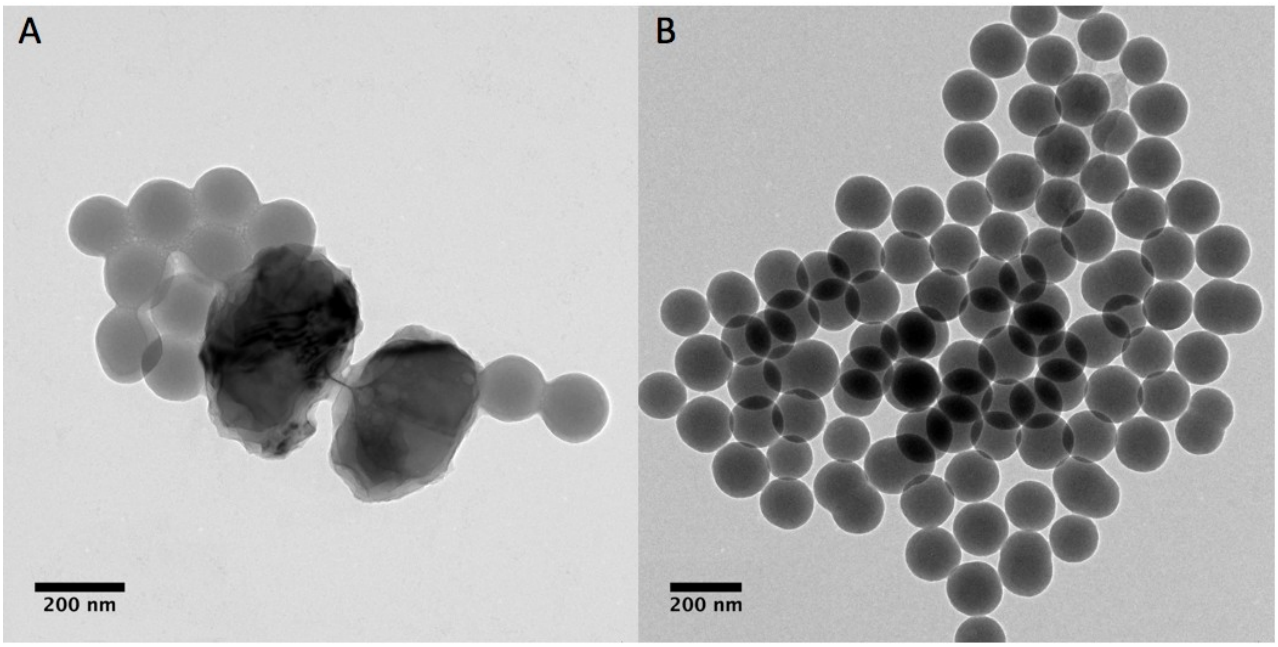

Figure 4.47 TEM images of the obtained products (1 mg/mL in water) following the silica coating procedure reported by Wu *et al*. (A) TEOS-PVP-CaS:Eu^{2+}/Dy^{3+} nanophosphors and silica nanoparticles and (B) silica nanoparticles (Scale bar: 200 nm).

In order to avoid the hydrolysis of the PVP-CaS:Eu^{2+}/Dy^{3+} nanophosphors, the amount of the aqueous ammonium hydroxide and TEOS was reduced to 50 μL and 5 μL respectively. As well, the aliquots of reactants were added using a constant rate and constant stirring. Figure 4.48 shows the TEM images of the TEOS-PVP-CaS:Eu^{2+}/Dy^{3+} nanophosphors and the corresponding energy-dispersive X-ray spectroscopy (EDS) pattern. Despite that the silica coated nanophosphors obtained do not show an homogeneous coating with a narrow size distribution, the coating procedure followed allowed for formation of a shell around the nanophosphors and minimized the generation of silica nanoparticles. From EDS analysis (Figure 4.48C) Ca, S, O and Si were found on the surface of the TEOS-PVP-CaS:Eu^{2+}/Dy^{3+}, in agreement with the expected composition of the nanophosphors. The concentrations of the Eu and Dy species are below the detection limit of the instrument used.

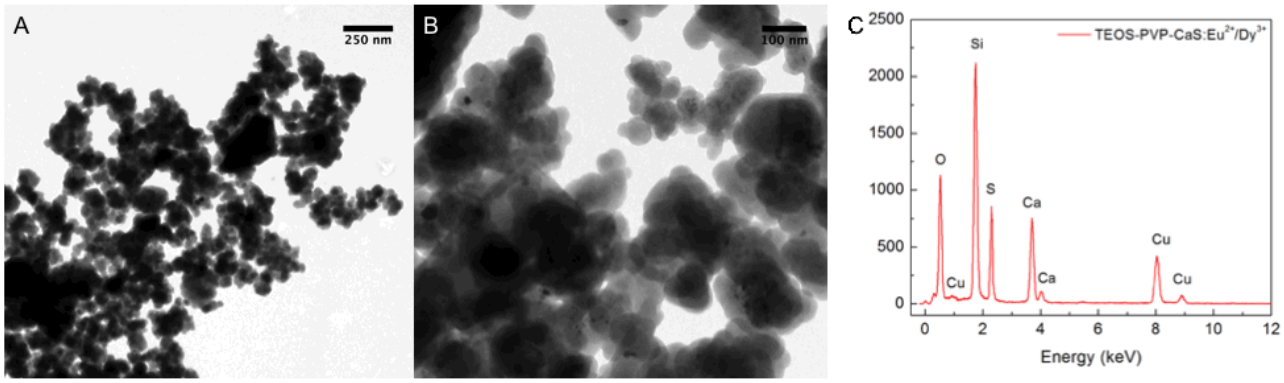

Figure 4.48 TEM images of TEOS-PVP-CaS:Eu^{2+}/Dy^{3+} nanophosphors (1 mg/mL in water) (A) scale bar: 250 nm, (B) scale bar: 100 nm and (C) corresponding EDS pattern taken from region imaged in figure B.

The presence of the silica shell allows for a better dispersion of the nanophosphors in polar solvents such as ethanol and water. The nanophosphors were first dispersed in ethanol 99% and the emission spectrum was measured upon 254 nm irradiation and shown in Figure 4.49. The spectrum exhibits the same characteristic optical properties exhibited by the PVP-CaS:Eu^{2+}/Dy^{3+} . Hence, the grafting of the silica shell on the surface of PVP-CaS:Eu^{2+}/Dy^{3+} nanophosphors does not have an effect on the crystal field splitting of the 5d excited energy levels of Eu^{2+} or in the environment of the intrinsic defects. Furthermore, the emission the emission spectrum (Figure 4.49) of the TEOS-PVP-CaS:Eu^{2+}/Dy^{3+} nanophosphors dispersed in water (0.5 mg/mL) was measured using 254 nm irradiation. As shown in the Figure 4.49 using an aqueous medium does not induce changes in the optical properties of the nanophosphors since no variations in the shape or band positions were found.

In order to compare the intensity of the luminescence of the TEOS-PVP-CaS:Eu^{2+}/Dy^{3+} nanophosphors in the different solvents, the emission spectrum of the nanophosphors in water was normalized with respect to the maximum intensity at 650 nm of the nanophosphors in ethanol. A slight decrease in the intensity is observed for TEOS-PVP-CaS:Eu^{2+}/Dy^{3+} nanophosphors in water. Initially, the same weight (0.5 mg) of nanophosphors was used to prepare the two different solutions. However, uncoated PVP-CaS:Eu^{2+}/Dy^{3+} nanophosphors present in the sample can be hydrolyzed when dispersed in

water. Thus, the minor decrease in intensity is attributed to a slight lower number of emitting nanophosphors in comparison with the present in the ethanolic solution.

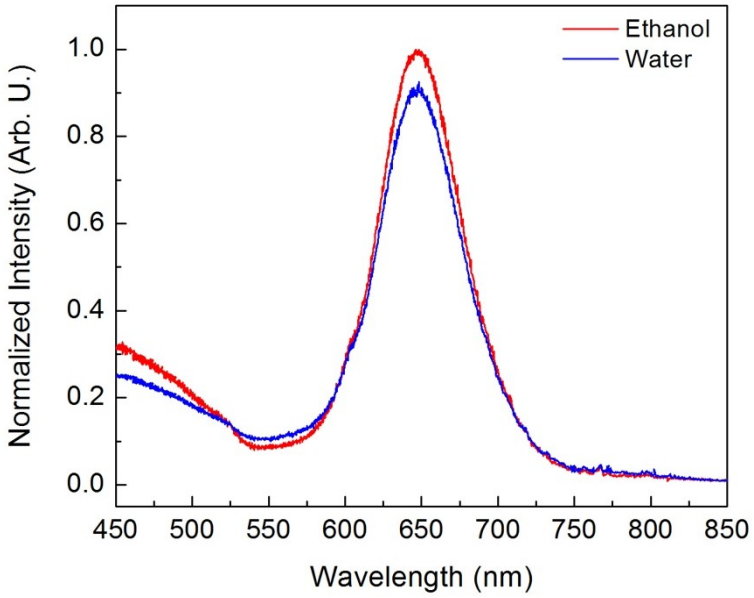

Figure 4.49 Emission spectra of TEOS-PVP-CaS:Eu^{2+}/Dy^{3+} nanophosphors dispersed in (red) ethanol 99% and (blue) water measured upon 254 nm irradiation.

A second procedure to graft a silica shell on the surface was proposed by Dr. Richards (Institut de Chemie of the French National Centre for Scientific Research) to obtain TEOS-CaS:Eu^{2+}/Dy^{3+} nanophosphors. This procedure avoids the adsorption of the PVP polymeric shell. To a solution of CaS:Eu^{2+}/Dy^{3+} nanophosphors dispersed in ethanol (2 mg/mL) 222 μL of ethanol, 247 of water and 6.7 μL of TEOS are added and the mixture is sonicated for 5 minutes to activate the hydrolysis process of the TEOS. After, 25 μL of aqueous solution of NH_4OH are added to catalyze the hydrolysis and condensation reactions on the surface of the nanophosphors. The reaction is left for 4 days at room temperature in a rotator. The TEOS-CaS:Eu^{2+}/Dy^{3+} nanophosphors are precipitated *via* centrifugation and washed several times with a mixture of water:ethanol. The TEOS-CaS:Eu^{2+}/Dy^{3+} nanophosphors were characterized by TEM (Figure 4.50). Images of the TEOS-CaS:Eu^{2+}/Dy^{3+} and the TEOS-PVP-CaS:Eu^{2+}/Dy^{3+} nanophosphors show that the silica coating is not distributed equally on the surface.

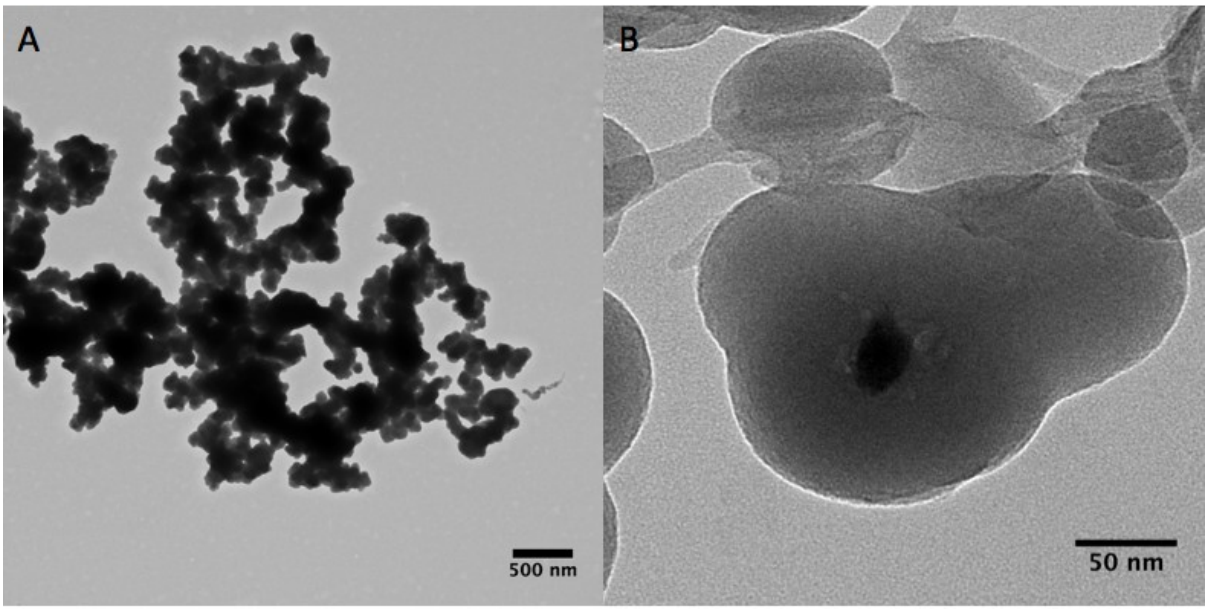

Figure 4.50. TEM images of TEOS-CaS:Eu^{2+}/Dy^{3+} nanophosphors (1 mg/mL in water) (A) scale bar: 500 nm and (B) scale bar: 50 nn.

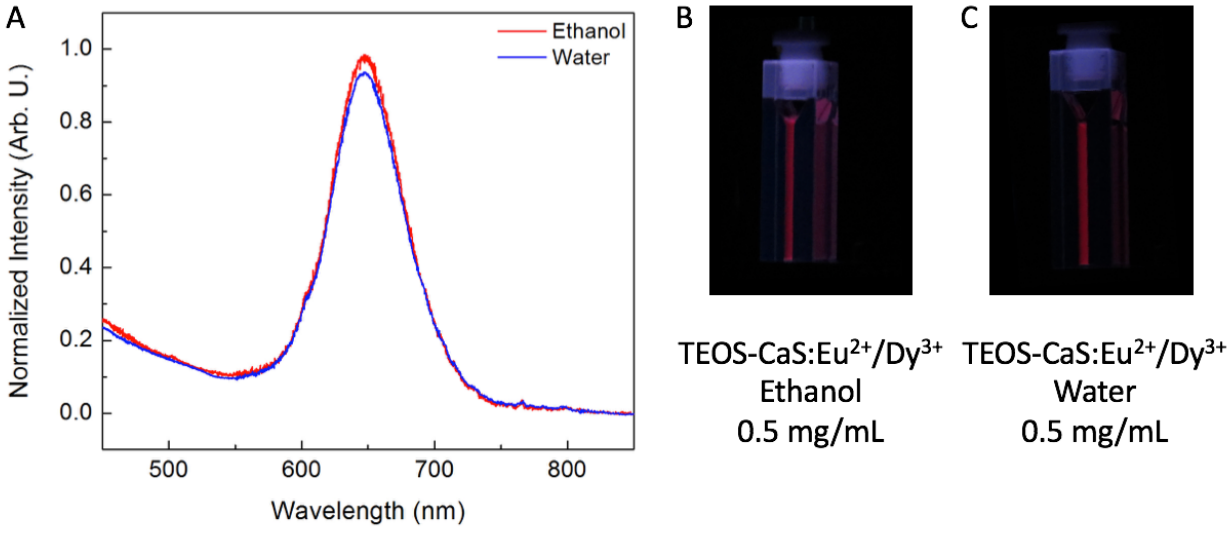

Figure 4.51(A) Emission spectra of TEOS-CaS:Eu^{2+}/Dy^{3+} nanophosphors dispersed in (red) ethanol 99% and (blue) water measured upon 254 nm irradiation. Concentration: 0.5 mg/mL. (B) and (C) Pictures of the luminescence exhibited by TEOS-CaS:Eu^{2+}/Dy^{3+} nanophosphors dispersed in ethanol 99% and water measured upon 254 nm irradiation respectively.

Likewise, the optical properties of the TEOS-CaS:Eu^{2+}/Dy^{3+} nanophosphors upon 254 nm excitation dispersed in the ethanol and in water did not show different features than those observed for the TEOS-PVP-CaS:Eu^{2+}/Dy^{3+} nanophosphors (Figure 4.51A). The direct grafting of the silica shell onto the unmodified surface of the CaS:Eu^{2+}/Dy^{3+} nanophosphors does not affect the environment of the ion emitting centres located in the surface, which would be characterised by a shift in the peak position of the bands of the CaS:Eu^{2+}/Dy^{3+} nanophosphors. Under UV light the TEOS-CaS:Eu^{2+}/Dy^{3+} nanophosphors dispersed in ethanol and in water exhibit similar luminescence intensities (Figure 4.51B,C).

The persistent luminescent properties of the TEOS-CaS:Eu^{2+}/Dy^{3+} nanophosphors dispersed in water (0.5 mg/mL) were evaluated using a persistent luminescence imaging set up (Figure 4.52). Unmodified CaS:Eu^{2+}/Dy^{3+} nanophosphors were selected as the control sample as it provides information on the decay of the intensity of the signal as consequence of the hydrolysis of the nano-host. Unmodified CaS:Eu^{2+}/Dy^{3+} and TEOS-CaS:Eu^{2+}/Dy^{3+} nanophosphors dispersed in water nanophosphors were irradiated for a period of 2 minutes with 254 nm light. Images of the red persistent luminescence in the absence of external excitation were acquired after 5, 30 and 60 minutes. The shorter irradiation time employed allowed the acquisition of the persistent luminescence exhibited by the unmodified CaS:Eu^{2+}/Dy^{3+} nanophosphors after 5 minutes of the charging process. After 30 minutes of being irradiated, no red persistent luminescence is detected as it was expected due to hygroscopic character of the CaS nano-host. Contrarily, the red persistent luminescence exhibited by TEOS-CaS:Eu^{2+}/Dy^{3+} nanophosphors was detected during the time frame of the experiment. Thus, the direct grafting of the silica shell on the surface of the nanophosphors does not influence the shallow traps responsible of the persistent luminescence.

The grafting of a silica shell on the surface of the CaS:Eu^{2+}/Dy^{3+} nanophosphors allowed the dispersion of the nanocrystals in aqueous environment maintaining its persistent luminescence properties. The TEOS-PVP-CaS:Eu^{2+}/Dy^{3+} and TEOS-CaS:Eu^{2+}/Dy^{3+} nanophosphors are water dispersible nanocrystals that exhibit red persistent luminescence in solution (650 nm), an emission in the NIR-I biological window. The red persistent

luminescence of the TEOS-CaS:Eu^{2+}/Dy^{3+} nanophosphors has a duration of at least an 1 hour after being charged with UV light for 2 min.

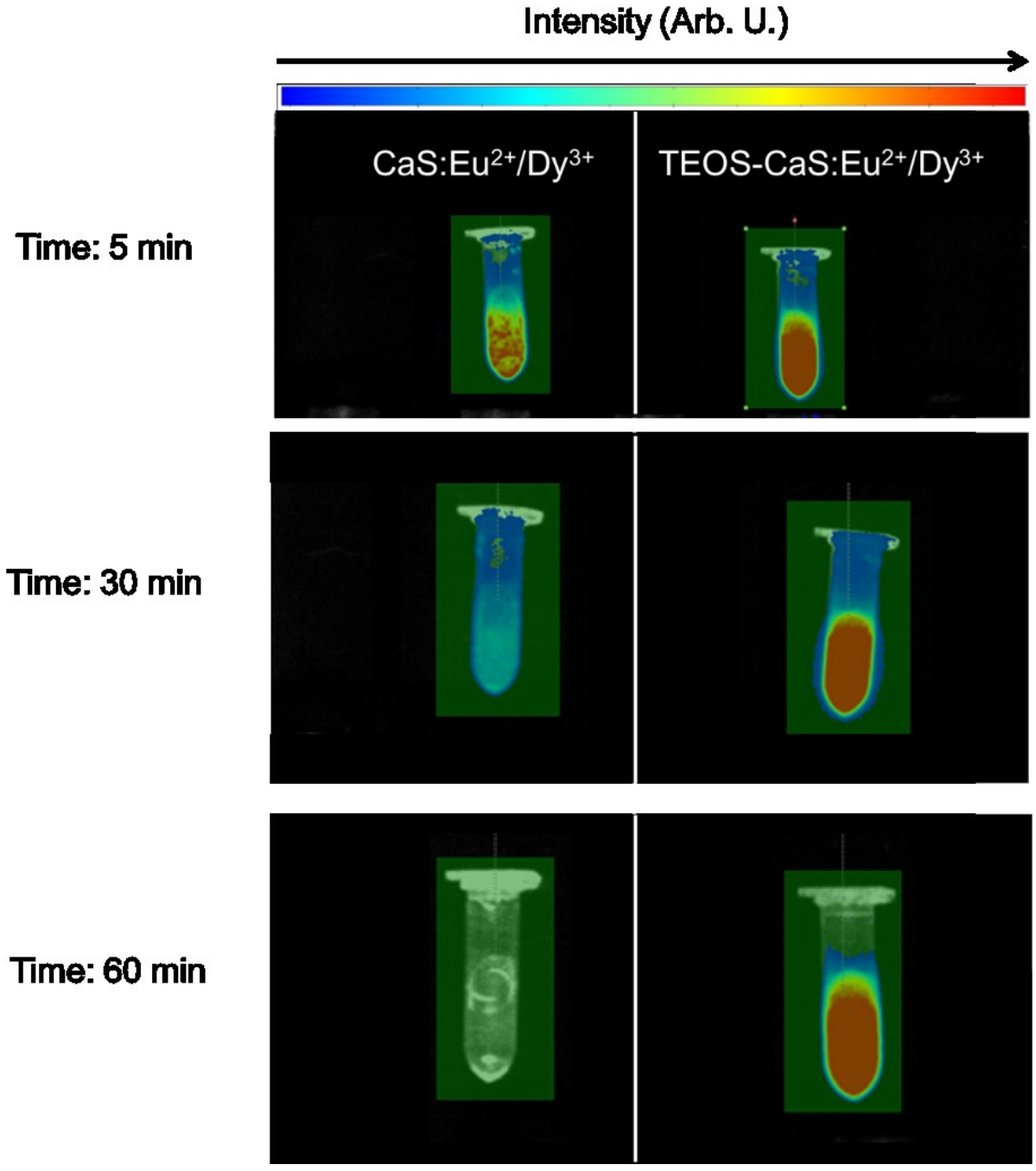

Figure 4.52 Imaging of the persistent luminescence exhibited by CaS:Eu^{2+}/Dy^{3+} and TEOS-CaS:Eu^{2+}/Dy^{3+} nanophosphors dispersed in water (0.5 mg/mL). Images were acquired under no excitation 5, 30 and 60 min after being irradiated with 254 nm light for 2 min.

4.4 Exploratory study of *In Vivo* Imaging using TEOS- CaS:Eu^{2+}/Dy^{3+} nanophosphors

The promising optical properties exhibited by the TEOS-CaS:Eu^{2+}/Dy^{3+} nanophosphors could potentially avoid some of the difficulties currently faced by other nanoparticles based luminescent probes in the acquisition of *in vivo* images. These nanophosphors can be optically excited before *in vivo* local or systemic injection; thus, the excitation of the nanophosphor of is not limited by the penetration of the excitation light through the skin and tissues. Moreover, the red persistent luminescence exhibited TEOS-CaS:Eu^{2+}/Dy^{3+} after being charged can be used to monitor the biodistribution of the nanophosphors in real time for at least one hour without the need of any external illumination source. This also could translate in a significant improvement of the signal-to-noise ratio and allowing the detection in rather deep organs.[80] However, effective use of these nanophosphors as luminescent probes for biomedical applications require elaborate studies involving the biodistribution, clearance and biocompatibility.

The fate of the nanoparticle-based luminescent probes once introduced in an small animal is dictated by its physicochemical properties such as morphology, size, surface charge, and hydrophobic/hydrophilic character. These properties will primarily determine the interaction with the different bio-entities in the body and finally the effectiveness of the nanoparticle in biomedical applications. The morphology of the nanoparticle play a role in the efficiency of their circulation in the body. Sphere-like shapes favor the circulation in the center of blood vessels due to the distribution of the hydrodynamic forces, causing less damage to the surrounding tissues. The size and the degree of polydispersity have a role in the biodistribution and clearance from the body. Surface properties will also dictate in these latter aspects. While circulating through the blood stream, nanoparticles can suffer of nonspecific adsorption of proteins (opsonins) at the surface that leads to particle accumulation and clearance *via* the reticular-endothelial system, also known as the macrophage system.[24, 138]

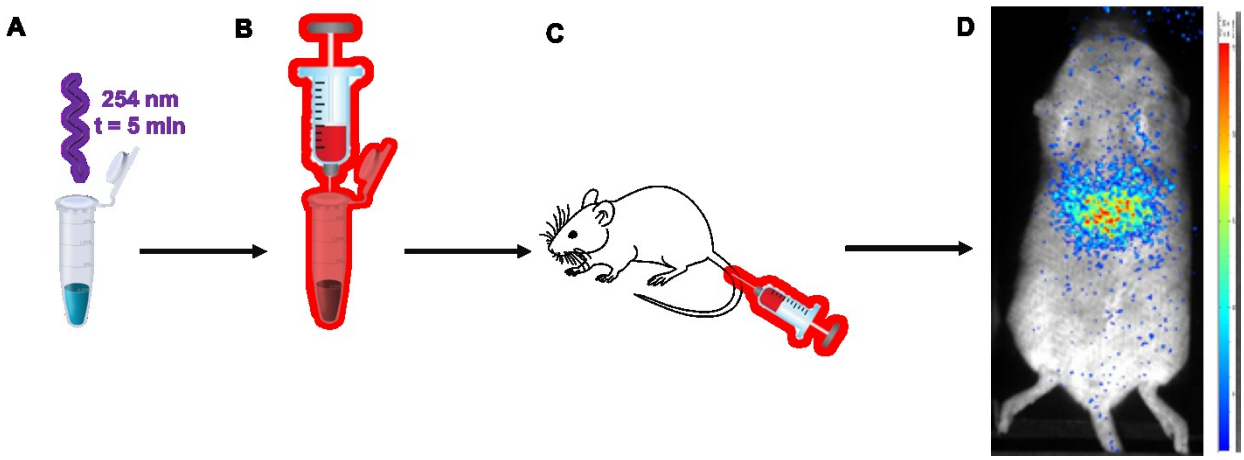

Figure 4.53 (A) TEOS-CaS:Eu^{2+}/Dy^{3+} dispersed in glucose solution (5%) under 254 nm irradiation for 5 min, after finishing of the charging process, (B) an aliquot of 200 μL is taken,(C) injected *via* intravenous tail injection and (D) *in vivo* image obtained 30 min after injection without external excitation.

An exploratory study was undertaken to attempt the acquisition of *in vivo* images of a Balc mouse using the red persistent luminescence of TEOS-CaS:Eu^{2+}/Dy^{3+} and to gain preliminary insights on the fate of TEOS-CaS:Eu^{2+}/Dy^{3+} after being injected. To acquire *in vivo* images using the red persistent luminescence of TEOS-CaS:Eu^{2+}/Dy^{3+}, the nanophosphors were dispersed in a aqueous glucose solution (5 wt%). The suspension was irradiated with 254 nm light for 5 minutes. Subsequently, 200 μL of the suspension were injected into a five-week-old female BALB/c mouse *via* intravenous tail injection and an *in vivo* image of the TEOS-CaS:Eu^{2+}/Dy^{3+} nanophosphors was taken after 30 min of the injection. Figure 4.53 shows an scheme of the procedure followed and the *in vivo* image acquired by using the red persistent luminescence exhibited by the injected TEOS-CaS:Eu^{2+}/Dy^{3+} nanophosphors. The in *vivo* image reveals that the nanophosphors accumulate in the liver, where the highest signal intensity is observed. This accumulation in the liver, detected as well using other nanoparticle based luminescent probes, can result from a rapid opsonisation and an uptake by endothelial and Kupffer cells of the reticular-endothelial system.[75, 80, 139] The result of this exploratory study confirms that red persistent luminescence of TEOS-CaS:Eu^{2+}/Dy^{3+} can be used to acquire *in vivo* images and suggests that future work should be oriented in the exploitation of the surface chemistry offered by the silica shell.

Chapter 5 – Conclusions

Persistent luminescence nanophosphors have drawn the attention of the scientific community dedicated to the development of novel luminescent probes for biomedical applications such as *in vivo* fluorescence optical imaging. The capacity of the persistent luminescence nanophosphors to store energy followed by the release of energy in the form of luminescence at room temperature for a period of time makes them feasible alternatives over other type of nanoparticle based luminescent probes. As *in vivo* luminescent probes, the persistent luminescence nanophosphors are excited *ex situ* and external excitation is not required during the acquisition of *in vivo* images thus, the generation of autofluorescence of tissue is eliminated. This result in the much-desired higher signal to noise ratio. Moreover, nanophosphors that exhibit high intensity and long persistent luminescence duration can be used for *in vivo* real time monitoring of biodistribution and accumulation studies as their emission can be detected using a sensitive camera outside the body. Nevertheless, the limitations in the exploitation of this type of nanomaterials as luminescent probes in biomedical applications are related to the low number of hosts that can offer the generation of persistent luminescence emissions found in the biological optical transparency window, synthetic methods that render particles in the micrometer scale, chemical instability and short duration of the persistent luminescence.

Sulfide based hosts, are probably the oldest well-known type of materials with the capacity to generate orange-red persistent luminescent materials. Calcium sulfide is a host that when doped with Eu^{2+} ions, can generate red persistent luminescence, which is required for efficient luminescent probes for applications in bioimaging. However, due to the size distribution in the micrometer range, its hygroscopic character and short persistent luminescence this host had been not considered as a potential material for bioimaging. Nonetheless, currently known synthesis and post-synthetic surface modification strategies inspired us to develop $CaS:Eu^{2+}/Dy^{3+}$ as a red persistent luminescent material in the nano size regime for potential bioimaging applications.

The development of the CaS:Eu^{2+}/Dy^{3+} nanophosphors was initiated by the synthesis of CaS nanoparticles, followed by the introduction of the Eu^{2+} ions (emitting centres) and ultimately the incorporation of Dy^{3+} ions, responsible for the lengthening of the duration time of the red persistent luminescence. The co-precipitation method was found to be a convenient synthetic approach to produce nano-sized CaS, CaS:Eu^{3+} and CaS:Eu^{3+}/Dy^{3+} nanoparticles. An annealing treatment was used to improve the crystallinity of the nanoparticles and in the case of the single doped and codoped nanophosphors to reduce Eu^{3+} ions to their divalent form, producing CaS:Eu^{2+} and CaS:Eu^{2+}/Dy^{3+} red persistent luminescence nanophosphors. A drawback of the use of the heat treatment on nanoparticles is the formation of agglomerates. Direct ultrasonication was found to be an useful technique to disrupt the agglomeration exhibited by the nanophosphors.

The substitution of Ca^{2+} ions by Dy^{3+} leads to the creation of defects that cause a disruption in the charge balance. These defects act as electron trapping sites that favour the lengthening of the red persistent luminescence and the storage of energy in deep traps that can only be released *via* NIR excitation. The nature of the traps responsible for the red persistent and NIR photo-stimulated luminescence were studied by luminescence spectroscopy and wavelength-resolved thermoluminescent measurements. A mechanism for the electron trapping after UV irradiation, and for persistent and NIR photo-stimulated luminescence for CaS nanoparticles, CaS:Eu^{2+} (0.02 mol%) and CaS:Eu^{2+} (0.02 mol%)/Dy^{3+} (0.002 mol%) nanophosphors was elucidated. The presence of electron trapping sites is observed in the bandgap of CaS nanoparticles. Intrinsic traps, consequence of the incorporation of Na^{+} ions as impurities, are formed during the synthesis of CaS, and are located at 0.02 eV (shallow traps) and 1.1 eV (deeper traps) below the conduction band. Under 254 nm irradiation, electrons are trapped in both type of intrinsic traps. Electrons trapped in the shallow traps can be released at room temperature generating a blue persistent luminescence whereas electrons trapped in the deeper traps require temperatures higher than 400K or 980 nm excitation to reverse the trapping process and recombine to generate photo-stimulated luminescence. Introducing Eu^{3+} as a dopant in CaS followed by the reduction to Eu^{2+}, creates two shallow traps (0.2 eV, 0.4 eV) below the conduction band. At room temperature, electrons in these shallow traps induce delayed and

persistent red emission from the $4f^6 5d^1$ energy levels of Eu^{2+} with a duration of approximately 8 minutes. Moreover, the incorporation of the codopant ion, Dy^{3+}, induces the formation of intermediate traps at approximately 0.6 eV below the conduction band. At room temperature, electrons captured in these intermediate traps can be released and retrapped by nearby shallow traps and promoted back to the conduction band, followed by a non-radiative decay to the $4f^6 5d^1$ energy levels of Eu^{2+} and subsequent radiative decay to the $4f^7$ ground state. This trapping-detrapping process translates in a red persistent luminescence with a duration of approximate 5 hours. Furthermore, the introduction of Dy^{3+} ions also generates the formation of deeper traps at approximately 1.3 eV below the conduction band. The electrons captured by these deeper traps can also be released *via* continuous NIR irradiation. This provides the possibility of releasing the stored energy at any time after the persistent luminescence has subsided.

To exploit the persistent luminescence properties exhibited by the CaS:Eu^{2+}/Dy^{3+} nanophosphors to acquire *in vivo* images, surface modification of the nanophosphors was necessary to achieve water dispersibility and avoid hydrolysis. This was accomplished through the modification of the surface of the nanophosphors *via* adsorption of a PVP polymer followed by the addition of a silica shell and *via* direct grafting of the silica shell on the "bare" surface of the CaS:Eu^{2+}/Dy^{3+} nanophosphors. Both strategies achieve the goal to disperse the nanocrystals in an aqueous environment since the silica shells prevents the hydrolization of the CaS core. In addition, the presence of the silica shell does not affect the optical properties of the nanophosphors.

An exploratory *in vivo* imaging experiment using a healthy Balc mouse and TEOS-CaS:Eu^{2+}/Dy^{3+} nanophosphors as luminescent probes was carried out. TEOS-CaS:Eu^{2+}/Dy^{3+} nanophosphors dispersed in a aqueous glucose solution (5 wt%) were charged with UV light and then injected intravenously to the animal. The red persistent luminescence exhibited was detected using an exterior camera, facilitating the *in vivo* monitoring of the fate of the nanophosphors inside the animal. *In vivo* images acquired after 30 minutes of the injection revealed accumulation of the TEOS-CaS:Eu^{2+}/Dy^{3+} nanophosphors in the liver. This accumulation is expected since this is the first response of the immune system of a healthy individual. The development of TEOS-CaS:Eu^{2+}/Dy^{3+} nanophosphors and the possibility to

generate *in vivo* images with them as luminescent probes contradicts the idea to discard sulfide based hosts in biological applications. Further research needs to be carried out with the aim of continuing improving the nanophosphors through the exploitation of the surface chemistry offered by the silica shell.

The work presented here aimed at developing a red persistent and NIR-photo stimulated nanophosphors suitable as an alternative to the current available nanoparticle based luminescent probes. Additionally, it offers a basic understanding of the persistent luminescence mechanism, primordial knowledge in the development of new nano-sized photonic materials. Furthermore, it establishes the base for the investigation on surface modification methods that can lead to the production of nanophosphors with active targeting capabilities.

Chapter 6 – Future Work

"If we knew all the answers, there will be no research" – Lailah Gifty Akita

Although the objectives established for the investigation and presentation of this thesis have been achieved, there are several lines of research arising from this work that should be pursued. This chapter presents some of these directions.

With respect to the characterization of the red persistent and NIR photo-stimulated luminescence duration time, the results were obtained at room temperature conditions. However, it should be kept in mind that after the introduction of the nanophosphor in a living species, the temperature is higher. As the release of electrons from the trapping sites is a temperature dependent process, characterization of the duration of the persistent and NIR photo-stimulated luminescence the CaS:Eu^{2+}/Dy^{3+} nanophosphors should be carried out as a function of temperature. It is suggested to study the release of the electrons from shallow traps and from deeper traps using NIR irradiation at a physiological temperature and conditions of hyperthermia.

Exploratory *in vivo* experiments revealed that the red persistent luminescence exhibited by the TEOS-CaS:Eu^{2+}/Dy^{3+} nanophosphors can be exploited in the acquisition of *in vivo* images. In addition, preliminary information on the fate of the TEOS-CaS:Eu^{2+}/Dy^{3+} nanophosphor was obtained. It was observed that the nanophosphors accumulate in the liver thus, a short circulation time is observed through the body before the nanophosphors are detected by the immune system. This has also been observed for other persistent luminescence nanoparticles with comparable size distribution and surficial chemical composition.[80] In order to exploit the red persistent luminescence for the *in vivo* imaging of specific diseases, targeting properties combined with longer times are required. Functionalization of nanoparticles with polyethylene glycol (PEG) has been reported to render charge-neutral particles that delay the uptake by liver and spleen.[141] Thus, it is suggested to explore the development of a surface modification strategy that leads to the formation of a silica shell that exhibits a mixture of terminal PEG chains and $-NH_2$ groups. It

is proposed to use a mixture of methoxy-PEG-silane and 3-(aminopropyl)-trimethoxysilane as precursors to produce a silica shell on the surface of the CaS:Eu^{2+}/Dy^{3+} nanophosphors. Whereas the PEG terminal chains may lengthen the circulation time of the red persistent luminescent nanophosphors, the terminal amino moieties can be exploited for the conjugation of targeting ligands of biomedical interest. It is important to emphasize that a complete study on the biodistribution, clearance and toxicity must be carried out for all proposed *in vivo* experiments.

The energy storage capacity of the TEOS-CaS:Eu^{2+}/Dy^{3+} nanophosphors and the possibility of releasing the stored energy *via* continuous NIR excitation should be explored for the acquisition of *in vivo* images. This optical property could be potentially used once the red persistent luminescence has subsided. However, it is important to emphasize that the possibility of liberating electrons trapped in the deeper traps of the TEOS-CaS:Eu^{2+}/Dy^{3+} *via* NIR photo-stimulation will be limited by the tissue penetration of the NIR excitation used. As well, the dependency of the photo-stimulated luminescence duration as a function of the power density of the NIR excitation must be taken into consideration for the application of NIR photo-stimulation of the TEOS-CaS:Eu^{2+}/Dy^{3+} nanophosphors in *in vivo* imaging.

Another ambitious step could be potentially taken to bring forth the use of this red persistent luminescence nanophosphor in other biomedical applications. Nanoscience has offered the opportunity to envision the combination of diagnosis and therapy through the design of nanoplatforms that simultaneously delivery therapeutic and imaging functions. Lin and collaborators reported the synthesis of TEOS-PVP-CaS:Fe nanoparticles that showed satisfactory heating efficiency.[137] The authors injected twelve female Balb/c mice injected with colon cancer cells (CT-26) and allowed tumors to grow to a size of 10 mm^2. TEOS-PVP-CaS:Fe^{3+} nanoparticles were injected in the localized tumors and the animals were immediately exposed to an oscillating magnetic field (750 Hz). Results were compared with infected animals that were not treated with TEOS-CaS:Fe^{3+} nanoparticles. The authors reported that localized tumor hyperthermia was achieved after exposure to the magnetic field reducing the size of the tumors while the tumors of the non-treated animals continue to grow in spite to be exposed to the same oscillating magnetic field. We have shown the possibility to carry out in *vivo* imaging using TEOS-CaS:Eu^{2+}/Dy^{3+}thus we propose the

synthesis of CaS:Eu^{2+}/Fe^{3+}/Dy^{3+} nanophosphors and carry out an study of the optical and magnetic properties exhibited to evaluate its potential as a theranostic nanoplatform.

REFERENCES

[1] A. G. Webb, *Introduction to Biomedical Imaging*, Wiley, **2002**.

[2] K. K. Shung, M. B. Smith, B. Tsui, *Principles of Medical Imaging*, Academic Press, Inc, United States of America, **1992**.

[3] a) R. Vadivambal, D. S. Jayas, *Bio-Imaging Principles, Techniques and Applications*, CRC Press Boca Raton, **2016**; b) R. Weissleder, M. J. Pittet, *Nature* **2008**, *452*, 580-589.

[4] a) R. Weissleder, V. Ntziachristos, *Nature Medicine* **2003**, *9*, 123-128; b) B. Costas, *Measurement Science and Technology* **2009**, *20*, 104020; c) S. H. Yun, G. J. Tearney, B. E. Bouma*, Vol. 5502*, **2004**, pp. 17-24.

[5] a) H. Xu, Q. Li, L. Wang, Y. He, J. Shi, B. Tang, C. Fan, *Chemical Society Reviews* **2014**, *43*, 2650-2661; b) C. J. Chang, T. Gunnlaugsson, T. D. James, *Chemical Society Reviews* **2015**, *44*, 4484-4486; c) D. Jaque, C. Richard, B. Viana, K. Soga, X. Liu, J. G. Solé, *Advances in Optics and Photonics* **2016**, *8*, 1-103; d) A. M. Ibarra-Ruiz, D. C. Rodríguez Burbano, J. A. Capobianco, *Advances in Physics X* **2016**, *1*; e) P. Padmanabhan, A. Kumar, S. Kumar, R. K. Chaudhary, B. Gulyás, *Acta Biomaterialia* **2016**, *41*, 1-16.

[6] a) J. S. Jaffe, *IEEE Journal of Oceanic Engineering* **2015**, *40*, 683-700; b) A. M. Safi, E. Chung, in *Biomedical Engineering: Frontier Research and Converging Technologies* (Eds.: H. Jo, H.-W. Jun, J. Shin, S. Lee), Springer International Publishing, Cham, **2016**, pp. 329-355; c) F. Leblond, S. C. Davis, P. A. Valdés, B. W. Pogue, *Journal of Photochemistry and Photobiology B: Biology* **2010**, *98*, 77-94.

[7] a) T. Etrych, H. Lucas, O. Janoušková, P. Chytil, T. Mueller, K. Mäder, *Journal of Controlled Release* **2016**, *226*, 168-181; b) D. A. Boas, D. H. Brooks, E. L. Miller, C. A. DiMarzio, M. Kilmer, R. J. Gaudette, Z. Quan, *IEEE Signal Processing Magazine* **2001**, *18*, 57-75; c) A. P. Gibson, J. C. Hebden, S. R. Arridge, *Physics in Medicine and Biology* **2005**, *50*, R1.

[8] K. Licha, in *Contrast Agents II: Optical, Ultrasound, X-Ray and Radiopharmaceutical Imaging* (Ed.: W. Krause), Springer Berlin Heidelberg, Berlin, Heidelberg, **2002**, pp. 1-29.

[9] R. Weissleder, *Nature Biotechnology* **2001**, *19*, 316-317.

[10] S. Prahl, S. Jacques*, Vol. 2016*, Prahl and Jacques, Portland, **1999**.

[11] A. M. Smith, M. C. Mancini, S. Nie, *Nature Nanotechnology* **2009**, *4*, 710-711.

[12] a) C.-H. Quek, K. W. Leong, *Nanomaterials* **2012**, *2*, 92; b) J. V. Frangioni, *Current Opinion in Chemical Biology* **2003**, *7*, 626-634; c) S. L. Jacques, *Physics in Medicine and Biology* **2013**, *58*, R37-R61.

[13] a) S. Diao, G. Hong, A. L. Antaris, J. L. Blackburn, K. Cheng, Z. Cheng, H. Dai, *Nano Research* **2015**, *8*, 3027-3034; b) E. Hemmer, A. Benayas, F. Legare, F. Vetrone, *Nanoscale Horizons* **2016**, *1*, 168-184.

[14] a) D. C. Rodríguez Burbano, R. Naccache, J. A. Capobianco, in *Handbook on the Physics and Chemistry of Rare Earths, Vol. Volume 47* (Eds.: B. Jean-Claude, K. P. Vitalij), Elsevier, **2015**, pp. 273-347; b) I. Johnson, *The Histochemical Journal* **1998**, *30*, 123-140.

[15] U. Resch-Genger, M. Grabolle, S. Cavaliere-Jaricot, R. Nitschke, T. Nann, *Nature Methods* **2008**, *5*, 763-775.

[16] A. L. Antaris, H. Chen, K. Cheng, Y. Sun, G. Hong, C. Qu, S. Diao, Z. Deng, X. Hu, B. Zhang, X. Zhang, O. K. Yaghi, Z. R. Alamparambil, X. Hong, Z. Cheng, H. Dai, *Nat Mater* **2016**, *15*, 235-242.

[17] M. Chen, X. He, K. Wang, D. He, X. Yang, H. Shi, *TrAC Trends in Analytical Chemistry* **2014**, *58*, 120-129.

[18] a) R. Alford, H. M. Simpson, J. Duberman, G. C. Hill, M. Ogawa, C. Regino, H. Kobayashi, P. L. Choyke, *Molecular Imaging* **2009**, *8*; b) J. O. Escobedo, O. Rusin, S. Lim, R. M. Strongin, *Current Opinion in Chemical Biology* **2010**, *14*, 64-70.

[19] R. P. Feynman, *Engineering and science* **1960**, *23*, 22-36.

[20] N. Kumar, S. Kumbhat, *Essentials in Nanoscience and Nanotechnology*, Joh Wiley & Sons. Inc, New Jersey, **2016**.

[21] B. A. Pierce, *Genetics: A Conceptual Approach*, 5th ed., W.H.Freeman & Co Ltd, **2014**.

[22] a) K. Chatterjee, S. Sarkar, K. Jagajjanani Rao, S. Paria, *Advances in Colloid and Interface Science* **2014**, *209*, 8-39; b) N. T. K. Thanh, L. A. W. Green, *Nano Today* **2010**, *5*, 213-230; c) G. L. Prasad, in *Safety of Nanoparticles: From Manufacturing to Medical Applications* (Ed.: J. T. Webster), Springer New York, New York, NY, **2009**,

pp. 89-109; d) B. Mishra, B. B. Patel, S. Tiwari, *Nanomedicine: Nanotechnology, Biology and Medicine*, *6*, 9-24.

[23] S. Wilhelm, M. Kaiser, C. Wurth, J. Heiland, C. Carrillo-Carrion, V. Muhr, O. S. Wolfbeis, W. J. Parak, U. Resch-Genger, T. Hirsch, *Nanoscale* **2015**, *7*, 1403-1410.

[24] A. Verma, F. Stellacci, *Small* **2010**, *6*, 12-21.

[25] a) R. Mout, D. F. Moyano, S. Rana, V. M. Rotello, *Chemical Society Reviews* **2012**, *41*, 2539-2544; b) O. S. Wolfbeis, *Chemical Society Reviews* **2015**, *44*, 4743-4768.

[26] a) G. E. LeCroy, S.-T. Yang, F. Yang, Y. Liu, K. S. Fernando, C. E. Bunker, Y. Hu, P. G. Luo, Y.-P. Sun, *Coordination Chemistry Reviews* **2016**; b) W. Fang, Y. Wei, *Journal of Innovative Optical Health Sciences* **2016**, 1630006; c) E. Abbasi, T. Kafshdooz, M. Bakhtiary, N. Nikzamir, N. Nikzamir, M. Nikzamir, M. Mohammadian, A. Akbarzadeh, *Artificial cells, nanomedicine, and biotechnology* **2016**, *44*, 885-891; d) A. Mukherjee, Y. Shim, J. Myong Song, *Biotechnology journal* **2016**, *11*, 31-42; e) S. Bouccara, G. Sitbon, A. Fragola, V. Loriette, N. Lequeux, T. Pons, *Current opinion in biotechnology* **2015**, *34*, 65-72; f) F. Peng, Y. Su, Y. Zhong, C. Fan, S.-T. Lee, Y. He, *Accounts of chemical research* **2014**, *47*, 612-623.

[27] L. Cheng, K. Yang, S. Zhang, M. Shao, S. Lee, Z. Liu, *Nano research* **2010**, *3*, 722-732.

[28] C. Li, Y. Zhang, M. Wang, Y. Zhang, G. Chen, L. Li, D. Wu, Q. Wang, *Biomaterials* **2014**, *35*, 393-400.

[29] A. L. Chen, M. A. Jackson, A. Y. Lin, E. R. Figueroa, Y. S. Hu, E. R. Evans, V. Asthana, J. K. Young, R. A. Drezek, *Nanoscale Research Letters* **2016**, *11*, 1-12.

[30] a) K. Van den Eeckhout, P. F. Smet, D. Poelman, *Materials* **2010**, *3*, 2536; b) Y. Zhuang, Y. Katayama, J. Ueda, S. Tanabe, *Optical Materials* **2014**, *36*, 1907-1912; c) A. Bessière, S. K. Sharma, N. Basavaraju, K. R. Priolkar, L. Binet, B. Viana, A. J. J. Bos, T. Maldiney, C. Richard, D. Scherman, D. Gourier, *Chemistry of Materials* **2014**, *26*, 1365-1373; d) D. C. Rodriguez Burbano, E. M. Rodriguez, P. Dorenbos, M. Bettinelli, J. A. Capobianco, *Journal of Materials Chemistry C* **2014**, *2*, 228-231; e) S. K. Singh, *RSC Advances* **2014**, *4*, 58674-58698; f) D. C. Rodríguez Burbano, S. K. Sharma, P. Dorenbos, B. Viana, J. A. Capobianco, *Advanced Optical Materials* **2015**, *3*, 551-557.

[31] N. D. Burrows, W. Lin, J. G. Hinman, J. M. Dennison, A. M. Vartanian, N. S. Abadeer, E. M. Grzincic, L. M. Jacob, J. Li, C. J. Murphy, *Langmuir* **2016**, *32*, 9905-9921.

[32] a) B. Viana, S. K. Sharma, D. Gourier, T. Maldiney, E. Teston, D. Scherman, C. Richard, *Journal of Luminescence* **2016**, *170, Part 3*, 879-887; b) Y. Li, M. Gecevicius, J. Qiu, *Chemical Society Reviews* **2016**, *45*, 2090-2136; c) C. Rosticher, B. Viana, T. Maldiney, C. Richard, C. Chanéac, *Journal of Luminescence* **2016**, *170, Part 2*, 460-466.

[33] T. Maldiney, A. Bessière, J. Seguin, E. Teston, S. K. Sharma, B. Viana, A. J. J. Bos, P. Dorenbos, M. Bessodes, D. Gourier, D. Scherman, C. Richard, *Nature Materials* **2014**, *13*, 418-426.

[34] J. Hölsä, *The Electrochemical Society Interface* **2009**, *18*, 42-45.

[35] D. J. McGowan, *Science* **1883**, *2*.

[36] E. N. Harvey, *A history of luminescence from the earliest times until 1900*, American Philosophical Society, **1957**.

[37] a) F. Liceti, in *Litheosphorus sive De Lapide Bononiensi, Vol. 4*, Udine, **1653**; b) A. Kircher, *Ars Magna Lucis et Umbrae*, Rome, **1646**; c) T. Browne, *Pseudodoxia Epidemica*, 2 ed., **1650**; d) N. Zucchi, *Optica Philosophia*, **1652**.

[38] T. Sidot, *Comptes Rendus de l'Académie des Sciences* **1866**, *62*, 999-1001.

[39] E. Nakazawa, S. Shionoya, W. Yen, *CRC Press, Boca Raton, Boston, London, New York, Washington, DC* **1999**, 102.

[40] K. Van den Eeckhout, P. F. Smet, D. Poelman, *Materials* **2010**, *3*, 2536-2566.

[41] T. Matsuzawa, Y. Aoki, N. Takeuchi, Y. Murayama, *Journal of The Electrochemical Society* **1996**, *143*, 2670-2673.

[42] B. Lei, Y. Liu, G. Tang, Z. Ye, C. Shi, *Materials Chemistry and Physics* **2004**, *87*, 227-232.

[43] X. Wang, Z. Zhang, Z. Tang, Y. Lin, *Materials Chemistry and Physics* **2003**, *80*, 1-5.

[44] A. Lecointre, R. Ait Benhamou, A. Bessiére, G. Wallez, M. Elaatmani, B. Viana, *Optical Materials* **2011**, *34*, 376-380.

[45] a) H. Takasaki, S. Tanabe, T. Hanada, *Journal of the Ceramic Society of Japan* **1996**, *104*, 322-326; b) T. Katsumata, T. Nabae, K. Sasajima, S. Komuro, T. Morikawa, *Journal of The Electrochemical Society* **1997**, *144*, L243-L245.

[46] D. Jia, X.-j. Wang, W. Jia, W. M. Yen, *Journal of Luminescence* **2007**, *122–123*, 311-314.

[47] a) J. Hölsä, H. Jungner, M. Lastusaari, J. Niittykoski, *Journal of Alloys and Compounds* **2001**, *323–324*, 326-330; b) T. Katsumata, T. Nabae, K. Sasajima, T. Matsuzawa,

Journal of Crystal Growth **1998**, *183*, 361-365; c) Y. Lin, Z. Tang, Z. Zhang, C. Nan, *Journal of the European Ceramic Society* **2003**, *23*, 175-178.

[48] D. Jia, W. M. Yen *Journal of The Electrochemical Society* **2003**, *150*, H61-H65.

[49] a) Y. Lin, Z. Zhang, Z. Tang, J. Zhang, Z. Zheng, X. Lu, *Materials Chemistry and Physics* **2001**, *70*, 156-159; b) R. Sakai, T. Katsumata, S. Komuro, T. Morikawa, *Journal of Luminescence* **1999**, *85*, 149-154.

[50] D. Jia, X.-j. Wang, E. van der Kolk, W. M. Yen, *Optics Communications* **2002**, *204*, 247-251.

[51] Y. Lin, Z. Tang, Z. Zhang, X. Wang, J. Zhang, *Journal of Materials Science Letters*, *20*, 1505-1506.

[52] a) T. Aitasalo, J. Hölsä, M. Kirm, T. Laamanen, M. Lastusaari, J. Niittykoski, J. Raud, R. Valtonen, *Radiation Measurements* **2007**, *42*, 644-647; b) L. Jiang, C. Chang, D. Mao, *Journal of Alloys and Compounds* **2003**, *360*, 193-197.

[53] L. Lin, Z. Zhao, W. Zhang, Z. Zheng, M. Yin, *Journal of Rare Earths* **2009**, *27*, 749-752.

[54] a) T. Aitasalo, J. Hölsä, T. Laamanen, M. Lastusaari, L. Lehto, J. Nittykoski, F. Pellé, *Ceramics-Silikáty* **2005**, *49*, 58-62; b) T. Aitasalo, D. Hreniak, J. Hölsä, T. Laamanen, M. Lastusaari, J. Niittykoski, F. Pellé, W. Stręk, *Journal of Luminescence* **2007**, *122–123*, 110-112.

[55] Y. Gong, X. Xu, W. Zeng, C. Wu, Y. Wang, *Physics Procedia* **2012**, *29*, 86-90.

[56] R. Pang, C. Li, L. Shi, Q. Su, *Journal of Physics and Chemistry of Solids* **2009**, *70*, 303-306.

[57] R. Pang, C. Li, S. Zhang, Q. Su, *Materials Chemistry and Physics* **2009**, *113*, 215-218.

[58] B. Lei, Y. Liu, Z. Ye, C. Shi, *Journal of Luminescence* **2004**, *109*, 215-219.

[59] J. Kuang, Y. Liu, J. Zhang, *Journal of Solid State Chemistry* **2006**, *179*, 266-269.

[60] a) Y. Miyamoto, H. Kato, Y. Honna, H. Yamamoto, K. Ohmi, *Journal of The Electrochemical Society* **2009**, *156*, J235-J241; b) K. Van den Eeckhout, P. F. Smet, D. Poelman, *Journal of Luminescence* **2009**, *129*, 1140-1143.

[61] J. Fu, *Electrochemical and Solid-State Letters* **2000**, *3*, 350-351.

[62] J. Fu, *Journal of the American Ceramic Society* **2002**, *85*, 255-257.

[63] a) D. Jia, W. Jia, D. R. Evans, W. M. Dennis, H. Liu, J. Zhu, W. M. Yen, *Journal of Applied Physics* **2000**, *88*, 3402-3407; b) D. Jia, J. Zhu, B. Wu, *Journal of The Electrochemical*

Society **2000**, *147*, 386-389; c) D. Jia, *Journal of The Electrochemical Society* **2006**, *153*, H198-H201.

[64] M. Lastusaari, T. Laamanen, M. Malkamaki, K. Eskola, A. Kotlov, S. Carlson, E. Welter, H. Brito, M. Betinnelli, H. Junger, J. Hölsa, *European Journal of Mineralogy* **2012**, *24*, 885-890.

[65] a) C. Guo, C. Zhang, Y. Lü, Q. Tang, Q. Su, *physica status solidi (a)* **2004**, *201*, 1588-1593; b) N. Hikmat, K. Ariyuki, T. Hideyuki, I. Kazutoshi, B. Ayaz, I. Seishi, *Japanese Journal of Applied Physics* **2002**, *41*, 1424; c) H. Najafov, A. Kato, H. Toyota, K. Iwai, A. Bayramov, S. Iida, *Japanese journal of applied physics* **2002**, *41*, 2058-2065.

[66] P. F. Smet, N. Avci, D. Poelman, *Journal of The Electrochemical Society* **2009**, *156*, H243-H248.

[67] B. Lei, Y. Liu, J. Zhang, J. Meng, S. Man, S. Tan, *Journal of Alloys and Compounds* **2010**, *495*, 247-253.

[68] a) P. F. Smet, K. V. d. Eeckhout, O. Q. D. Clercq, D. Poelman, in *Handbook on the physics and chemistry of rare earths, Vol. 48* (Eds.: J.-C. G. Bünzli, V. K. Pecharsky), Elsevier, Amsterdan, The Netherlands, **2015**; b) T. Aitasalo, P. Dereń, J. Hölsä, H. Jungner, J. C. Krupa, M. Lastusaari, J. Legendziewicz, J. Niittykoski, W. Stręk, *Journal of Solid State Chemistry*, *171*, 114-122.

[69] a) T. Peng, H. Yang, X. Pu, B. Hu, Z. Jiang, C. Yan, *Materials Letters* **2004**, *58*, 352-356; b) Z. Qiu, Y. Zhou, M. Lü, A. Zhang, Q. Ma, *Acta Materialia* **2007**, *55*, 2615-2620; c) C. Zhao, D. Chen, *Materials Letters* **2007**, *61*, 3673-3675.

[70] J. Geng, Z. Wu, *Journal of Materials Synthesis and Processing*, *10*, 245-248.

[71] a) T. Aitasalo, J. Hölsä, H. Jungner, M. Lastusaari, J. Niittykoski, M. Parkkinen, R. Valtonen, *Optical Materials* **2004**, *26*, 113-116; b) J. Sánchez-Benítez, A. de Andrés, M. Marchal, E. Cordoncillo, M. V. Regi, P. Escribano, *Journal of Solid State Chemistry*, *171*, 273-277.

[72] C. Rosticher, C. Chanéac, B. Viana, M. A. Fortin, J. Lagueux, L. Faucher, in *Oxide-based Materials and Devices VI, Vol. Proc. SPIE 9364*, **2015**.

[73] T. Maldiney, A. Lecointre, B. Viana, A. Bessière, M. Bessodes, D. Gourier, C. Richard, D. Scherman, *Journal of the American Chemical Society* **2011**, *133*, 11810-11815.

[74] A. Lecointre, A. Bessière, B. Viana, D. Gourier, *Radiation Measurements* **2010**, *45*, 497-499.

[75] Q. le Masne de Chermont, C. Chanéac, J. Seguin, F. Pellé, S. Maîtrejean, J.-P. Jolivet, D. Gourier, M. Bessodes, D. Scherman, *Proceedings of the National Academy of Sciences* **2007**, *104*, 9266-9271.

[76] Y. Li, Y.-Y. Li, K. Sharafudeen, G.-P. Dong, S.-F. Zhou, Z.-J. Ma, M.-Y. Peng, J.-R. Qiu, *Journal of Materials Chemistry C* **2014**, *2*, 2019-2027.

[77] X. Fu, C. Liu, J. Shi, H. Man, J. Xu, H. Zhang, *Optical Materials* **2014**, *36*, 1792-1797.

[78] a) J. Li, Q. Wu, J. Wu, in *Handbook of Nanoparticles* (Ed.: M. Aliofkhazraei), Springer International Publishing, Cham, **2016**, pp. 295-328; b) W. Li, Y. Liu, P. Ai, X. Chen, *Journal of Rare Earths* **2009**, *27*, 895-899.

[79] M. Lun, C. Wei, *Nanotechnology* **2010**, *21*, 385604.

[80] C. Richard, T. Maldiney, Q. l. M. d. Chermont, J. Seguin, N. Wattier, G. Courties, F. Apparailly, M. Bessodes, D. Scherman, in *Advances in Bio-Imaging: From Physics to Signal Understanding Issues: State-of-the-Art and Challenges* (Eds.: N. Loménie, D. Racoceanu, A. Gouailard), Springer Science & Businnes Media, Springer Berlin Heidelberg, **2012**.

[81] J. Hölsä, *Electrochemical Society Interface* **2009**, *18*, 42-45.

[82] a) Y. Lin, Z. Zhang, Z. Tang, X. Wang, J. Zhang, Z. Zheng, *Journal of the European Ceramic Society* **2001**, *21*, 683-685; b) A. Nag, T. R. N. Kutty, *Materials Research Bulletin* **2004**, *39*, 331-342; c) W. Jia, H. Yuan, S. Holmstrom, H. Liu, W. M. Yen, *Journal of Luminescence* **1999**, *83–84*, 465-469; d) W. Jia, H. Yuan, L. Lu, H. Liu, W. M. Yen, *Journal of Luminescence* **1998**, *76–77*, 424-428; e) H. B. Yuan, W. Jia, S. A. Basun, L. Lu, R. S. Meltzer, W. M. Yen, *Journal of The Electrochemical Society* **2000**, *147*, 3154-3156.

[83] T. Aitasalo, J. Hölsä, H. Jungner, M. Lastusaari, J. Niittykoski, *Journal of Luminescence* **2001**, *94–95*, 59-63.

[84] a) P. Dorenbos, *Journal of The Electrochemical Society* **2005**, *152*, H107-H110; b) P. Dorenbos, *Journal of Luminescence* **2004**, *108*, 301-305.

[85] P. Dorenbos, *Journal of Luminescence* **2013**, *135*, 93-104.

[86] F. Clabau, X. Rocquefelte, S. Jobic, P. Deniard, M. H. Whangbo, A. Garcia, T. Le Mercier, *Chemistry of Materials* **2005**, *17*, 3904-3912.

[87] T. Aitasalo, J. Hölsä, H. Jungner, M. Lastusaari, J. Niittykoski, *The Journal of Physical Chemistry B* **2006**, *110*, 4589-4598.

[88] P. K. Ghosh, B. Ray, *Progress in Crystal Growth and Characterization of Materials* **1992**, *25*, 1-37.

[89] a) R. Das, S. Pandey, *International Journal of Material Science* **2011**, *1*, 35-40; b) C. Zhang, J. Lin, *Chemical Society Reviews* **2012**, *41*, 7938-7961.

[90] a) J. H. Crawford, L. M. Slifkin, *Point Defects in Solids, Vol. 1*, Plenum PRess, New York, **1972**; b) W. D. Callister, *Materials Science and Engineering: An Introduction*, John Wiley & Sons, New York, **2007**.

[91] a) P. Kofstad, T. Norby, *Defects and Transport in Crystalline Solids*, University of Oslo, Oslo, **2007**; b) P. Ehrhart, in *Landolt-Börnstein, Vol. 25* (Ed.: H. Ullmaier), Springer, Berlin, **1991**.

[92] J. G. Solé, L. E. Bausá, D. Jaque, *An Introduction to the Optical Spectroscopy of Inorganic Solids*, John Wiley & Sons Ltd, West Sussex, England, **2005**.

[93] R. A. Johnson, J. R. Brown, *Journal of Materials Research* **1992**, *7*, 3213-3218.

[94] J. N. Lalena, D. A. Cleary, *Principles of inorganic materials design*, John Wiley & Sons, **2010**.

[95] C. Kittel, *Introduction to Solid State Physics*, Wiley, **2004**.

[96] G. Blasse, B. C. Grabmaier, *Luminescent Materials*, Springer-Verlag Berlin Heidelberg, Berlin **1994**.

[97] C. Jørgensen, *Progress in Inorganic Chemistry, Volume 4* **1962**, 73-124.

[98] B. Huang, *Inorganic Chemistry* **2015**, *54*, 11423-11440.

[99] R. Pandey, S. Sivaraman, *Journal of Physics and Chemistry of Solids* **1991**, *52*, 211-225.

[100] P. Dorenbos, A. J. J. Bos, *Radiation Measurements* **2008**, *43*, 139-145.

[101] P. Dorenbos, *Journal of Physics: Condensed Matter* **2003**, *15*, 8417.

[102] A. B. Parmentier, J. J. Joos, P. F. Smet, D. Poelman, *Journal of Luminescence* **2014**, *154*, 445-451.

[103] Y. Nobuhiko, *Japanese Journal of Applied Physics* **1991**, *30*, 3335.

[104] S. Yokono, T. Abe, T. Hoshina, *Journal of the Physical Society of Japan* **1979**, *46*, 351-352.

[105] S. W. McKeever, *Thermoluminescence of solids, Vol. 3*, Cambridge University Press, **1988**.

[106] R. Boyle*, Vol. 3* (Ed.: M. D. Peter Shaw), W. and J. Innys, **1725**.

[107] M.-A. Seeley, *Journal of Archaeological Science* **1975**, *2*, 17-43.

[108] M. D. Fay, *Histoire de L'Academie Royale des Sciences* **1735**, *1*, 347-372.

[109] E. Wiedemann, G. C. Schmidt, *Ann. d. Physik.* **1895**, *56*, 210-210.

[110] A. Jabłoński, *Zeitschrift für Physik* **1935**, *94*, 38-46.

[111] J. Randall, M. Wilkins, in *Proceedings of the Royal Society of London A: Mathematical, Physical and Engineering Sciences, Vol. 184*, The Royal Society, **1945**, pp. 365-389.

[112] S. W. S. McKeever, *Nuclear Instruments and Methods* **1980**, *175*, 19-20.

[113] G. Garlick, A. Gibson, *Proceedings of the physical society* **1948**, *60*, 574.

[114] K. Vinay, K. Ravi, S. P. Lochab, S. Nafa, *Journal of Physics D: Applied Physics* **2006**, *39*, 5137.

[115] X. Peng, J. Wickham, A. P. Alivisatos, *Journal of the American Chemical Society* **1998**, *120*, 5343-5344.

[116] B. Sun, G. Yi, D. Chen, Y. Zhou, J. Cheng, *Journal of Materials Chemistry* **2002**, *12*, 1194-1198.

[117] a) V. Ankush, S. Surender, K. Ravi, S. P. Lochab, V. V. S. Kumar, S. Nafa, *Journal of Physics D: Applied Physics* **2009**, *42*, 105103; b) S. Y.-H. Wu, C.-L. Tseng, F.-H. Lin, *Journal of Nanoparticle Research* **2010**, *12*, 1173-1185; c) E. I. Anila, A. Arun, M. K. Jayaraj, *Nanotechnology* **2008**, *19*, 145604; d) Y. Zhao, F. T. Rabouw, C. d. M. Donegá, A. Meijerink, C. A. van Walree, *Materials Letters* **2012**, *80*, 75-77; e) V. Kumar, S. S. Pitale, M. M. Biggs, I. M. Nagpure, O. M. Ntwaeaborwa, H. C. Swart, *Materials Letters* **2010**, *64*, 752-754.

[118] K. Vinay, S. Nafa, K. Ravi, S. P. Lochab, *Journal of Physics: Condensed Matter* **2006**, *18*, 5029.

[119] U. Holzwarth, N. Gibson, *Nature Nanotechnology* **2011**, *6*, 534-534.

[120] a) R. Pandey, J. E. Jaffe, A. B. Kunz, *Physical Review B* **1991**, *43*, 9228-9237; b) V. S. Stepanyuk, A. Szász, O. V. Farberovich, A. A. Grigorenko, A. V. Kozlov, V. V. Mikhailin, *Physica Status Solidi* **1989**, *155B*, 215-220.

[121] P. M. Jaffe, E. Banks, *Journal of the Electrochemical Society* **1955**, *102*, 518-523.

[122] a) K. Katsuhiro, O. Fumio, *Japanese Journal of Applied Physics* **1983**, *22*, 76; b) H. L. Park, H. K. Kim, C. H. Chung, S. K. Chang, J.-T. Yu, *Solid State Communications* **1989**, *69*, 765-767.

[123] Y. Nobuhiko, F. Shigeru, I. Sumiaki, O. Hideomi, *Japanese Journal of Applied Physics* **1993**, *32*, 3135.

[124] R. Shannon, *Acta Crystallographica Section A* **1976**, *32*, 751-767.

[125] a) C. Enrico, B. Enrico, B. Alessandro, *Journal of Physics: Condensed Matter* **2002**, *14*, 5221; b) Y. Chen, X. Cheng, M. Liu, Z. Qi, C. Shi, *Journal of Luminescence* **2009**, *129*, 531-535.

[126] H. Chen, Y. Yu, H. L. Xin, K. A. Newton, M. E. Holtz, D. Wang, D. A. Muller, H. D. Abruña, F. J. DiSalvo, *Chemistry of Materials* **2013**, *25*, 1436-1442.

[127] C. Sauter, M. A. Emin, H. P. Schuchmann, S. Tavman, *Ultrasonics Sonochemistry* **2008**, *15*, 517-523.

[128] T. J. Mason, J. P. Lorimer, in *Applied Sonochemistry*, Wiley-VCH Verlag GmbH & Co. KGaA, **2003**, pp. 25-74.

[129] T. Maldiney, G. Sraiki, B. Viana, D. Gourier, C. Richard, D. Scherman, M. Bessodes, K. Van den Eeckhout, D. Poelman, P. F. Smet, *Opt. Mater. Express* **2012**, *2*, 261-268.

[130] W. W. Yu, E. Chang, J. C. Falkner, J. Zhang, A. M. Al-Somali, C. M. Sayes, J. Johns, R. Drezek, V. L. Colvin, *Journal of the American Chemical Society* **2007**, *129*, 2871-2879.

[131] F. Zhang, E. Lees, F. Amin, P. Rivera_Gil, F. Yang, P. Mulvaney, W. J. Parak, *Small* **2011**, *7*, 3113-3127.

[132] a) C. Graf, S. Dembski, A. Hofmann, E. Rühl, *Langmuir* **2006**, *22*, 5604-5610; b) I. Z. Dinic, M. E. Rabanal, K. Yamamoto, Z. Tan, S. Ohara, L. T. Mancic, O. B. Milosevic, *Advanced Powder Technology* **2016**, *27*, 845-853; c) R. Foldbjerg, P. Olesen, M. Hougaard, D. A. Dang, H. J. Hoffmann, H. Autrup, *Toxicology letters* **2009**, *190*, 156-162; d) H.-L. Liu, S. P. Ko, J.-H. Wu, M.-H. Jung, J. H. Min, J. H. Lee, B. H. An, Y. K. Kim, *Journal of Magnetism and Magnetic Materials* **2007**, *310*, e815-e817; e) H.-Y. Lee, S.-

H. Lee, C. Xu, J. Xie, J.-H. Lee, B. Wu, A. L. Koh, X. Wang, R. Sinclair, S. X. Wang, *Nanotechnology* **2008**, *19*, 165101; f) N. J. Johnson, N. M. Sangeetha, J.-C. Boyer, F. C. van Veggel, *Nanoscale* **2010**, *2*, 771-777; g) V. J. Leppert, S. Mahamuni, N. Kumbhojkar, S. H. Risbud, *Materials Science and Engineering: B* **1998**, *52*, 89-92.

[133] A. M. Smith, M. C. Mancini, S. Nie, *Nat Nano* **2009**, *4*, 710-711.

[134] W. Stöber, A. Fink, E. Bohn, *Journal of Colloid and Interface Science* **1968**, *26*, 62-69.

[135] G. Kolbe, **1956**.

[136] a) M. A. Habila, Z. A. ALOthman, A. M. El-Toni, J. P. Labis, X. Li, F. Zhang, M. Soylak, *Microchimica Acta* **2016**, *183*, 2377-2384; b) M. Runowski, S. Goderski, J. Paczesny, M. Księżopolska-Gocalska, A. Ekner-Grzyb, T. Grzyb, J. D. Rybka, M. Giersig, S. Lis, *The Journal of Physical Chemistry C* **2016**, *120*, 23788-23798; c) A. S. Karakoti, R. Shukla, R. Shanker, S. Singh, *Advances in Colloid and Interface Science* **2015**, *215*, 28-45; d) A. Sedlmeier, H. H. Gorris, *Chemical Society Reviews* **2015**, *44*, 1526-1560; e) J.-N. Liu, W.-B. Bu, J.-L. Shi, *Accounts of Chemical Research* **2015**, *48*, 1797-1805.

[137] S. Y.-H. Wu, K.-C. Yang, C.-L. Tseng, J.-C. Chen, F.-H. Lin, *Journal of Nanoparticle Research* **2011**, *13*, 1139-1149.

[138] F. Alexis, E. Pridgen, L. K. Molnar, O. C. Farokhzad, *Molecular Pharmaceutics* **2008**, *5*, 505-515.

[139] a) J. A. A. M. Kamps, H. W. M. Morselt, P. J. Swart, D. K. F. Meijer, G. L. Scherphof, *Proceedings of the National Academy of Sciences of the United States of America* **1997**, *94*, 11681-11685; b) M. Krieger, *Annual Review of Biochemistry* **1994**, *63*, 601-637.

[140] a) J. Kolosnjaj-Tabi, J. Volatron, F. Gazeau, in *Design and Applications of Nanoparticles in Biomedical Imaging* (Eds.: J. W. M. Bulte, M. M. J. Modo), Springer International Publishing, Cham, **2017**, pp. 9-41; b) J. Nam, N. Won, J. Bang, H. Jin, J. Park, S. Jung, S. Jung, Y. Park, S. Kim, *Advanced Drug Delivery Reviews* **2013**, *65*, 622-648; c) L. Xiaoyan, J. Cai, J. Tingting, F. Xiaohui, *Nanotechnology* **2015**, *26*, 175101.

[141] a) J. Cui, R. De Rose, K. Alt, S. Alcantara, B. M. Paterson, K. Liang, M. Hu, J. J. Richardson, Y. Yan, C. M. Jeffery, R. I. Price, K. Peter, C. E. Hagemeyer, P. S. Donnelly, S. J. Kent, F. Caruso, *ACS Nano* **2015**, *9*, 1571-1580; b) C. Cruje, B. Chithrani, *J Nanomed Res* **2014**, *1*, 00006; c) B. Pelaz, P. del Pino, P. Maffre, R. Hartmann, M. Gallego, S. Rivera-Fernández, J. M. de la Fuente, G. U. Nienhaus, W. J. Parak, *ACS Nano* **2015**, *9*,

6996-7008; d) R. Toy, K. Roy, *Bioengineering & Translational Medicine* **2016**, *1*, 47-62.